CAPTURE AND RELEASE OF BIOMOLECULES AND CANCER CELLS VIA SMART MATERIALS INTEGRATED MICROFLUIDIC CHIPS

A THESIS SUBMITTED TO

THE GRADUATE SCHOOL OF ENGINEERING AND SCIENCE

OF BILKENT UNIVERSITY

IN PARTIAL FULFILLMENT OF THE REQUIREMENTS FOR

THE DEGREE OF

MASTER OF SCIENCE

IN

MATERIALS SCIENCE AND NANOTECHNOLOGY

By

KUTAY SAĞDIÇ

AUGUST 2022

Capture and Release of Biomolecules and Cancer Cells via Smart Materials Integrated Microfluidic Chips
By KUTAY SAĞDIÇ
AUGUST 2022

We certify that we have read this thesis and that in our opinion it is fully adequate, in scope and in quality, as a thesis for the degree of Master of Science.

FATİH İNCİ(Advisor)

BENGİ ÖZGÜN ÖZTÜRK

BÜLEND ORTAÇ

Approved for the Graduate School of Engineering and Science:

Orhan Arıkan
Director of the Graduate School

ABSTRACT

CAPTURE AND RELEASE OF BIOMOLECULES AND CANCER CELLS VIA SMART MATERIALS INTEGRATED MICROFLUIDIC CHIPS

KUTAY SAĞDIÇ
M.S. in MATERIALS SCIENCE AND NANOTECHNOLOGY
Advisor: FATİH İNCİ
AUGUST 2022

Prevalent clinical conditions are impacting notably on our daily lives and the global economy. Healthcare system is hence garnering more interest in developing innovative material-based technologies along with accurate surface chemistry and signal generation reactions to measure biomarkers for disease diagnosis. In particular, biomedical studies focus to diagnose complex cases such as cancer. For instance, there are some critical stages in cancer development and metastasis. Moreover, impractical, invasive methods, and the restricted repertoire of targeted therapies are driving factors for researchers to find out new monitoring techniques that anticipate the future journey of cancer cells. On the other hand, the analysis of bodily fluids containing circulating tumor cells (CTCs) and biomarkers allows more insight into detecting/monitoring cancer as early as possible, and it would provide more information than that of any single-site biopsies. Yet, implementing the current technologies focusing on CTC detection and isolation in the clinics have notable challenges, i.e., expensive reagents/assays, complex operation, lengthy processes, bio-compatibility, and the need for specialized personnel. In this thesis, we have designed a microfluidic chip to hurdle these existing challenges, and for this regard, we tuned the surface area of the chip by integrating bio-mimetic smart materials (different shapes of silica particles-coated with poly(N-isopropylacrylamide). Initially, we tested our strategy with model proteins for both capture and release aspects. The smart materials were then modified with anti-EpCAM antibodies to capture human breast cancer cells (MCF-7) as a cancer model. Once the cells were captured in the chip, they were released by simply altering the 3-dimensional structure of smart materials above to lower critical solution temperature. Herein, we have anticipated that the developed platform would resolve cost, bio-compatibility, applicability, complexity, and assay duration-related challenges of current technologies in this realm.

Keywords: Smart Polymeric Materials, Microfluidic Chips, Circulating Tumor Cells, Cancer Diagnostics.

ÖZET

AKILLI MALZEMELER ENTEGRE EDILEN MİKROAKIŞKAN ÇİPLERDE BİYOMOLEKÜLLERİN VE NADİR KANSER HÜCRELERİNİN YAKALANMASI VE SALINMASI

KUTAY SAĞDIÇ
Malzeme Bilimi ve Nanoteknoloji, Yüksek Lisans
Tez Danışmanı: FATİH İNCİ
AĞUSTOS 2022

Halihazırda bulunan klinik tedavi koşulları ve yöntemleri günlük hayatımızı ve küresel ekonomiyi derinden etkiler. Sağlık sistemleri bu koşulları iyileştirmek ve hastalık biyobelirteçleri teşhisi için uygun yüzey kimyası ve sinyal değişimlerine hassas yenilikçi akıllı malzeme tabanlı teknolojiler geliştirmeye çalışır. Özellikle, biyomedikal çalışmalar kanser gibi kompleks hastalıkların tanısına odaklanır. Örneğin kanser gelişimi ve metastazında bazı kritik aşamalar bulunur. Ek olarak, pratik olmayan, invazif yöntemler ve sınırlı repertuara sahip tedaviler, araştırmacıların kanser hücrelerinin vücut içindeki yolculuğunu öngören yeni tanı metotları bulmaları için teşvik edici faktörlerdir. Öte yandan, vücut sıvılarında dolaşımda olan kanser hücrelerinin (CTCs) ve biyobelirteçlerin analizi kanserin erken safhalarda tespiti ve izlenmesine olanak sağlamakta ve kanser tespiti hakkında tek bir bölge biyopsi örneğinden çok daha fazla bilgi sağlar. Fakat, klinik çalışmalarda CTC tespiti ve izolasyonu için mevcut teknolojilerde pahalı reaktifler/tahliller, karmaşık operasyon süreçleri, düşük biyo-uyumluluk ve uzman personel ihtiyacı gibi birçok zorlukla karşılaşılır. Bu tezde, mevcut zorlukların üstesinden gelmek için bir mikroakışkan çip tasarladık ve bu bağlamda, biyo-mimetik akıllı malzemeyi (poli(N-izopropilakrilamid) ile kaplanmış farklı şekildeki silika parçacıkları) entegre ederek çipin yüzey alanını arttırdık. İlkin, tasarladığımız bu yöntemi test etmek adına model proteinlerin yakalanması ve salınması gerçekleştirildi. Bu akıllı malzemeler daha sonra anti-EpCAM antikorları ile modifiye edilerek insan meme kanseri hücrelerini (MCF-7) yakalamak ve tespit etmek için kullanıldı. Kanser hücreleri mikroakışkan çip içinde yakalandıktan sonra düşük kritik çözelti sıcaklığı (LCST) üzerine çıkılarak malzemelerin 3-boyutlu yapısı değiştirilip hücrelerin salınmasını sağlandı. Tezin bu noktasında, geliştirdiğimiz mikroakışkan platformun maliyet, biyo-uyumluluk, uygulanabilirlik, karmaşıklık ve test süresiyle ilgili günümüz teknolojilerinin sıkıntılarını çözmesi hedeflenmektedir.

Anahtar sözcükler: *Akıllı Polimerik Malzemeler, Mikroakışkan çipler, Dolaşımda Tümör Hücreleri, Kanser Tanısı.*

Acknowledgement

First and foremost, I would like to express my special thanks to my advisor, Assistant Prof. Dr. Fatih Inci for his guidance and encouragement in my research. His support helped me to develop an interdisciplinary comprehension, which I can facilitate throughout my research career. His life lessons and supportive attitude made me endure in very hard times. His teaching not only contributed to my academic career but also he is a role model for me. Moreover, being an MS and graduate researcher in "Incilab" have been an extraordinary experience for me.

I would like to thank the dear members of my thesis committee Assistant Prof. Dr. Fatih Inci and Assistant Prof. Dr. Bülend Ortaç from Bilkent University and Associate Prof. Dr. Bengi Özgün Öztürk for their perceptive comments and feedback.

I would also like to additionally thank Associate Prof. Dr. Bengi Özgün Öztürk for his endless devotion, insightful comments, feedbacks, and exceptional supports. He is truly a remarkable professor. He is a hero in his work. I will carry his doctrines with me throughout my research career.

This thesis simply would not have been possible without the help of Incilab family. During my research, one of the most valuable things that I gained is lifelong friendships. Especially, I would like to express my most sincere thanks to Esma Derin, Eylül Yılmaz, Yusuf Aslan, Murat Güngen, Nedim Hacıosmanoğlu, Beyza Küçük, İrem Kaya, İrem Sena Karagözler, and Dr. Özgecan Erdem for their exceptional companionship during this long marathon. They always make me laugh even at my tired moments. Their support and expertise in academia clearly made me see things from a different perspective.

I would like to state my special thanks to Esma Derin. Together, we pursued interesting scientific solutions, which significantly eased my adaptation to the laboratory in my first year. Her encouraging liveliness kept me motivated all the time.

I would like to state my thanks to Mina Aşkun, Zeynep Tunalı, Saeedreza Zeibi Shirejini, Barkan Kağan Durukan and Dr. İsmail Eş for their fruitful collaboration. Together we managed to publish in the high-quality journals.

I would like to express my special thanks to Assistant Prof. Dr. Yeşeren Saylan and Hacettepe University for their support in terms of TÜBİTAK ARDEB 1001-Scientific and Technological Research Projects Funding Program (Project No: 120Z445).

I would like to greatly acknowledge the M.Sc. scholarship supported from TÜBİTAK ARDEB 1001-Scientific and Technological Research Projects Funding Program (Project No: 120Z445).

I would like to acknowledge the M.Sc. scholarship from UNAM (Bilkent University UNAM Graduate Fellowship for M.Sc. students). I am appreciated to give a myriad of opportunities. I will always remember UNAM's help and remarkable support.

I would like to thank Prof. İhsan Doğramacı, the founder of Bilkent University. Prof. Doğramacı's endless pursuit inspired me to reach perfection and open-mindedness in my research career.

I would like to take this opportunity to give my tribute in memory of Prof. Dr. Mehmet Mutlu who taught me many techniques and tools, which significantly raised my knowledge in my first years of academia. Rest in Peace, Prof. Mutlu.

I would also like to express my special thanks to TOBB University of Economics and Technology for their remarkable support in my Bachelorette of Biomedical Engineering.

Last but not least, I would like to dedicate this thesis to my family Onur Sağdıç,

Cenan Sağdıç and Hanım Hande Sağdıç. I owe my accomplishments to them. Their support has always kept me motivated. They always supported me with their endless love. I am proud of being their son. I work really hard for days and nights to elevate their honor and name. I promise to be an honorable and trustable man until the end of my life.

Contents

List of Figures

List of Tables

ABBREVIATIONS

Circulating tumor cells	: CTCs
Circulating tumor microemboli	: CTM
Transforming growth factor β	: TGFβ
White blood cells	: WBCs
Red blood cells	: RBCs
Cytokeratin	: CK
Epithelial cell adhesion molecule	: EpCAM
Epithelial to mesenchymal transitions	: EMT
Mesenchymal-epithelial transition	: MET
Reverse transcription-polymerase chain reaction	: RT-PCR
Nucleic acid-based fluorescence *in situ* hybridization	: FISH
Reverse transcription quantitative-PCR	: RT-qPCR
Di-electrophoresis	: DEP
Flexible micro spring array	: FMSA
Micro-nuclear magnetic resonance	: μNMR
Size-dictated immunocapture chip	: SDI-Chip
Herringbone microfluidic chip	: HB-Chip
Deterministic lateral displacement	: DLD
Strep-Tactin-coated magnetic beads	: STMBs
Ultraviolet	: UV
Near-infrared	: NIR
Streptavidin	: SA
Particles-integrated herringbone CTC chip	: NP-^{HB}CTC-Chip
N-isopropylacrylamide	: NIPAAm
Lower critical solution temperature	: LCST
Graphene oxide	: GO
Polydimethylsiloxane	: PDMS
Bovine serum albumin	: BSA

Avidin-fluorescein isothiocyanate	: Avidin-FITC
3-mercaptopropyl-trimethoxysilane	: 3-MPS
Silane-polyethyleneglycol-thiol, 1 kDa	: Silane-PEG-SH 1k
Silane-polyethyleneglycol-thiol, 5 kDa	: Silane-PEG-SH 5k
2,5-diphenyl-2H-tetrazolium bromide	: MTT
Atom transfer radical polymerization	: ATRP
Cationic surfactant cetrimonium bromide	: CTAB
Tetraethoxysilane	: TEOS
Aminopropyltriethoxysilane	: APTES
α-Bromoisobutyryl bromide	: BIBB
Triethylamine	: TEA
Tris[2-(dimethylamino)ethyl]amine	: Me_6TREN
2-Bromoisobutanoic acid *N*-hydroxysuccinimide ester	: NHS-ester
Scanning electron microscope	: SEM
Energy dispersive X-ray spectroscopy	: EDX
Transmission electron microscopy	: TEM
Fourier transform infrared spectroscopy	: FTIR
X-ray diffractometry	: XRD
Nuclear Magnetic Resonance	: NMR
Size Exclusion Chromatography	: SEC
Differential Scanning Calorimetry	: DSC
Molecular weight	: M_n
Tetramethylsilane	: TMS
Polydispersity index	: PDI
Glass transition temperature	: T_g
Cloud points	: CP
The hydrodynamic	: HD

Brunauer–Emmett–Teller : BET

Polymethyl methacrylate : PMMA

Double sided adhesive layer : DSA

Polytetrafluoroethylene : PTFE

N-γ-maleimidobutyryl-oxysuccinimide ester : GMBS

Self-assembled monolayers : SAMs

Precision Etching and Coating System : PECS

Estrogen receptor : ER

Progesterone receptor : PR

Human epidermal growth factor receptor : HER

Fetal Bovine Serum : FBS

Dulbecco's Modified Eagle's Medium : DMEM

Ethylenediaminetetraacetic acid : EDTA

Filter 1 : FL1

Ultrapure water : UPW

Chapter 1

CONCEPTS in CAPTURE and RELEASE of CIRCULATING TUMOR CELLS and EMBOLI

Declaration of Copyright

This work is partially described in the following publication [1].

Kutay Sagdic 1,2 and Fatih Inci#,1,2,

1 UNAM-National Nanotechnology Research Center, Bilkent University, 06800 Ankara, Turkey

2 Institute of Materials Science and Nanotechnology, Bilkent University, 06800 Ankara, Turkey

#Corresponding author: finci@bilkent.edu.tr

Adapted with permission from Sagdic, K., Inci, F. (2022). Smart Material-Integrated Systems for Isolation and Profiling of Rare Cancer Cells and Emboli. Advanced Engineering Materials, 24(3), 2100857.

License Number: 5332510580640

1.1 INTRODUCTION: Cancer Metastasis, EMT, and MET Transitions

Cancer leading to an annual casualty of 9.6 million people worldwide and 116,710 cases in Turkey, depends on multiple parameters such as age-group, geography, regional gene-diversity, and many genetic/epigenetic factors. Personalized healthcare for cancer patients relies on identifying molecular indicators in disease because oodles of diverse cells join the circulation throughout carcinogenesis [12, 13]. The existing orthodox techniques to isolate rare cancer cells focus generally on the biomarkers, predicting treatment measured from biopsy samples [14]. Due to a wide-ranging area of cancer encompassing versatile disciplines, unfeasible invasive systems, cancer cell progression, and limited repertoire of targeted treatments have been encouraged us to elaborate new techniques and modalities in monitoring approaches that foresee the future journey of rare cancer cells much more ideally [15]. To hurdle associated obstacles, one of the new-fangled avenues is circulating tumor cells (CTCs), and roughly 3-100 cancer cells form the clusters called circulating tumor microemboli (CTM) [16, 17, 1]. CTCs/CTM holds great potential to provide real-time information and non-invasive snapshots of genetic intratumor heterogeneity and they are better than those of any single-site biopsy techniques [18, 19]. As CTCs/CTM have been spanned the area of tumor metastasis and invasion, they have been conjured up prognostic [20], pharmacodynamic [21], biomarker utility [22], and identification [23] for therapeutic therapy [24] (**Figure 1.1**).

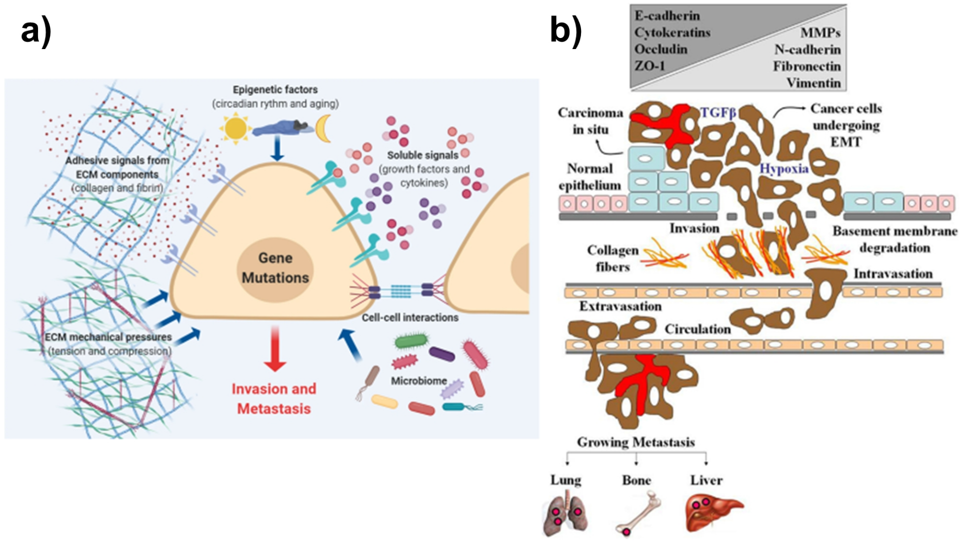

Figure 1.1: **a)** The process of invasion and metastasis is associated to cell-ECM and cell-cell adhesive signals; ECM automated pressures; intratumoral microbiota; soluble signals in the ECM; and epigenetic reasons. **b)** EMT is described by the deficit of epithelial markers and regulated by different effectors, such as growth factors (TGFβ). (Reproduced from Ref. [1] with permission from John Wiley and Sons, [2] with permission from Springer Nature, [3] with permission from Frontiers Research Foundation.)

A myriad of studies have been presented the clues in discovering the role of CTCs within metastasis [25]. In particular, the aggregates or clusters of tumor cells are associated with higher metastatic risk [26, 27]. In these aforementioned reports, rare cancer cells have been varied in size, density, shape, concentration, and internal structure belongings to estimate the metastatic potential [28, 29, 30]. With recent methods, DNA and RNA characteristics of CTCs have been studied for defining the scale of heterogeneity through single-cell profiling or aggregation techniques, yet the main challenge in CTCs examination is their low abundance (1-3000 CTCs/mL [31]) in blood circulation (10^7 white blood cells (WBCs) per mL; 10^9 red blood cells (RBCs)/mL [32, 33, 34]). To tackle this challenge, CTCs are primarily detected with cytokeratin (CK) cytoskeletal protein and epithelial cell adhesion molecule (EpCAM) surface protein whereas they are negative for

WBC-specific CD45 surface protein. Heretofore, mesenchymal CTCs have been contrarywise identified due to down-regulation of EpCAM or CK biomarkers, epithelial to mesenchymal transitions (EMT), and mesenchymal-epithelial transition (MET) [35]. On the progression of embryonic development and wound healing, EMT happens, yet if the tumor environment disarranged this progression in the rareness of EMT-inducing signals with prompting regulators of EMT, which are growth factor-β and hepatocyte growth factor/scatter factor, the process may reverse to MET.

Furthermore, researchers have spent many years to know-how the function of CTM that could be identified in human peripheral blood. In particular, the ubiquitous phenotypic and functional properties of CTM are foremost for the progression of metastases because they have the capability to avoid immune surveillance [36], avoidance of anoikis [37], and traveling niche [38] thanks to the presence of stromal cells [39]. Besides, CTM is described as a rip from primary and pivotal tumor mass clusters [16]. The incompetence and rarity of isolation methods of CTM limit our knowledge about their origin, consisting markers, and the relationship with metastasis. There are therefore acquirement needs for novel methods to effectively isolate and release the rare number of CTCs from blood in order to enlighten pathophysiological and biological characteristics.

1.1.1 Biological Origin and Characteristics of CTCs/CTM

To isolate CTCs, the expression of cell surface biomarkers, i.e., CD45(-) and EpCAM(+) are omnipresent biological possessions that guide methodologies to design and elaborate recognition elements (antibodies and aptamer), for instance, anti-EpCAM antibodies, anti HER2/neu antibodies, anti-CD5 antibodies, anti-EGFR antibodies to identify CTCs with a decent specificity [40].

1.1.2 Molecular Characterization of CTCs/CTM

Due to the extreme rarity and excessive heterogeneity of CTCs/CTM, advanced characterization methods are needed to isolate these cells much more reliably. The tools for this aspect could be categorized, but not limited to, antibody-based methods, physical asset-based techniques, and other detection methodologies [39]. Antibody-based techniques are mainly used as cell capture methods, and among them, EpCAM is the most frequently employed biomarker for this manner. The cellular beginning of CTCs can be ascertained from primary and metastatic tumor deposits, thereby physical property differences in dielectric properties, cell size, mechanical plasticity, and density can be engaged to detect CTCs, possessing distinct physical belongings compared to blood cells. Flow cytometry or protein-assisted immunofluorescence (CellSearch®); reverse transcription-polymerase chain reaction (RT-PCR), nucleic acid-based fluorescence in situ hybridization (FISH), reverse transcription quantitative-PCR (RT-qPCR), sequencing or microarrays are the additional assay-based methods [41]. To identify CTM, the most frequently employed batch purification systems are likely to disturb the cellular aggregates so that a number of additional technologies have been launched to isolate CTM under favour of the physical and biological signs of epithelial cells as mentioned earlier.

1.1.3 Versatile Research/Clinical Methods for Isolation of CTCs/CTM

Specifying CTCs/CTM biomarkers is challenging because of inter/intra patient heterogeneity in cancer cell biology. In contrast, these belongings would be used to isolate, distinguish, and detect CTCs/CTM against billions of RBCs and WBCs in the bloodstream. In a few words, smart materials such as bioconjugates, aerogel-created polymers, metal foams, nanofibers, shape-memory materials, and piezoelectric constituents have been employed in terms of CTCs/CTM isolation [42, 43, 44]. The most commonly employed physical isolation strategies involve deformability and size-based [45, 46], electrical property-assisted dielectrophoresis (DEP) separation [30], and density-gradient centrifugation [43]. In other respects, the isolation methodologies relying on biological characteristics are mainly either (i) a positive selection—aiming surface biomarkers especially for the phases of metastasis or (ii) a negative selection-stemmed from the depletion of blood cells [35]. Apart from the conventional methods, batch purification methods and microfluidic devices are employed currently in isolating CTCs/CTM [47, 48]. Isolating CTCs holds notable struggles that involve low recovery, purity, and enrichment yield. Highlighting again, the enrichment of cancer cell clusters/aggregates is more challenging than those for the approaches of capturing single tumor cell due to the limited lifespan and rarity.

1.1.3.1 Performance Metrics of Platforms for CTCs/CTM Isolation

To compare performance metrics of all the techniques, the performance of CTCs/CTM enrichment technologies benchmark with the next parameters: (i) capture yield, (ii) capture purity, (iii) capture throughput, (iv) enrichment yield, (v) cell viability, and (vi) clinical yield percentage. The efficiency of isolation depends on the lowest number of CTCs revealed per specimen, which is vital for pre-diagnostic circumstances **(Equation 1.1)**. Capture purity yield is the relation ratio of detected CTCs compared to all captured cancer cells from a spiked specimen **(Equation 1.2)**. Capture throughput is the amount of cancer cells injected per period of time. Indeed, for microfluidics, the capture throughput is the velocity of the platform, and it can be derived from the volumetric flow rate **(Equation 1.3)**. Enrichment rate is the ratio of CTCs to blood cells (WBCs and RBCs) before and after the isolation **(Equation 1.4)**. The viability of tumor cells can be described in **(Equation 1.5)**. Clinical yield percentage is the average number of tumor cells isolated from patients with a recognized cancer phase **(Equation 1.6)** [49, 50, 51, 19]. All these equations are also described and formalized as follows:

$$CaptureEfficiency_{TumorCells} = \frac{TumorCells_{Output}}{TumorCells_{Input}} \tag{1.1}$$

$$Purity_{TumorCells} = \frac{TumorCells_{Recovered}}{TumorCells_{Recovered} + BackgroundCells_{Input}} \tag{1.2}$$

$$CaptureThroughput_{TumorCells} = \frac{VolumetricFlowRate}{Time} \tag{1.3}$$

$$Enrichment_{Rate} = \frac{(TumorCells/BackgroundCells)_{Recovered}}{(TumorCellsBackgroundCells)_{Sample}} \tag{1.4}$$

$$Viability_{TumorCells} = \frac{ViableTumorCells_{Recovered}}{TumorCells_{Recovered}} \tag{1.5}$$

$$ClinicalYieldPercentage_{TumorCells} = \frac{TumorCells_{Recovered}}{TotalVolume} x100 \tag{1.6}$$

1.1.3.2 Conventional Methods

Versatile approaches for the batch purification—the earliest techniques in isolating single CTCs, have been engaged to versatile cells according to immunomagnetic characteristics and density gradient of rare cancer cells [29]. Apart from that, magnetic affinity-based selection is a widely used technique to detect CTCs from patient specimens. CellSearch® is named as a “gold standard”, and until now, it is the only and first CTCs identification assay validated by the FDA as a prognostic technology for patients with metastatic colorectal, breast or prostate cancer [17]. By employing EpCAM(-) coated magnetic beads, enumeration of epithelial-originated CTCs can be performed [47]. After capturing, magnetically-labeled tumor cells are extracted by applying a nuclear stain DAPI(+) and a distinct magnetic field [52]. Moreover, fluorescent-labelled antibodies can be employed for distinguishing cancer cells from white blood cells according to CTCs surface biomarkers including CK(+), CD45(-), and EpCAM(+). However, this conventional techniques have some challenges, such as (i) extreme background signals because of the sensor contagions caused by RBCs and WBCs [17], (ii) limitations to observe the subpopulation of cancer cells undergoing the EMT [53], and (iii) the low recovery rate of CTCs [54].

1.1.3.3 Physical, Immunologic, and Magnetic Affinity-Based Strategies

Physical properties of CTCs and CTM for isolation methods depend on many distinctions in physical assets, including deformability, size, density, distinguishable phenotypes between leukocytes and CTCs or electrical polarizability [55]. The discrimination of CTCs can be performed through the size differences of epithelial tumor cells (ISET® [56] and ScreenCell® [57]). Briefly, ISET® extracts CTCs from the blood samples in size and deformability aspects, thereby improving the cell recovery rate [56]. Thanks to the larger sizes of EMT subpopulations than that of leukocytes of peripheral blood, CTCs can be isolated by the filtration method. Regardless of these precious characteristics, the struggles of ISET® with filtration are high background signals due to WBCs and low CTC recoveries (∼50%) [58]. From another perspective, a well-designed flexible micro spring array (FMSA) technology has been facilitated for minimizing cell injury to enhance cell viability of CTCs/CTM via changing the design parameters (aspect ratio) of a microfluidic chip that decreases shear stress. Moreover, a microfiltration method (CellSieve®), designed with high porous decorations running under low pressure, is fabricated to detect CTCs through the size exclusion and their subsections whilst sustaining intracellular contents [59]. According to physical approaches, investigating the cellular phenotypes of tumor cells would be a key to gain insight into isolation techniques, cell-microenvironment relations, metastatic cascade of cancer cells, and capacity of cell invasion. Comprehensive examinations of CTCs/CTM adhesion, motility, and drug response may be an effective way to devise and deliver deeper insights into isolation techniques [60].

Besides, immunocapture-based methods usually accomplish high-throughput isolation of CTCs/CTM via cell surface biomarkers with exceedingly specific interactions between antigen and antibody. For this purpose, immobilization of positive binding ligands is mostly employed on the nanostructures. As an example, fluorescent in situ hybridization (FISH) was designed for both CTCs and CTM isolation via integrating immunostaining methodology [61, 62]. Additionally, a clinically feasible Epic CTC Platform was launched to assess analytical performance by using immunofluorescence labeling and genetic biomarkers in the spiked samples collected from a liquid biopsy of prostate cancer patients and healthy donors [63].

Magnetic affinity-based isolation is another technique to distinguish rare CTCs/CTM from unfractionated blood samples with a high purity rate [1]. As mentioned, even though CellSearch® is the first validated cancer cell isolation platform using magnetic fields [59, 31], the immunomagnetic and density gradient cell separation reliant methodologies are some of the primary presented technologies for isolation of CTM from whole blood [64, 65]. Most of the immunomagnetic methods combine antibodies with functionalized and operable magnetic nanobeads to detect CTCs/CTM [58, 66]. Bestowing reliable, reproducible, and functional ways are the foremost solutions of these methods; but they still have some obstacles regarding poor detection range, optical analysis, and imaging because of extreme antibody saturation on the surface of beads [67]. MagSweeper, for instance, addresses some challenges in leukocyte contamination and improves the limited methodological sensitivity via a robotic liquid biopsy device by purifying alive CTCs capably via magnetic rods enclosed in plastic sleeves [66, 17]. Numerous innovative technologies, including micro-nuclear magnetic resonance (µNMR) [68], MagSifter [69, 70], Maglev [71], and MagDense [72] are the other platforms under the umbrella of immunomagnetic split-up for CTCs/CTM.

1.1.3.4 Microfluidics Isolation Methods

Microfluidics—consisting of chambers, valves, and microchannels, stereotypically manipulates liquids at a micrometer level with high sensitivity, specificity, throughput, and compatibility manners [73, 74]. This methodology requires three fundamental actions including testing, processing, and finally validation. In terms of enrichment of rare tumor cells, the isolation capability of microfluidics comes from either (i) passive approaches that modify microfilters of varying flow chamber geometries [75], pore sizes [76], flow density [77], and microstructures [70] or (ii) active methods relying on magnetic susceptibility [70], compressibility [78], and polarizability [79]. For analyzing and enumerating CTCs/CTM, the surface chemistry in microfluidics needs precise control for capture and release functionality. For example, a surface-functionalized microfluidic platform (CMx platform) [80], a size-dictated immunocapture chip (SDI-Chip) [76], and a passive mixing within a wavy-herringbone microfluidic chip (HB-Chip) [81] have been performed to isolate and characterize CTCs/CTM. Apart from that, numerous label-free microfluidics have been employed to isolate CTCs/CTM from the chip microenvironment. As an example, a microfluidic chip, i.e., the Cluster-Chip, isolates cancer cell clusters from the blood through tumor-specific biomarkers and bifurcating traps under a low profile of shear stress [82]. In addition, Parsotrix™ cell separation platform provides biomarker independent isolation of CTCs along with their deformability and size with a 99% of viability and 42-70% of capture yield range [83]. Lastly, another microfluidic chip is designed on a deterministic lateral displacement method that depends on size separation of CTCs and WBCs from whole blood. It employs a passive method via two separate operational parts that are used to initially perform magnetophoresis for inertial focusing, precise positioning, and separating rare cancer cells. It is then employed for depleting antibodies against leukocytes, resulting in a 97% rate of CTCs [84].

Chapter 2

SMART MATERIALS for ISOLATION of CANCER CELLS

2.1 INTRODUCTION: The Significance of Isolating/Releasing CTCs/CTM

Once CTCs/CTM are captured specifically, the origin and heterogeneity of tumor cells are needed to understand for introducing the most effective treatment. Releasing or isolating CTCs/CTM from the enriched platforms is a mainstay in this manner. Focusing on this regard, the way of cancer cell release provides molecular analysis, phenotype identification, and culture expansion of captured CTCs/CTM. At this point, surface functionalization with specific chemistry approaches is one of the most crucial point that allows the controllable release of cancer cells. During this process, there is a potential risk that cancer cells might hold some contaminations or have some structural damages that could hinder downstream analyses. Releasing process needs to fulfill the highest levels of performance metrics, and thus, the mode of action requires to be highly gentle and very specific for accurate investigation of CTCs/CTM transcriptome, proteome, and genome. As an example, the low impurity of CTCs/CTM obfuscates their downstream molecular profiling and disturbs true positive signals in the situation of low intact cell viability [47]. To tackle these encounters, CTCs/CTM release technologies would occur via thermal modes or mechanosensitive, enzymatic, self-assembly, and chemical interactions with the integration of smart materials (**Figure 2.1**).

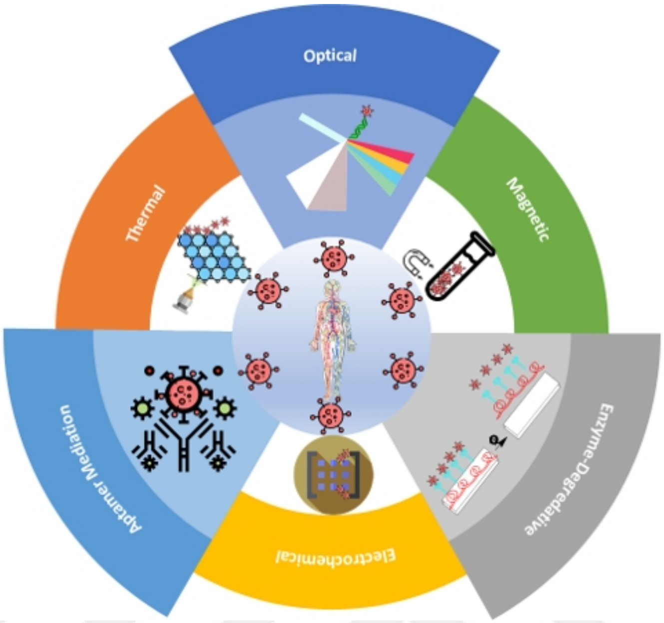

Figure 2.1: The need for CTCs analysis is expressed via smart release mechanisms with various external stimuli including optical, thermal, ligand competitive, magnetic, aptamer mediated, electrochemical, enzyme degradative, and affinity-based strategies. (Reproduced from Ref. [1] with permission from John Wiley and Sons.)

2.1.1 Smart Material-integrated Release Strategies of CTCs/CTM

Smart materials can passively or actively alter their original properties according to external stimuli [85]. Not only changing conformation but also conveying and converting an energy form to an alternative form is the foremost ability of smart materials. In particular, considering releasing/isolating the captured CTCs/CTM, smart materials-assisted emerging technologies have displayed a remarkable impact on the course of isolation of rare tumor cells [86]. In contrast, there are still obstacles that hinder the release process in this regard, including (i) inaccurate properties of smart materials; (ii) high-adherence ratio to the captured platforms; (iii) or limitations on construction platform aspect ratio and dimensions; (iv) limited repeatability; (v) non-sustainability; and finally, (vi) poor data management [87]. In this manner, combining well-designed, fabricated, and characterized smart materials with convenient chemical modifications and topological structures would be the keys for addressing accurate, facile-to-use, efficient, and label-free isolation platforms. For example, smart bionanomaterials such as particles, hydrogels, conjugates, nanofibers, and shape memory materials are commonly employed in the area of rare cancer cells isolation and release [88, 44]. In this chapter, we have comprehensively elaborated on the developmental fashions, impediments, and next-generation methodologies of smart material-integrated approaches (**Figure 2.2**).

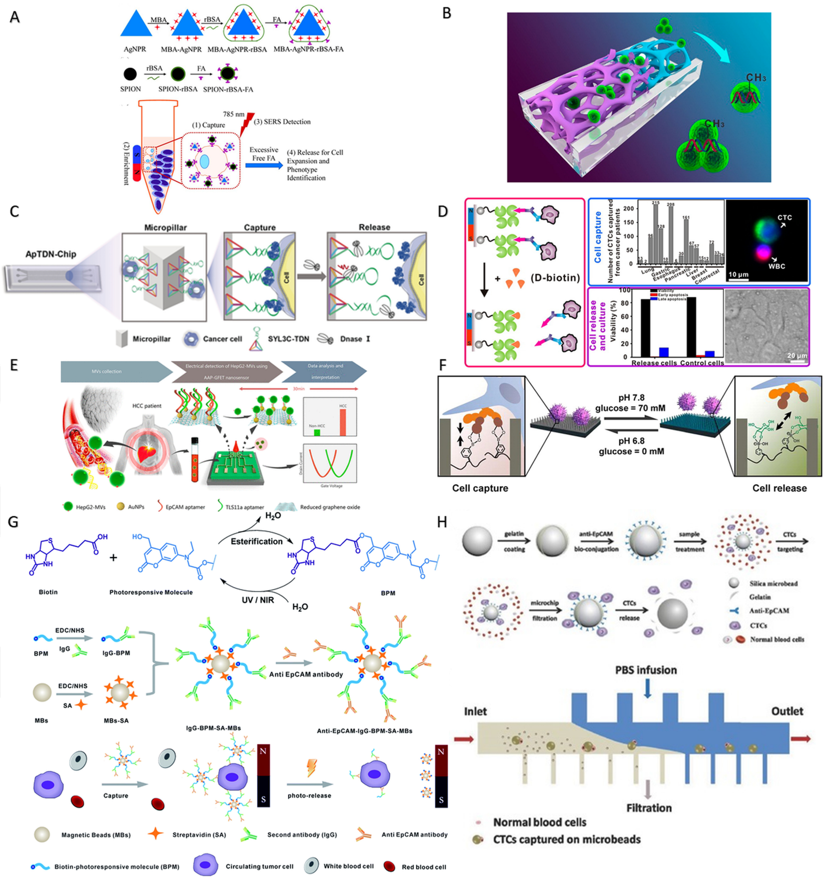

Figure 2.2: Versatile smart-material integrated release strategies are presented. **a)** CTCs analysis system relies on silver particles [4] **b)** Thermoresponsive 3D scaffold chip is employed for the CTC isolation [5] **c)** The workflow of the aptamer-mediated chip is presented [6] **d)** Protein-triggered immunomagnetic beads is used for the CTC isolation [7] **e)** Electrical-based detection strategy is presented [8] **f)** Dual-sensitive surface is demonstrated for the isolation of CTCs [9] **g)** Photosensitive magnetic system is used for the isolation of CTCs [10] **h)** Isolation of CTCs is employed through size amplification strategy [11] (Reproduced from Ref. [1] with permission from John Wiley and Sons, [4] with permission from ACS Biomaterials Science & Engineering, [5] with permission from Analytical Chemistry, [6] with permission from Angew Chemie International Edition, [7] with permission from ACS Applied Materials & Interfaces, [8] with permission from Analytical Chemistry, [9] with permission from Journal of the American Chemical Society, [10] with permission from Chem Science Journal, [11] with permission from Advanced Healthcare Materials.)

2.1.2 Different CTC/CTM Isolation Methods

In this section, we denote a myriad of applications in releasing tumor cells with different strategies. First of all, aptamers—single-stranded DNA/RNA peptides or oligonucleotides that precisely fold into secondary and tertiary configurations to identify the targets, are widely used for the isolation of CTCs [89]. The aptamers have predominant features including rapid response, high reproducibility, affinity, small size, ease of modifiability, and non-toxicity as a biorecognition element bringing them prominent specialties in cancer cell release [90]. Under favor of aptamers, the isolation of rare cancer cells has been enabled with an alternative strategy to antibodies as affinity ligands. Moreover, the aptamers would lose specificity and affinity by changing their conformation, which results in allowing a number of alternatives to release CTCs/CTM. For example, a well-oriented and deterministic lateral displacement (DLD)-patterned microfluidic chip (ApTDN-Chip) was designed to isolate CTCs via the enzyme degradation of aptamers via a tetrahedral DNA scaffold with a suspended aptamer graft [6]. The tetrahedral DNA nanostructure both helped to reduce the local overloading effect to make aptamers more reachable to DNA nuclease and controlled the arrangement of aptamers for increasing target-aptamer interaction. In addition, the DLD patterns elevated the number of collisions between micropillars and CTCs which enabled 60% of capture efficiency and 83% of release efficiency along with 83% of cell viability.

In functionalizing with diverse antibodies (blood cells (negative enrichment) or by CTCs (positive enrichment)), magnetic particles are mostly employed for the extraction of tumor cells [54, 53]. The main idea in the course of applying a proper magnetic field is to discriminate aptamer-coated magnetic particles which are holding CTCs from the surface of the platform [91]. The key factor for this approach is the cell recovery yield of the immunoaffinity-integrated magnetic particles, which depend on the expression level and integrity of the antibody binding epitopes of the target antigen [92, 58]. For example, an immunomagnetic platform coupled with anti-EpCAM antibodies, anti-EGFR antibodies, and anti-HER2 antibodies was used to isolate CTCs [7]. Moreover, after the release of

CTCs, an ex vivo culture of viable CTCs was executed for enabling a genotype of the primary tumor cells. For capturing the cells, Strep-Tactin (a mutated streptavidin molecule with the biotin-binding site)-coated magnetic beads (STMBs) were employed. Strep-tag II (a short peptide sequence)-derived antibody-STMBs and Strep-Tactin were used as a capture agent, and by introducing biotin to the system, Strep-tag II-derived antibody was removed from STMBs so that CTCs were released. As a result, $\sim$70% of captured cancer cells were released, and approximately 85% of the released tumor cells have sustained viable.

Electrochemical-based sensing enables quantitative investigations in releasing CTCs/CTM through the redox states of microsystems. Electrochemical type of stimuli-sensitive materials can be employed by applying a decent amount of voltage to the surface of the electrode to change the adhesion rate and conformational transition of the particles [93, 94]. By looking into current, potential, conductance, impedance, and scan rate alterations of CTCs isolation technologies, the paradigms of rapid response and efficiency can be integrated into those of smart material-assisted techniques. However, the sensing abilities of electrochemical platforms would be insufficient because CTCs/CTM could be isolated in trace numbers from the bloodstream. Moreover, the accuracy of cancer cell detection would be also a challenge due to the fact that the complex protein structure of the cancer cell membrane causes complications of specification. Therefore, the electrochemical-based platforms have been generally harmonized with versatile materials, including particles, immunoassays, magnetic beads, transistors, composites, nanosheets, and nanowires [95, 96, 97, 98, 8, 99].

From the perspective of the affinity-based CTCs/CTM isolation, 3D nanocomponent-modified elements are employed owing to local topographic interactions of the cellular agents on the surface at the same level. Digestion of these nanostructures would be a promising strategy in the course of cancer cell release [100]. For instance, a photo-responsive immunomagnetic delivery agent was designed for CTCs isolation with a photo activator 7-Aminocoumarin bridge to modify the anti-EpCAM antibodies with magnetic beads [10]. Under near-infrared (NIR) light illumination and ultraviolet (UV), C-O bonds were created by the coumarin moieties amid capture antibody and streptavidin (SA)-functionalized immunomagnetic beads. After the cleavages were damaged, CTCs were released with yields of 73% ± 4% and 52% ± 6% on the course of UV light irradiation and NIR, whereas 90% and 97% of these cancer cells were viable in those of irradiation circumstances.

The ligand competition-based release is a favorable way to generate more steady chemical bonds by applying ligands with robust affinities. Owing to this ubiquitous technique, not only available experimental conditions, but also the selection of an appropriate approach are quite achievable [101, 102]. For example, an HB-Chip with a thiol-functionalized ligand-exchange reaction via NHS-modified gold particles (NP-^{HB}CTC-Chip) was fabricated to isolate breast cancer cells from whole blood [103]. The nanopatterned configurations of the microfluidic chip leveraged precise interactions between antibodies and tumor cells, whereas the thiol molecules exchanged antibodies and ligands through the thiol–metal interactions. Moreover, the high release yield of the captured cancer cells was provided thanks to the enhanced the surface area via NP assemblies.

Applications of external-stimuli mainly comprise thermoresponsive, photosensitive, and hybrid (combination of at least two stimuli) methods. Revealing the photoresponsive platforms, light is one of the most important external stimuli that triggers off the molecular arrangement of materials including alterations in surface charge, diameter, and size [85]. In this manner, light can be applied plausibly in a feasible manner as its maneuverability of being controlled elegantly to illuminate the interfacial nature of systems [104, 105, 106]. Hence, light-stimuli moderated platforms would also have controlled the harvesting of rare cancer cells. As an example, for the immunocapture and then site-release of single CTCs, a near-infrared (NIR) light-responsive platform was constructed through the utilization of gold nanorods-conjugated with a thermoresponsive gelatin hydrogel. The hydrogel was thawed at body temperature (37 °C) and this changed surface property and aided the bulk release of the captured tumor cells [104]. By combining anti-EpCAM antibodies with gelatin-based hydrogels, the yield of the capture of MCF-7 cells was found as 92% ± 6%, and the yields of cancer cell release from the small and bulk regions revealed as 92% ± 6% and 95% ± 4%, respectively.

Thermoresponsive methods can also be employed in aspects of the release of captured tumor cells via utilizing either carbon-based or polymers materials to enhance the cell viability of the isolated CTCs/CTM [107]. In this manner, graphene-utilized polymer compounds, polypyrrole, poly(N-isopropyl acrylamide (poly(NIPAAm), p(NIPAAm)) or hydrogel-grafted surfaces/brushes have been preferred generally due to hydrophobic-to-hydrophilic phase transition at lower critical solution temperature (LCST) [5, 108]. For instance, a tunable thermoresponsive device consisting of graphene oxide (GO) and poly(N-acryloyl piperidine-co-N, N-diethyl acrylamide) copolymer compound was designed for capably capture and reversibly release of CTCs on a device of microfluidic [109]. As the LCST is low as 13 °C, this made downstream assay, molecular investigation, single-cell analysis, and FISH analysis possible even at room temperature. The platform was modified by decorating anti-EpCAM antibodies and the highest capture yield of 95.21% was achieved at a 17 µL min^{-1} flow rate, and the release yield of 91.56% in blood and 95.21% in buffer were obtained while keeping 91.68% of cell viability. Additionally, a thermoresponsive hydrogel-incorporated gelatin into self-assembled (polydimethylsiloxane) PDMS scaffold microfluidic chip has been presented for isolation of both CTC and CTM by forcing tumor cells undergoing chaotic migration or vortex [5]. Gelatin material dissolves at 37 °C and above this temperature, the feature of the chip has a phase transition behavior from a hydrophilic swollen state to a hydrophobic collapsed state to enable tumor cell release. Respectively, the immobilization of sulfo-NHS-biotin, streptavidin, and anti-EpCAM antibodies allows the capture of MCF-7 cells which provided 80% of recovery yield and high capture efficiency of CTCs/CTM with more than 90% viability at the range of 34-3.4 µL min^{-1} of flow rates.

2.2 DESIGN: Bioinspired Smart Polymers/Materials

2.2.1 Sources of Inspiration

Blood holds crucial information and contains distinct biological molecules, disease biomarkers, and cell types. In particular, CTCs are released from the primary tumor and spread to different regions to nearby or distant organs through the bloodstream. Hereinto, metastasis is one of the most pivotal steps of cancer, comprising 90% of cancer-related deaths. Studies disclose both positive responses to treatment and significant reductions in associated-costs with treatment/diagnosis when cancer is detected in early stages. Researches on CTCs, therefore, would have a significant role in diagnosing cancer at very stages possible. The approach of "liquid biopsy" enabling the isolation and characterization of CTCs holds an unprecedented impact in this regard.

Briefly, CTCs are isolated from circulation with diverse strategies. Due to their very low abundancy and heterogeneity of blood in early-stage cancer patients, detecting and isolating CTCs via conventional methods are however challenging due to high-cost, lengthy process, and the need for sophisticated facilities narrowing their utility for early-stage diagnosis **Table 2.1**. Although microfluidic-based platforms offer an opportunity to work with minute sample volumes, a limited surface area significantly diminishes the capture yield. Furthermore, releasing the captured CTCs and analyzing them is crucial to decipher cancer progression and provide proper clinical management. The cell release strategies are basically reliant on enzymatic, magnetic, optical, aptamer/affinity-based, and polymeric systems interfere with the unity of the cell surface. However, they lose their specificity due to high-sensitivity to the environment, and they require labelling steps that increase the cost and complexity of assay drastically. Hence, there is an urgent need for novel methods that effectively isolate and release a rare number of CTCs from blood and at the same time, address these existing challenges in cost-, complexity-, and efficiency-perspectives.

Table 2.1: CTCs isolation methods, technology types along with their advantages and limitations.

Method	Type	Advantage	Limitation	Refs
Conventional laboratory methods	CellSearch, Fluorescence *in situ* hybridization (FISH)	Easy-to-use, well-known methods	Time, Sensitivity, and Reliability	[29]
Physical principles for isolating CTCs/CTM	3D micro-filtration, CellSieve	High-throughput	Loss of CTCs with size equal to and smaller than the pore size of the filter	[55]
Immunocapture of CTCs/CTM	Next-generation sequencing	High specificity	Loss of CTCs subpopulations	[104]
Microfluidics Isolation Methods	Surface-coated Microfluidic Chip (CMx platform)	CTCs separation *via* an array of parallel and alternating microchannels	CTCs damage due to hemodynamic stress	[81]
Magnetic affinity-based Selection	MagSweeper, CTC-Chip (Ephesia)	Enable capture of different phenotypes of CTCs/CTM	Low specificity	[72]
Batch purification methods	Herringbone (HB)-Chip	Low Shear Design, Enhanced Mixing	Loss of CTCs with high density	[47]

Thanks to their analytical performances and unique functions, smart material-assisted strategies, hold a notable impact on not only CTCs detection and also on CTCs identification and isolation from the circulation. However, a myriad of obstacles including manufacturing defects, cost, and energy efficiency, are encountered once smart materials deploy from lab bench to industry. Moreover, there is a gigantic demand for advanced emergent systems to procure efficient, easy-to-produce, affordable, controllable, and consistent manufacture. Prior to engaging clinical approaches, these above-mentioned challenges require to be fulfilled and considered.

To tackle these aforementioned obstacles, smart particles have been manufactured with significant abilities such as passive retention mechanisms, overcoming non-specific cellular uptake, and therapeutic potential via cell, gene, drug, and protein delivery systems [1, 110, 111]. Among all the smart particles, silica particles are ubiquitous materials due to their thermal and physicochemical stability, biocompatibility, nontoxicity, controllable structure, and ease-of-surface modification [112, 113]. Silica particles have attracted much attention because of their mesostructural feature that provides facile functionalization for health-care platforms including diagnosis, biosensors, and delivery systems [114]. Particularly, hollow silica particles endow a large specific surface area, enhanced optical performance, low density, adjustable pore diameter, increased pore size, and external surface functionalization [115, 116]. Controlling the shape and size of hollow silica by bio-mimicking and bio-inspired strategies alter, enhance, control, and tune the interactions between surface-biomolecule via controllable surface areas, pore volume, pore size, and diameter.

On the other hand, numerous conditions such as the paucity of appropriate surface functionalization methods, limitations in biomolecule loading capacity, and non-specific interactions of hollow silica particles, necessitate facile functionalization of silica surfaces by one-spot synthesis (co-condensation) and/or post-synthesis (grafting) [113]. For the purpose of detecting, carrying, and isolating biomolecules, a myriad of approaches have been launched for making surfaces of silica particles functional such as chemical treatments, grafting with monoclonal antibodies, introducing inorganic nanomaterials, biomacromolecules, host-guest assemblies, and polymer gatekeepers [117, 118, 119]. Apart from all mentioned methods, poly(N-isopropylacrylamide) or p(NIPAAm)—a pH and thermosensitive polymer, has ability to change its molecular phase from hydrophilic to hydrophobic at the defined LCST [120, 121]. Owing to reversible soluble characteristics, p(NIPAAm) has been widely utilized for drug release [121], diagnostics [122], protein delivery [123], and other biomedical applications such as thermo-responsive platforms [124], particularly in a varying temperature range of 30-35 °C. By changing the temperature, phase characteristics of p(NIPAAm) can enable precisely controllable environment in terms of biomolecules isolation because the phase (from expanded to collapsed state) of the polymer changes during the temperature enhancement. Additionally, due to its thermoresponsive mechanism, p(NIPAAm)-functionalized particles exhibit a similar collapsed/expanded phase transition across the LCST, and their integration into microfluidic-based studies has been previously displayed to be an effective agent and gatekeeper for the isolation and delivery of cell, protein, drug, and CTCs/CTM [125, 123].

2.2.2 The Main Objective of the Thesis

This dissertation's aim is to fabricate an easy-to-use, efficient, and label-free platform which integrates smart materials, bio-inspired materials, and microfluidics in order to address real-world challenges in capturing and releasing/isolating biomolecules (proteins) and cancer cells as model CTC candidates. At this interdisciplinary intersection, a non-invasive strategy has been adopted through "liquid biopsy" fashion. To enhance and control the surface area in microfluidics, bio-inspired silica particles with different-shaped shell morphologies such as peanut, square, and oval were synthesized (**Figure 2.3**). Implementing shape-dependent silica particles with thermo-responsive p(NIPAAm) compounds enabled to produce 3-D structures, where surface area and so that the interactions between CTCs with the microfluidic platform were able to be controlled precisely. Even if the limited amount of sites and non-specific bindings into polymers can reduce the yields of NIPAAm integrated platforms, molar rate of initiator/monomer/ligand molecule can sustain a high number of open succinimide groups and also protein blocking can eliminate the non-specific interactions. Initially, the loading capacity of p(NIPAAm)-functionalized different-shaped silica particles was examined by binding model proteins (bovine serum albumin (BSA) and avidin-fluorescein isothiocyanate (Avidin-FITC)) noncovalently without altering their biological functionality [126]. For this purpose, the adsorption and desorption of BSA and avidin-FITC were analyzed under the conditions of room and body temperatures. Then, by harmonizing smart-polymers p(NIPAAm) with specific antibodies, it was projected to capture and release model CTCs on-a-chip due to the alterations in the different-shaped 3-D structure of smart-particles, caused by a phase transition from hydrophilic to hydrophobic at LCST. Moreover, to optimize the distance of the p(NIPAAm)-modified different-shaped silica particles, we employed distance-dependent surface linkers to attach them into the microfluidic chip, including short-length (1 nm, 3-mercaptopropyl-trimethoxysilane (3-MPS)), medium-length (7-9 nm, silane-polyethyleneglycol-thiol, 1 kDa (Silane-PEG-SH 1k)), and long-length (32-42 nm, silane-polyethyleneglycol-thiol, 5 kDa (Silane-PEG-SH 5k)) linkers. Human breast cancer (MCF-7) cells (high expression of EpCAM) were utilized as model cancer cells. Cell cytotoxicity, viability, proliferation, and specificity of the system were assessed with various standard biochemical tests such as 2,5-diphenyl-2H-tetrazolium bromide (MTT) assay analysis, live/dead assay analysis (ThermoFisher), and flow cytometry.

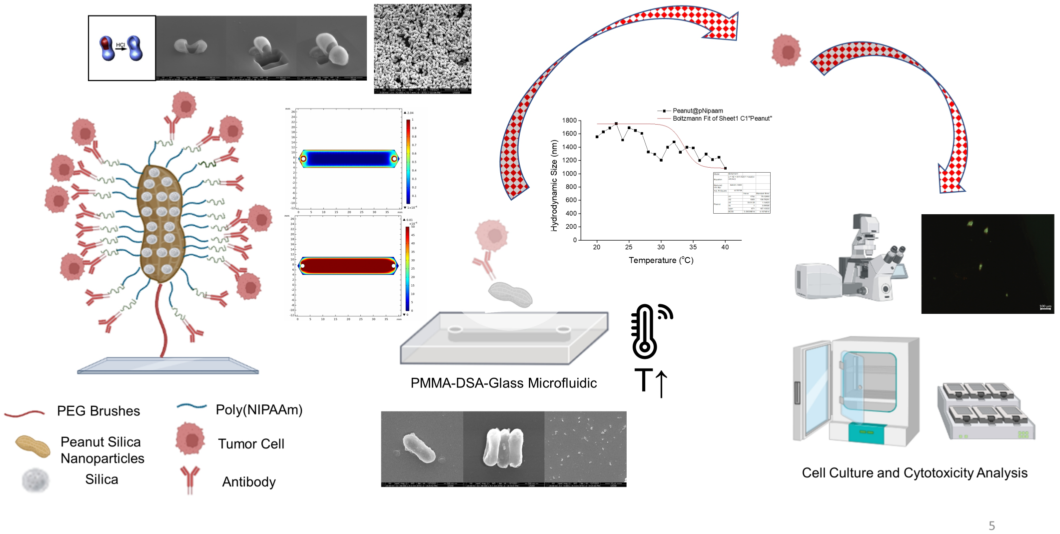

Figure 2.3: To change, enhance, and control surface area in the microfluidic chips, bio-inspired silica particles with different shapes of shell morphologies such as peanut, square, and oval are integrated to isolate CTCs by changing temperature.

Chapter 3

FABRICATION and CHARACTERIZATION of DIFFERENT-SHAPED HOLLOW SILICA PARTICLES

3.1 INTRODUCTION: The Use of Silica Particles in Biosystems

Silica particles and their assemblies have been utilized in oodles of areas including bioanalyte and chemical sensing, pharmaceutics, catalysis, and diagnostics [127, 128, 129]. During the synthesis of silica particles and their gel forms (silica-gels), physical assets such as shape, size, isotropy, polydispersity, and surface chemistry need to be controlled in order to endow looked-for chemical, optical, electronic, magnetic, and catalytic features. In particular, hollow silica particles provide controllable physical and surface characteristics such as increased pore size, specific surface area, low density, external surface functionalization, and adjustable pore diameter [115, 116]. To synthesize hollow silica particles, template-assisted strategies are expedient methods to design the final morphology of silica particles under favor of heterogonous templates that can properly control silica shape through meticulous manipulation of the hematite structure dimension. In this regard, omnipresent approaches for synthesizing silica particles are firstly tracking the steps of fabrication of hard or soft templates, and then, coating surfaces with silica gel agent on the periphery of templates [115].

3.2 MATERIALS and METHODS: Shape-Controlled Synthesis of Hollow Silica Particles

Owing to its capability to fabricate rigid, metastable, and versatile well-defined shapes (peanut, square, and oval), we here utilized hematite (α–Fe_2O_3) hard templates as a core for coating silica to synthesize (α-Fe_2O_3)@(SiO_2) core-shell colloidal structures via surfactant assemblies according to the literature [130]. The surfactant molecules neutralize the charge around silica-gel structures due to the condensation of the silica precursor and initial hydrolysis [131]. After coating the different-shaped hard templates with silica-gel, the inner core was removed through refluxing the particles in aqueous HCl solution, thus forming hollow silica particles with well-defined inner voids. The attribution of hollow feature is a pivotal phenomenon that encompasses high biomolecule loading capacity into the silica particles via highly dense and enormous porous structure. Furthermore, after eliminating the core material, the hollowness of the material enhances the flexibility which acquires surface-molecule compatibility [115]. Afterwards, in this thesis, we implemented thermoresponsive p(NIPAAm) polymers into different-shaped silica particles by surface initiated atom transfer radical polymerization (ATRP) technique, and this provided temperature controllable isolation, release, and delivery of biomolecules through the alteration of swelling/deswelling ratio of colloids.

3.2.1 Synthesis of Hematite (α–Fe_2O_3) Colloidal Hard Templates

The synthesis of different-shaped hematite (α–Fe_2O_3) particles as hard templates was carried out by the method described by Sugimoto et. al. [132, 133]. First of all, aqueous $FeCl_3$ (2 M, 100 mL) and NaOH (6 M, 90 mL) solutions were prepared. 100 mL of $FeCl_3$ solution was added to a 250 mL of Pyrex bottle, followed by slow addition of NaOH solution and the resulting mixture was stirred for 10 minutes at room temperature. To control the morphology of the particles, the amount of sodium sulfate (Na_2SO_4) solution was tuned. The agitation was hence continued by the addition of different volumes of Na_2SO_4 (0.6 M) solution to the mixture. To obtain peanut (12 mL), oval (10 mL), and square (0 ml) shaped hematite particles, different volumes and fixed concentration of Na_2SO_4 (0.6 M) solution was poured into a bottle glass and stirred for an additional 5 minutes. The tightly closed bottles were taken to a pre-heated oven at 100 °C and kept in the oven for 8 days. After 4 days, the color of the colloidal mixture turned from orange to red. After 8 days, dark red particles were precipitated into the bottom of the glass, and thus, the resulting particles were separated from the reaction mixture by pouring the supernatant (the liquid at the top). The remaining red products were washed with both deionized water (3 times and 6 min each) and ethanol (3 times and 6 min each) and separated from the mixture by centrifugation. Subsequently, the red-colored hematite particles were placed and dried in the oven at 50 °C for 24 h.

3.2.2 Synthesis of Hollow Silica Particles

Hollow silica gels with different morphologies, including peanut, square, and oval were produced via coating the sacrificial hard templates (α-Fe_2O_3) with (SiO_2) using the Stöber method. The template agent (α–Fe_2O_3) was removed from the silica-coated core/shell particles using 6M HCl (aq.) solution, thus dissolving the inner core [134]. Initially, morphologically different (α–Fe_2O_3) templates (1.5 g), non-ionic surfactant (Synperonic F108) (0.25 g), and cationic surfactant (CTAB) (0.25 g) were dispersed in a mixture consisting of 250 mL of ethanol and 12.5 mL of water through ultra sonification (4 times and 5 min each) Then, the mixture was left to stir for 30 minutes in a mechanic stirrer at 800 rpm. Afterwards, concentrated (NH_3) (2.5 mL) solution was added to the mixture, and the agitation was prolonged for 30 minutes. At the end of 1-hour mixing period, the reaction was initiated through the dropwise addition of tetraethoxysilane (TEOS) (1.25 mL) as the silica precursor, and the solution was stirred for 24 h. The products were rinsed with both deionized water (2 times and 6 min each) and ethanol (2 times and 6 min each) through the filtration method, and then, they were placed and dried in the oven preheated at 50 °C for 24 h to obtain different-shaped Fe_2O_3@SiO_2 products [135].

Thereafter, the templating agent; Fe_2O_3 was removed from the peanut, square, and oval shaped Fe_2O_3@SiO_2 (core@shell) particles through etching with HCl (6 M) solution to obtain the hollow silica gels. In this step, the Fe_2O_3 core acting as the hard template dissolves in concentrated HCl, forming Fe^{+3} and Fe^{+2} cations. Hence, Fe_2O_3@SiO_2 (1.0 g) was transferred into a single-neck glass balloon and then, HCl (6 M, 25 mL) was poured into the balloon, and refluxed at 100 °C for 24 h. The color of the solution was gradually started to turn into an orange/red color, while a white precipitate was obtained at the bottom of the balloon. The precipitate was washed with deionized water (2 times and 6 min each) and ethanol (2 times and 6 min each), and the product was then dried in a pre-heated oven at 50 °C for 24 h.

3.2.3 Synthesis of p(NIPAAm)@SiO_2 Composites

In this section of the dissertation, hollow peanut-shaped SiO_2 (0.2 g) particles were dispersed in a three-neck (100 mL) rounded bottom flask containing dry toluene (10 mL). After stirring the solution with a magnetic stir bar, aminopropyltriethoxysilane (APTES) (80 µL) was added dropwise to the mixture and refluxed for 24 h at 250 rpm at 110 °C. After modifying SiO_2 surfaces with (-NH2) APTES agent, the resulting samples were separated from the mixture by centrifugation and washed with water (2 times and 6 min. each) and EtOH (2 times and 6 min. each), and dried in a vacuum oven at 50 °C for 24 h [136]. Afterwards, the initiator agent (α-Bromoisobutyryl bromide (BIBB)) (22 µL) in toluene (200 µL) was added to the mixture containing the (-NH_2) modified hollow peanut SiO_2 (0.1 g in 5 mL) in a 100 mL of single-neck glass balloon. After that, the glass balloon was cooled to 0 °C, then, triethylamine (TEA) (33 µL) was inserted into the glass balloon, and the mixture was stirred for 30 min. Later on, the initiator agent (BIBB) was dropwise added to the glass balloon. After elevating the temperature to 25 °C, the reaction in the balloon stirred for an additional 24 h. The hollow peanut-shaped SiO_2@BIBB colloids were purified with the same method for the modification of amino groups. For the synthesis of square-shaped, and oval-shaped SiO_2@BIBB, the procedure was similar to the preparation of peanut SiO_2@BIBB.

Following this procedure, *N*-isopropylacrylamide ((NIPAAm): Acros, 97%) was polymerized via the ATRP method. NIPAAm monomer was purified by the crystallization from n-hexane at 70 °C for 2 h, and dried in the vacuum-drying chamber at 25 °C at 25 mbar prior to use. After that, dried NIPAAm (0.3 g) was dissolved in a flat-bottom flask with deionized water (5 mL). The initiator-modified peanut shaped silica gel (SiO_2@BIBB) (0.03 g) was sonicated in a round-bottom of Schlenk flask for 5 minutes. In another Schlenk hose, tris[2-(dimethylamino)ethyl]amine (Me_6TREN) (12 mg) was dissolved with water (4 mL) and degassed under an N_2 atmosphere for 10 min. Then, the dissolved NIPAAm monomer was added to the SiO_2@BIBB mixture in Schlenk flask. Subsequentially, CuBr (7.63 mg), 2-Bromoisobutanoic acid *N*-hydroxysuccinimide ester (NHS-ester) (14 mg), Me_6TREN solution, and additional water (10 mL) were added to the mixture as the catalyzer, initiator, and ligand precursor and the resulting mixture was degassed under N_2 at 4 °C for 30 minutes. NHS-ester initiator was used to end-functionalize p(NIPAAm) with succinimide group on silica gel surface for protein adsorption, whereas the BIBB initiator was engaged for controlled ATRP polymerization [137]. After that, the Schlenk flask was closed with a septum lid, and it was then stirred for 2 h at 4 °C without degassing. After polymerization, the peanut-shaped p(NIPAAm)@SiO_2 products were isolated from the solution through centrifugation with water (2 times and 6 min each) and ethanol (2 times and 6 min each), and then, the particles were placed and dried in the oven preheated at 50 °C for 24 h. For the surface-initiated polymerization of square-shaped, and oval-shaped p(NIPAAm)@SiO_2, the procedure was similar to the preparation of peanut p(NIPAAm)@SiO_2 as aforementioned (**Figure 3.1**).

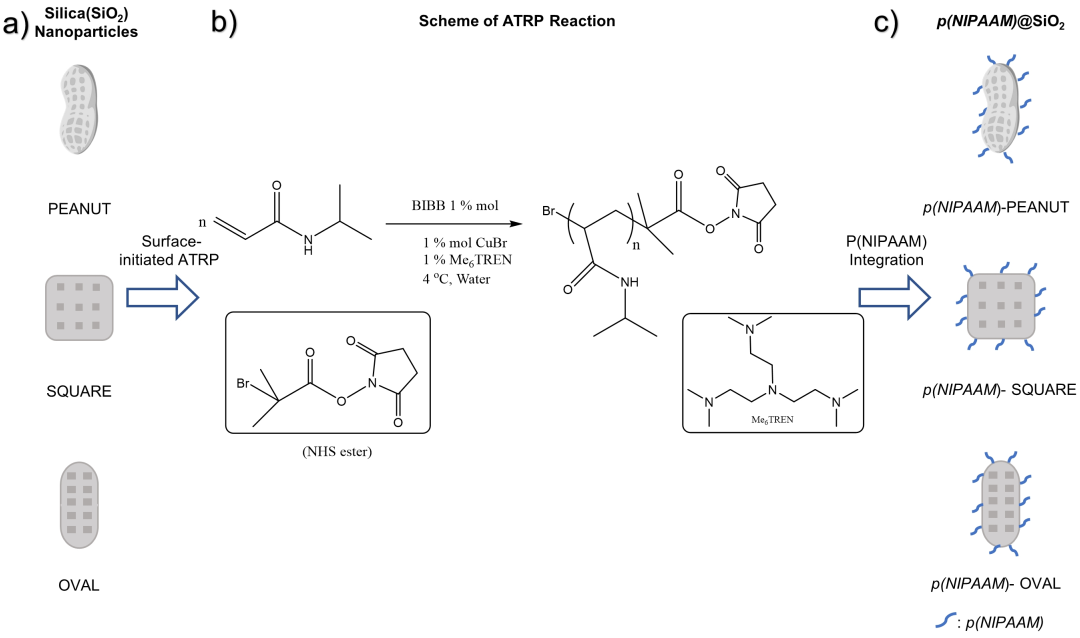

Figure 3.1: Surface initiated ATRP reaction is employed for **a)** different shapes of silica particles. **b)** The reaction scheme and **c)** p(NIPAAm)@SiO$_2$ product are illustrated.

3.2.4 Surface Modification of p(NIPAAm)@SiO_2

Once the succinimide end-functionalized p(NIPAAm) was integrated on hollow silica gels, the silica gel surface was further modified with maleimide group (-C(O)NHC(O)-) which will act as the binding site of the gel to the glass surface in further studies. The modification has two main steps: (i) peanut shape of p(NIPAAm)@SiO_2 (0.1 g) was dispersed in 50 mL of toluene in a two-necked (100 mL) rounded bottom flask. Afterwards, APTES (0.17 mmol, 40 µL) was inserted to the flask and the resulting solution was stirred at 110 °C for 12h to integrate amine (-NH_2) groups onto the silica surface. Unreacted reactants were removed by centrifugation of the resulting mixture and the resulting solid was washed using toluene (2 times and 6 min each) and ethanol (2 times and 6 min each) to purify the silica gel. (ii) Peanut shaped p(NIPAAm)@SiO_2-NH_2 (0.1 g) was mixed with maleic anhydride (25 mg) and toluene (50 mL) in a two-neck (100 mL) rounded bottom flask at 140 °C for 12 h. The condensation reactions between amine and anhydride groups formed maleimide groups on the surface of silica particles. Finally, peanut-shaped and maleimide-integrated p(NIPAAm)@SiO_2 was purified with the same method for the modification of amino groups. For the maleimide and p(NIPAAm) functionalized square-shaped, and oval-shaped SiO_2 particles were prepared using the same procedure that for peanut-shaped particles (**Figure 3.2**).

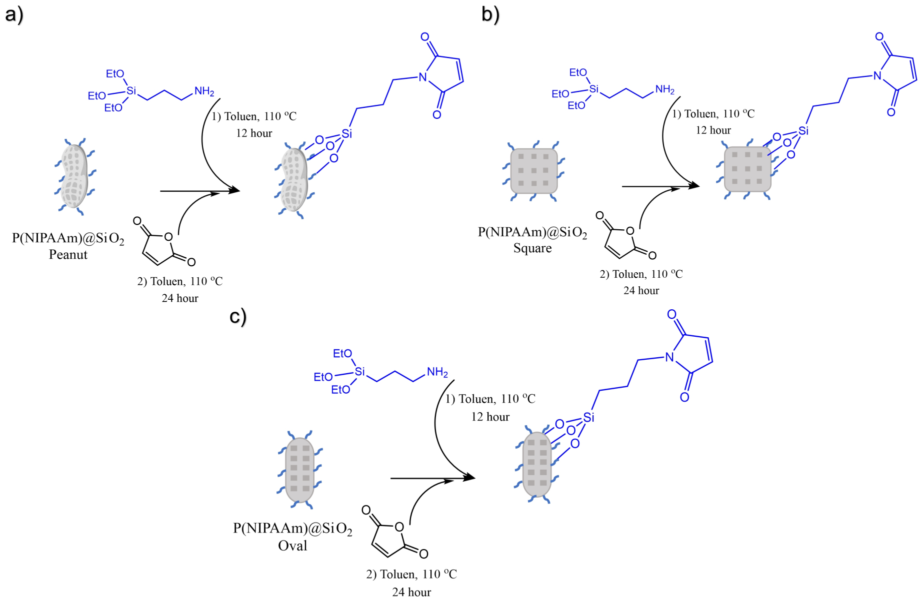

Figure 3.2: Surface modification is presented on **a)** peanut, **b)** square, and **c)** oval shapes of p(NIPAAm)@SiO_2 particles.

3.3 RESULTS and DISCUSSION

3.3.1 Characterization of Fe_2O_3, Hard Templates Fe_2O_3@SiO_2 Silica Gel Coated Templates, and SiO_2 Hollow Silica Particles

Morphology, elemental content, and 2D structure of synthesized peanut, square, and oval -shaped Fe_2O_3, Fe_2O_3@SiO_2, and hollow SiO_2 particles were examined by scanning electron microscopy (SEM), energy dispersive X-ray spectroscopy (EDX), Fourier transform infrared spectroscopy (FTIR) and transmission electron microscopy (TEM). The initial Fe_2O_3 templates were found to be monodisperse in size distribution and the sizes of the particles were found to be 1.30-1.50 µm, 0.35-0.45 µm, and 0.7-0.9 µm for peanut-, square-, and oval-shaped particles as confirmed by SE analysis respectively. The coating of hematite Fe_2O_3 particles was carried out through the formation of silicic acid and silicate derivatives from the precursor molecule; TEOS, which could be polymerized in a basic medium (pH>7). The -OH groups on the template surface react with the silica agent, and it can form silanol groups (Si-OH) that further produce siloxane bonds (Si-O-Si) leading to the formation of Fe_2O_3@SiO_2 core /shell structure. In our study, the removal of the sacrificial core was performed in the presence of HCl to prepare the hollow SiO_2 shells with different morphologies. The thickness of peanut-, square-, and oval-shaped SiO_2 shells were measured from the SEM images using ImageJ software. The shell-thickness of the hollow silica gels was found to be between 35-75 nm range.

When the EDX spectrums were examined with SEM images, Fe (0.709 (Lα) ve 6.398 (Kα) keV) and O (0.530 (Kα) keV) content was obvious for different shapes of Fe_2O_3 hard-templates (**Figure 3.3a-c**). In addition to Fe and O, a strong peak at Si (1.74 (Kα) keV) proved that the silica-gel coating was completed successfully for the Fe_2O_3@SiO_2 core/shell structure (**Figure 3.3d-f**). After etching the template with HCl solution, the iron (III) oxide core was removed from the silica gel, whereas the Si peak appeared once again (**Figure 3.3g-i**). In addition, the contrast difference between the outer shell and inner hollow sections of the particles was visualized on TEM (**Figure 3.4**).

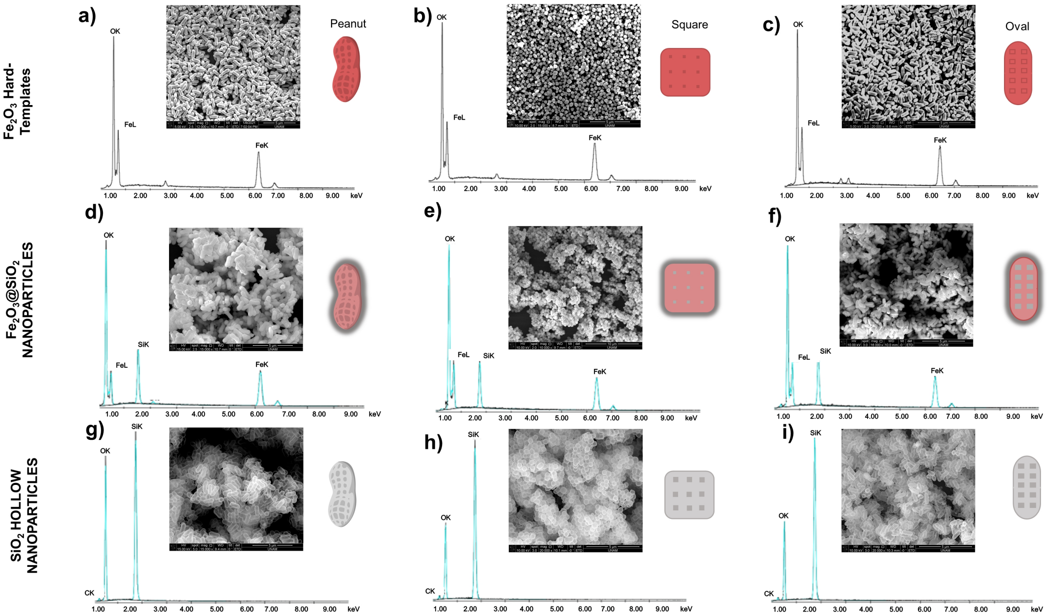

Figure 3.3: SEM-EDX analyses of peanut, square, and oval shapes of particles are presented. **a-c)** Fe_2O_3 hard template, **d-f)** $Fe_2O_3@SiO_2$ core/shell, and **g-i)** SiO_2 hollow particles.

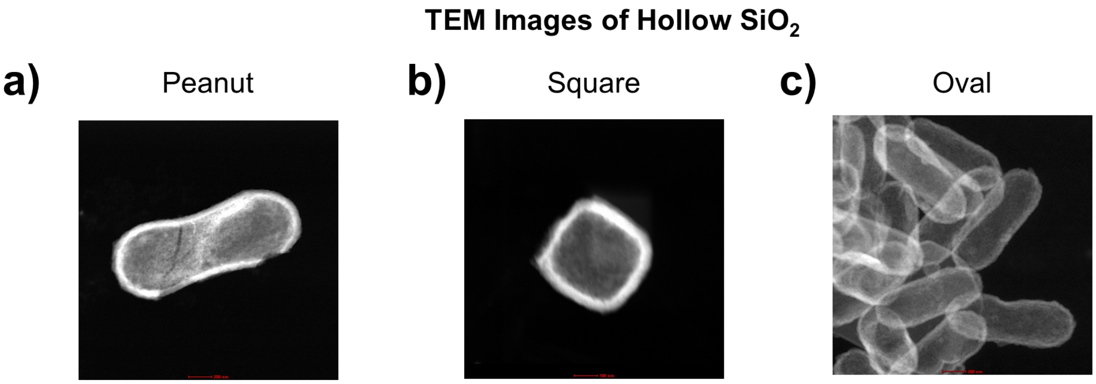

Figure 3.4: TEM images present hollow versions of **a)** peanut, **b)** square, and **c)** oval shaped SiO_2 particles.

Moreover, the crystal diffraction pattern of Fe_2O_3 and SiO_2 particles were characterized by X-ray diffractometry (XRD) (**Figure 3.5**). Hematite Fe_2O_3 hard-template exhibited a similar peak distribution to the (04-003-1145) reference coded Fe_2O_3 rhombohedral single-crystal, confirming that the hematite particles were synthesized successfully [138]. The XRD pattern of hollow SiO_2 shells did not show any regular crystal structure, whereas it had an amorphous structure, in particular, the wide peak between 10-35 ° proved the presence of an amorphous structure [139]. When the XRD patterns of hollow SiO_2 shells were indexed to the (04-008-7833) reference coded SiO_2 phase, the existence of silica material was realized clearly

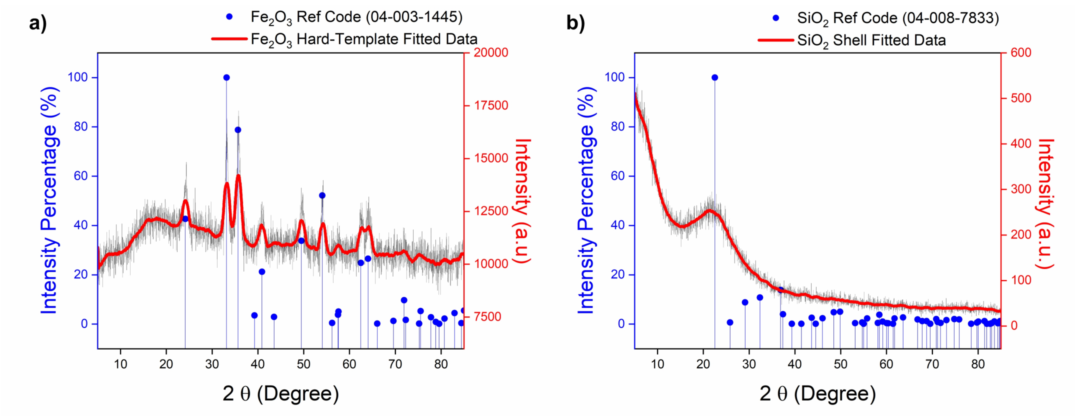

Figure 3.5: XRD patterns are presented for **a)** Fe_2O_3 and **b)** SiO_2 particles.

In addition, FTIR spectrums of the $Fe_2O_3@SiO_2$ and SiO_2 particles were examined in the span of 400-4000 cm^{-1} as depicted in (**Figure 3.6**). The common stretchings and bending vibrations were observed at 3448 and 3469 cm^{-1} (–NH) stemmed from H-bond vibrations, 1150 and 1102 cm^{-1} / 751 and 802 cm^{-1} stand for doublet (SiO_2) peaks, whereas 2996 cm^{-1} (Si–OH), 2952 cm^{-1} (–CH_2), and 2843 cm^{-1} (–CH) originated from aliphatic groups were observed in $Fe_2O_3@SiO_2$ particles.

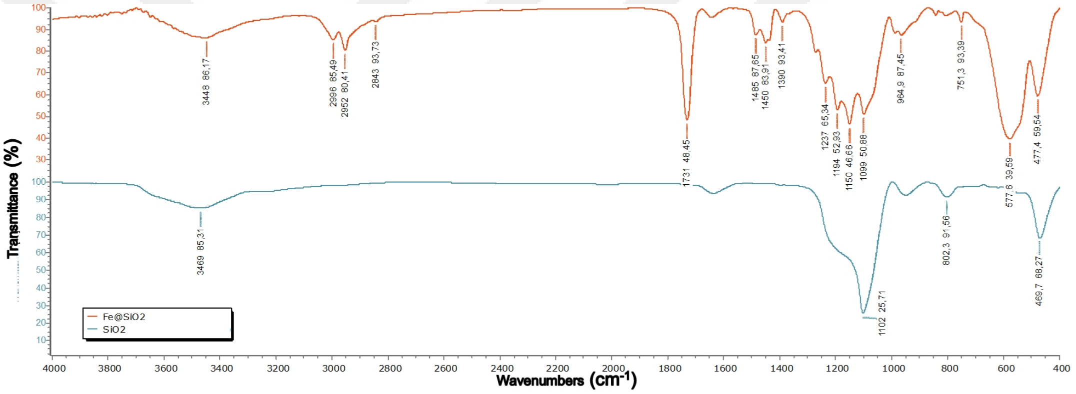

Figure 3.6: FTIR analysis is presented for **a)** Fe_2O_3 and **b)** SiO_2 particles

3.3.2 Characterization of p(NIPAAm)@SiO$_2$ Composites

Some of the p(NIPAAm)@SiO$_2$ composites were initially filtrated to extract NIPAAm polymer (**Figure 3.7**) for the characterization studies in ^{1}H and ^{13}C Nuclear Magnetic Resonance (NMR), FTIR, Size Exclusion Chromatography (SEC), and lastly, Differential Scanning Calorimetry (DSC). ^{1}H NMR spectrum of the p(NIPAAm) was performed in CDCl$_3$ with a 400 MHz FT-NMR spectrometer.

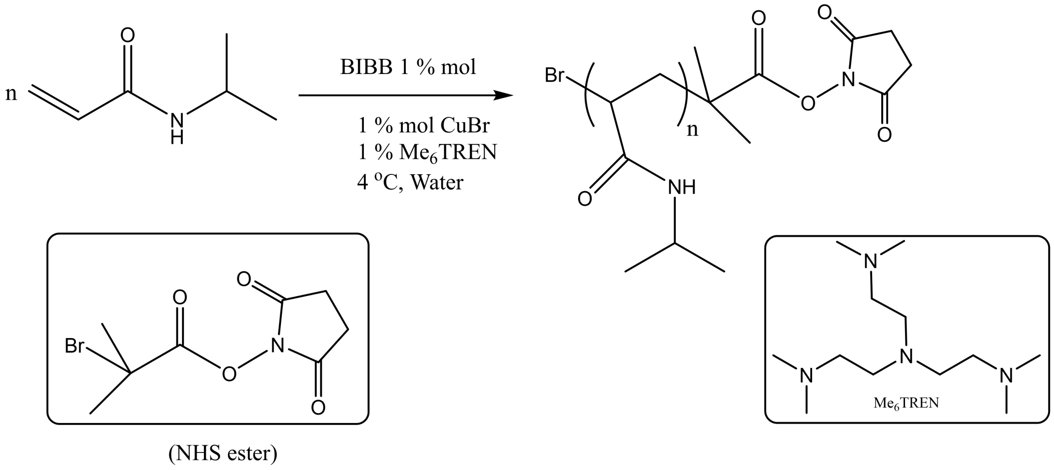

Figure 3.7: Polymerization of NIPAAm monomer is illustrated.

For the ^{1}H NMR, the existence of a broad signal in the range of 6.5-5.7 ppm (g) belonged to the proton in –NH- groups with a low intensity due to hydrogen bonds in the structure (**Figure 3.8**). The multiple peaks observed at the value of 4.02 ppm (a) were related to –CH- proton in NH-CH- group. CH-CH- protons in linear chain structure repeating in p(NIPAAm) structure were observed as wide peak sets within the range of 2.29-0.84 ppm (b and c+d). The –CH group adjacent to the electron-withdrawing amide group peaked in the region of 2.29-1.90 ppm, while the neighboring –CH group was observed at 1.67 ppm (c+d). The –CH_3 protons in the isopropyl group were perceived in the 0.84 ppm region (b). The -CH_2-CH_2- protons in the succinimide group attached to the end of the chain were observed as a small signal of 2.54 ppm (f). Since the N-succinimide group was at the end of the chain, the corresponding peak was relatively low, and therefore, it resulted in weak signals.

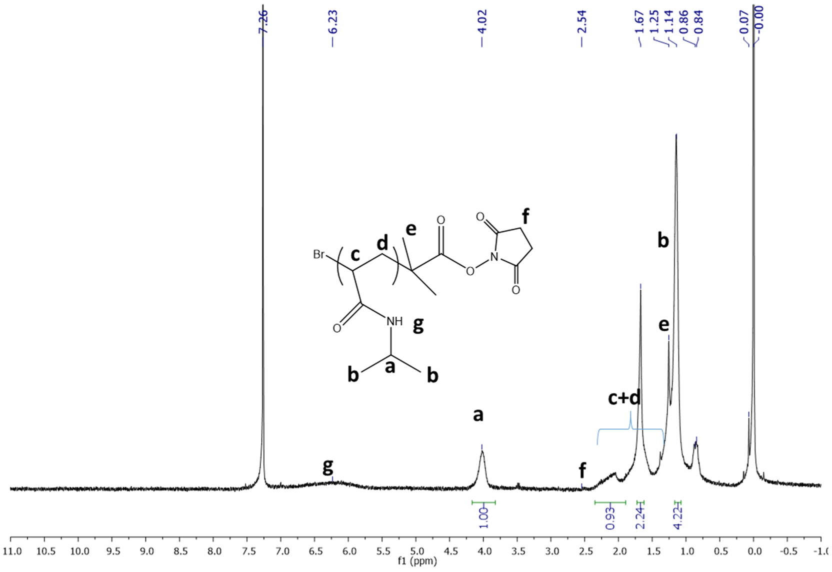

Figure 3.8: ^{1}H NMR spectrum of p(NIPAAm) is represented.

For the ^{13}C NMR studies, the existence of a signal in the 174.40 ppm (a) was related to the carbonyl group (-C=O-) (**Figure 3.9**). Since the N-succinimide group is located at one end of the chain, we observed this corresponding signal quite low at 164.50 ppm (b). The multiple peaks in the range of 120-140 ppm were not observed since all of the monomeric NIPAAm molecules were converted to polymers. At the value of 42.19 ppm, (c) belongs to the –CH- proton in the NH-CH- group, whereas (e) at 22.62 ppm is (-CH_3), and around 0.00 ppm belongs to tetramethylsilane (TMS) solvent.

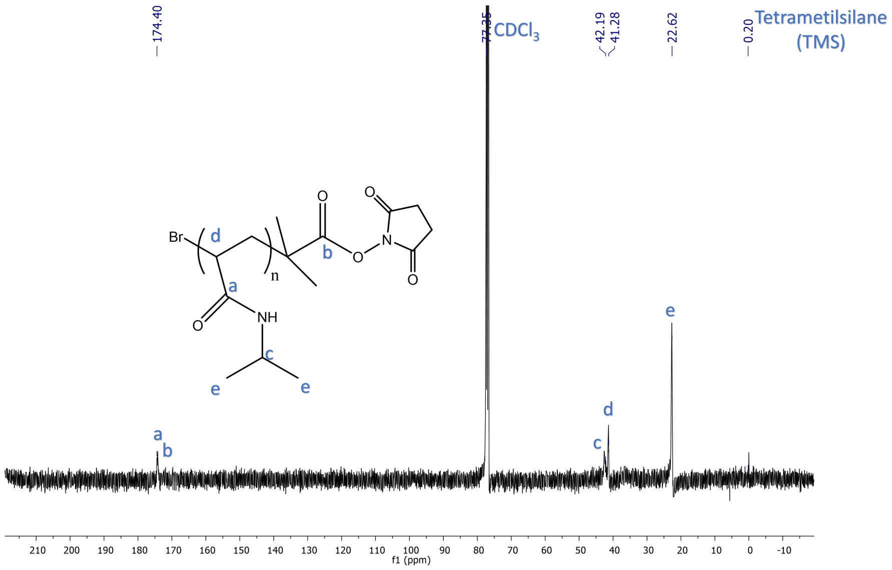

Figure 3.9: ^{13}C NMR spectrum of p(NIPAAm) is demonstrated.

In addition, common stretchings and bending vibrations arising from H-bond vibrations were observed at 3550 and 3288 cm^{-1} (–NH) in FTIR analysis of p(NIPAAm) functionalized peanut-shaped silica gel (**Figure 3.10**), 3074 cm^{-1} (–CH$_2$), 2975 cm^{-1} (–CH) originated from the presence of aliphatic groups, whereas the peaks appearing at2139 cm^{-1} (-CN), 1653 cm^{-1} (-C=O-) was associated with the presence of carbonyl group, 1750-1760 cm^{-1} (-C=O-) of succinimide ring. The peak appearing at1653 cm^{-1} was associated with the presence of the amide group (-C=O-N-H).

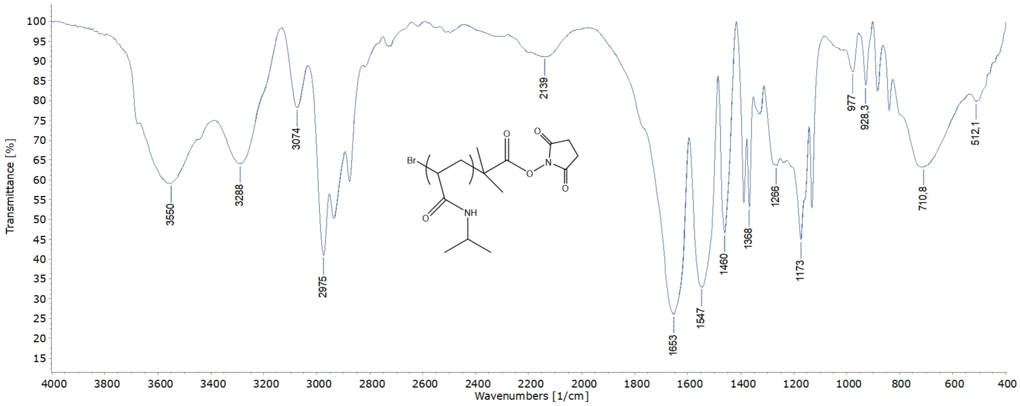

Figure 3.10: ^{13}C NMR spectrum of p(NIPAAm) is demonstrated.

Next, the number average molecular weight (M_n) of p(NIPAAm) was varied using different amounts of initiators and monomers **Table 3.1**. For this process, the ratio of BIBB/NHS-ester (mol/mol) was tested as 1/3, 1/2, and 1/1, and there was no significant change was observed in the molecular weight (M_n) and yield percentage. The M_n values were measured as 10, 12, and 13 kDa for 100/1/1/3, 100/1/1/2, and 100/1/1/1 (NIPAAM/catalyst/initiator/initiator; mol/mol/mol/mol), respectively. The polydispersity index values (PDI) of polymers were found to be 1.1 which indicates that the ATRP polymerization was proceeded in a controlled manner. When the amount of monomer was doubled, the molecular weight (M_n) of the polymer was increased to 28 kDa. Therefore 100/1/1/3 ratios (NIPAAM/Cu(I)Br/ BIBB/ NHS-ester) was chosen as the polymerization parameters due to the high yield. The SEC traces of the resulting polymer was also given in **Figure 3.11**.

Table 3.1: Molecular weight change of the p(NIPAAm) in the existence of the versatile amounts of initiators and monomers is evaluated through PDI and the yield analysis.

Experiment	NIPAAm/Cu(I)Br/BIBB/ NHS-ester (mol/mol/mol/mol)	Me$_6$TREN (mol %)	Time (min)	M$_n$	PDI (M$_w$/M$_n$)	Yield %
1	100/1/1/3	1	12	10 kDa	1.1	90
2	100/1/1/2	1	12	12 kDa	1.1	90
3	100/1/1/1	1	12	13 kDa	1.1	85
4	100/1/1/1	1	12	28 kDa	1.1	78

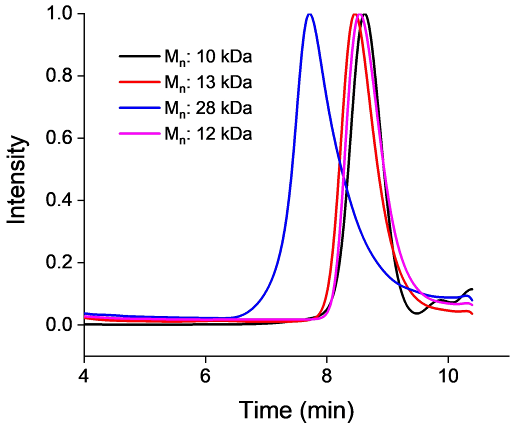

Figure 3.11: SEC traces of p(NIPAAm) for the molecular weight vs retention time analysis.

The DSC thermogram of p(NIPAAm) compound (Mn: 10 kDa), the endothermic peak at 35.4 °C corresponded to the LCST of the polymer (**Figure 3.12**). At the above this temperature, H-bond activity in the p(NIPAAm) diminished, and the functional amide group lost its hydrophilic effect and became hydrophobic [**?**]. In addition, the second endothermic peak which was observed at 61.8 °C associated to the hydration of amide groups in the structure. The glass transition point (T_g) of the polymer was observed at 134.4 °C [140]. Furthermore, the color changed in p(NIPAAm) molecule as it turned from hydrophilic to hydrophobic phase depending on the temperature.

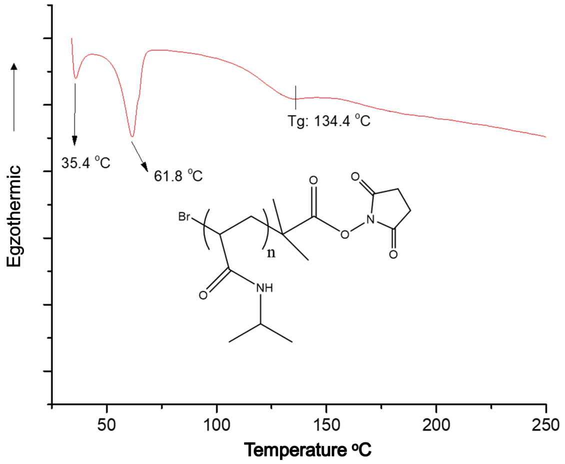

Figure 3.12: DSC thermogram of the p(NIPAAm) compound (M_n: 10 kDa) is presented.

After the surface-initiated ATRP modification of peanut, square, and oval shaped silica gels, the surfaces of p(NIPAAm)@SiO_2 composites were characterized by XPS (**Figure 3.13**). For each p(NIPAAm)@SiO_2 composites, the characteristics peaks of silicon (Si2p) were observed at 103 eV and 154 eV (Si2s), carbon (C1s) at 285 eV, nitrogen at 400 (N1s) eV, oxygen at 532 eV (O1s), respectively [136]. To present specific bonds of composites, we further examined C1s spectra of different shapes of p(NIPAAm)@SiO_2, and four distinct peaks associated with C-H, C-C=O, C-N, and N-C=O were detected with varying binding energies.

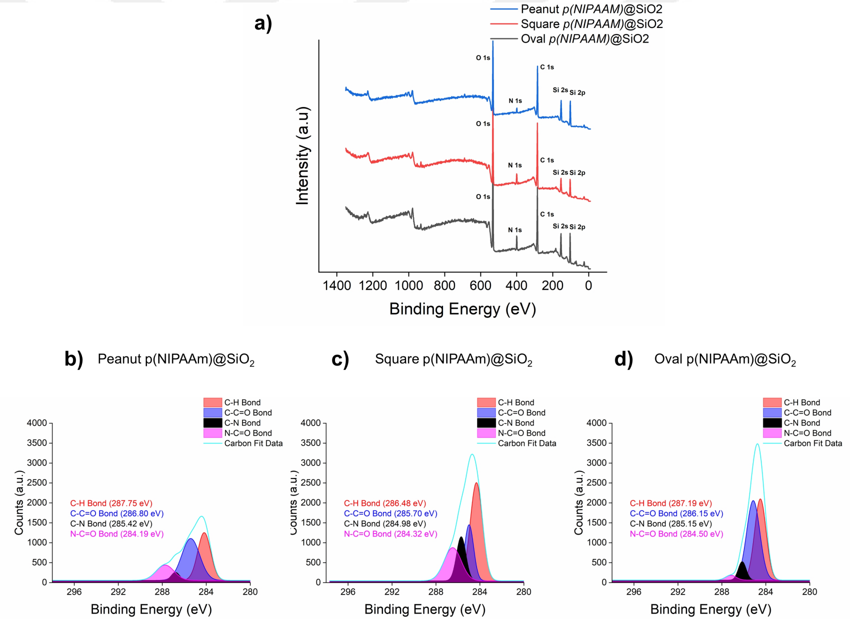

Figure 3.13: XPS analysis for different shapes of p(NIPAAm)@SiO_2 particles is presented. **a)** General survey and C bondings of **b)** peanut, **c)** square, and **d)** oval shapes of particles are demonstrated.

Furthermore, the existence of p(NIPAAm) on the silica gel surface was proved by SEC investigation. The p(NIPAAm) was integrated on the silica gel surface through covalent bonds during ATRP reactions. Therefore, the direct analysis of p(NIPAAm)@SiO_2 is not possible due to the solubility and dispersion issues. Therefore, p(NIPAAm) was detached from the silica surface prior to size exclusion chromatography (SEC) analysis. For this purpose, the p(NIPAAm)@SiO_2 particles (0.050 g) were dispersed in THF/MeOH (4 mL/0.10 mL) after that 50 µL concentrated H_2SO_4 was added to disintegrate the p(NIPAAm) from silica surface through transesterification reactions. as depicted in **Figure 3.14**, SEC analysis of the synthesized polymers extracted from different shaped SiO_2 was performed to measure molecular weight distribution. Relatively higher M_n values were observed for peanut and oval-shaped silica gels whereas slightly lower M_n value was observed in SEC analysis (**Figure 3.12**).

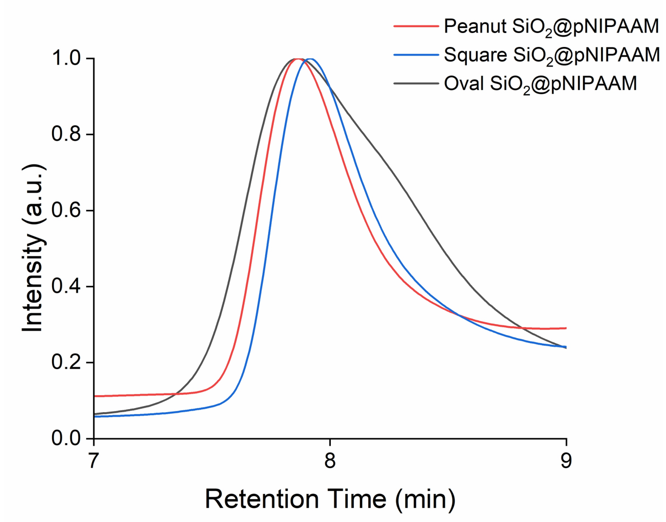

Figure 3.14: SEC traces of different-shaped p(NIPAAm)@SiO_2 is presented.

To harmonize the data from XPS and SEC analyses, thermogravimetric analysis (TGA) of p(NIPAAm) (113.16 g/mol), p(NIPAAm)@SiO_2, and SiO_2 particles were compared in **Figure 3.15**. All three samples revealed a weight loss of 3.0% at <100 °C and 6% at <317 °C because of the desorption of water molecules in the porous structure of specimens. From 317 °C to 450 °C, p(NIPAAm) degraded to almost 9.0%, and the values for weight retention were observed 94.5%, 73.5%, and 6.1% for SiO_2, p(NIPAAm)@SiO_2, and p(NIPAAm), respectively. This confirmed the attachment of p(NIPAAm) onto the surface of silica particles.

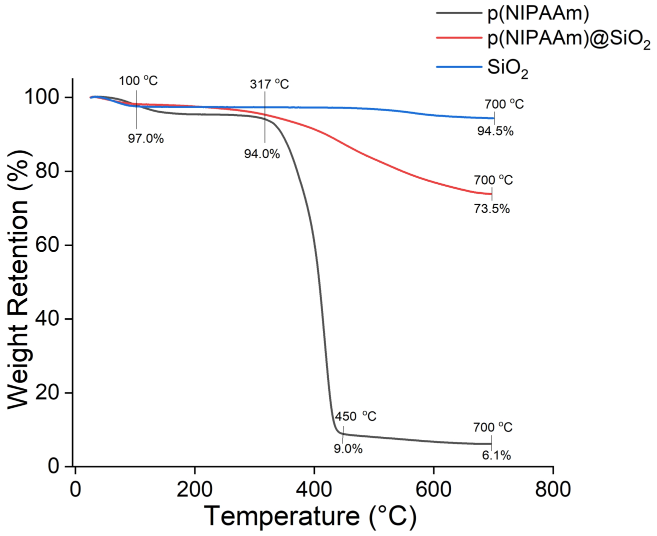

Figure 3.15: TGA analysis of p(NIPAAm), p(NIPAAm)@SiO_2, and SiO_2 is demonstrated.

3.3.3 Temperature-Dependent Size Characterizations of Different-Shaped Particles

The phase of p(NIPAAm) shifts from hydrophilic to hydrophobic due to the coil-to-globule transition of the material occurring at LCST, as the temperature increases from room temperature (25 °C) to body temperature (37 °C). The cloud points (CP) analysis of thermo-sensitive polymers are widely used to investigate the turbidity of polymers, thereby understanding the exact LCST values [141]. We also snapshotted the temperature-dependent turbidity alterations of the p(NIPAAm), and as depicted in **Figure 3.16**, the polymeric aqueous solution started to turn cloudy at 32 °C.

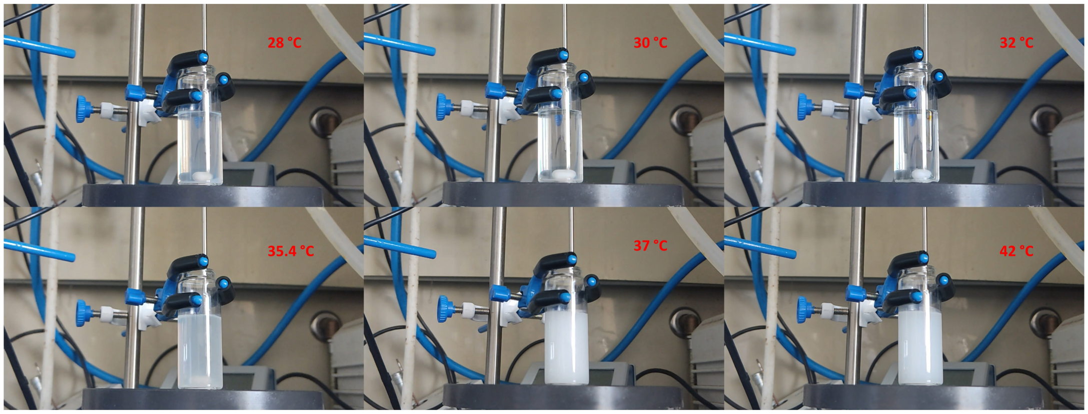

Figure 3.16: Temperature-dependent turbidity (cloud points) alterations of the p(NIPAAm) are presented.

Throughout the phase transition, peanut, square, and oval shaped p(NIPAAm)@SiO$_2$ particles exhibited reversible swelling and shrinking characteristics upon temperature change. As the temperature of aqueous solutions containing different shaped p(NIPAAm)@SiO$_2$ compounds increases, the swelling ratio and the hydrodynamic (HD) particle size will be decreased (especially after LCST temperature) [112, 142]. To examine the HD size of the different shapes of p(NIPAAm)@SiO$_2$ particles, the method of dynamic light scattering (DLS, Zetasizer Nano ZS (Malvern Panalytical, UK)) was used by setting the following parameters as 1.45 of refractive index for p(NIPAAm) [143]; 0.3 a.u. of absorbance at 272 nm (**Figure 3.17**) [112, 142]. The average HD size of peanut, square, and oval shapes of p(NIPAAm)@SiO$_2$ was measured at 25 °C, and they were 1691 nm, 880 nm, and 1014 nm, respectively. These values decreased to 1296 nm, 551 nm, and 785 nm while changing the temperature to 37 °C. Especially above the LCST point, the formation of strong p(NIPAAm) segment aggregations could be observed due to hydrophobic interactions between the isopropyl groups of p(NIPAAm) side chains [144]. However, above the LCST of composites, no significant aggregative associations were realized since p(NIPAAm) chains grafted on the surface of silica particles denoted steric stability to the suspension.

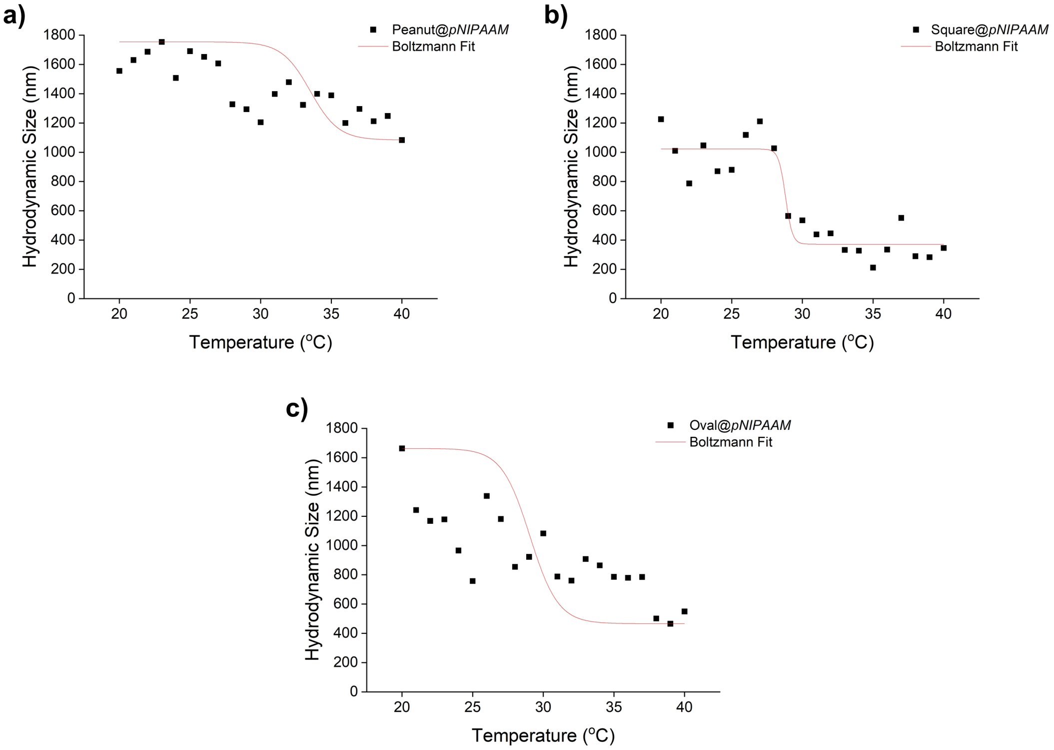

Figure 3.17: Temperature-dependent hydrodynamic size analysis is performed for **a)** peanut, **b)** square, and **c)** oval shapes of p(NIPAAm)@SiO_2 particles.

Furthermore, the polymer chain length, the concentration of polymer solution or polymer molecular weight also affect LCST value. Gupta et al. showed the LCST point fractions of p(NIPAAm) moieties according to the size of the core structure [145]. As the size of the core structures enhances, their surface area increases. They have observed that core structures act like anchors and control polymer rotation, movement, and conformational change points. The larger particles having more surface area restrict to form of hydrophobic globule because the amount of energy increases to overcome this restriction [145]. As the energy quantity enhances, the LCST will go further high. Hence, the surface area of peanut-, square-, and oval-shaped SiO_2 composites will be the dominant factor in designating LCST points.

The surface areas of different-shaped SiO_2 particles were calculated by Brunauer–Emmett–Teller (BET) via N_2 adsorption/desorption isotherm analysis (**Figure 3.18**). The related isotherm graph (Type IV) applies only to mesoporous solids, which absorb the gas at the range of 0.6-0.95 P/P_0 (hysteresis loop). Furthermore, the belly-like region between 0.65-0.90 P/P_0 between the adsorption and desorption curve confirms the presence of hollow-void within the silica gel structure. From the isotherm graphs, the specific surface areas of peanut-, square-, and oval-shaped SiO_2 particles were measured as 506.983, 94.228, and 236.716 m^2/g, respectively (**Table 3.2**). On the parallel track, the LCST of peanut-, square-, and oval-shaped p(NIPAAm)@SiO_2 were found around 37 °C, 30 °C, and 35 °C from DLS analysis.

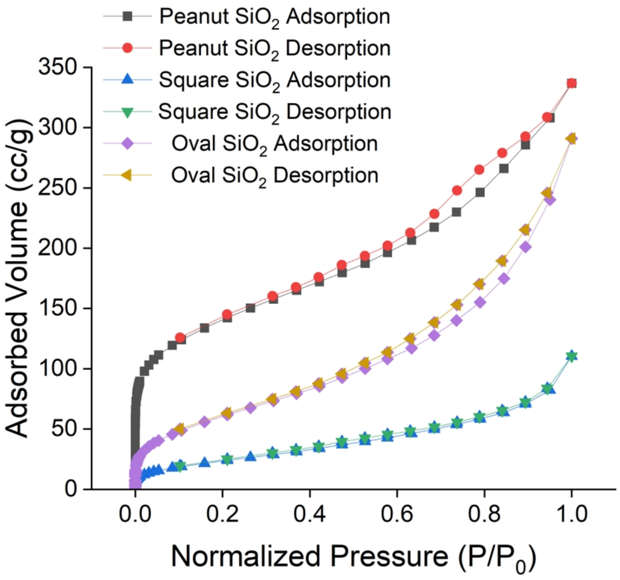

Figure 3.18: BET, N_2 adsorption/desorption isotherm analysis is presented for different-shaped SiO_2.

Table 3.2: Area of surface, the radius of pore, and volume of pore analysis are depicted for different shapes of SiO_2 particles.

	Peanut	Square	Oval
Surface Area (m^2/g) (Full Isotherm)	506.983	94.228	236.716
Pore Radius (A°) (BJH Method)	15.297	17.048	17.018
Pore Volume (cc/g) (BJH Method)	0.073	0.022	0.070

3.3.4 Characterizations of Surface Modifications into p(NIPAAm)@SiO$_2$ Particles

Following p(NIPAAm) integration, the maleimide modification into peanut, square, and oval shapes of p(NIPAAm)@SiO$_2$ was performed to form thioether linkages between maleimide groups and sulfhydryl groups (from 3-MPS enriched glass slides). Herein, p(NIPAAm)@SiO$_2$ were initially characterized by ATR-FTIR analysis (**Figure 3.19**). The common stretchings and bending vibrations for each analyses were observed at 3650 cm^{-1} (-NH), 2980 cm^{-1} (C-H), 1650 cm^{-1} and 1540 cm^{-1} (C=O), 1385 cm^{-1} (C-O), 1235 cm^{-1} (C-C), 1150 cm^{-1} (=C-H), 1060 cm^{-1} and 800 cm^{-1} (Si-O-Si), and 950 cm^{-1} (Si-C) of wavenumbers. After maleimide integration, the shifted C=O and C=C stretching at 1700 cm^{-1} and 1460 cm^{-1} indicated the presence of carbonyl groups and maleimide rings in the modified p(NIPAAm)@SiO$_2$.

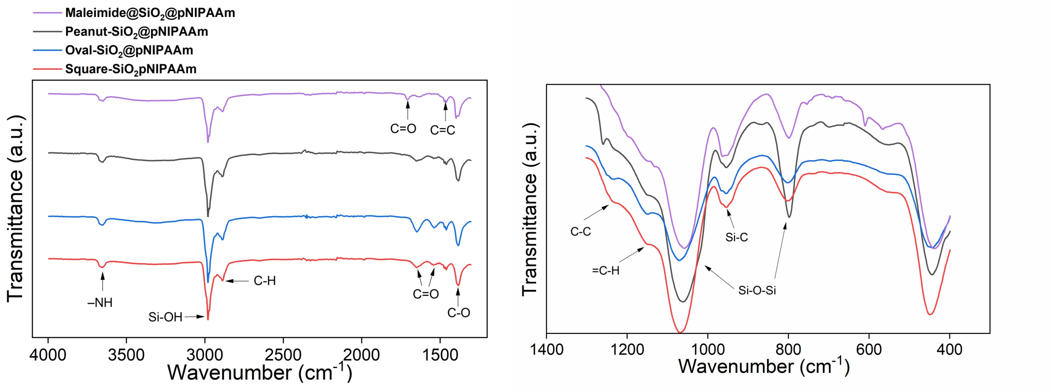

Figure 3.19: FTIR analysis is employed for maleimide modification into peanut, square, and oval shapes of p(NIPAAm)@SiO$_2$ particles.

3.4 CONCLUSION

In this chapter, we synthesized peanut, square, and oval hollow silica particles, and then, p(NIPAAm) brushes were integrated to their surfaces via ATRP method. Finally, the surface modifications with succinimide and maleimide groups were applied to the outer shells of p(NIPAAm)@SiO_2 colloids.

In the first stage, hematite (α-Fe_2O_3) hard templates with peanut, square, and oval morphologies were fabricated. Subsequently, different shapes of hard templates were homogeneously coated with silica-gel without any agglomeration. The Fe_2O_3@SiO_2 core-shell structures were treated with HCl acid solution to remove the core structure, hence forming different shapes of hollow silica-gel structures. All these steps were characterized. Briefly, morphology was analyzed by TEM and SEM; the chemical composition was studied with SEM-EDX, and FTIR; and crystal structure was evaluated with XRD. Second, the synthesis of p(NIPAAm) by the surface-initiated ATRP method and its integrations into peanut, square, and oval shapes of SiO_2 colloids were carried out. The p(NIPAAm)@SiO_2 compounds were characterized by FTIR, ^{1}H-^{13}C NMR, DSC, SEC, XPS, and TGA. By detecting two endothermic peaks of p(NIPAAm)@SiO_2, the glass transition (Tg) points of each compound were evaluated. Furthermore, the temperature-dependent size analysis and surface area measurements were analyzed via DLS and BET methods, respectively. Finally, maleimide groups were modified via amination with APTES, and then, maleic anhydride was şntegrated. On the other hand, succinimide groups were modified with ATRP initiator agent (BIBB) into the surface of p(NIPAAm)@SiO_2 colloids. The presence of functional groups was determined by FTIR and XPS analyses.

Chapter 4

NUMERICAL MODELING and FABRICATION of MICROFLUIDICS

4.1 INTRODUCTION: Significance of Microfluidics for the Isolation of CTCs/CTM

Microfluidic devices are currently in use for CTCs isolation, and however, there are significant challenges including low cell recovery, purity, and enrichment rate [47, 48]. Furthermore, enriching CTM is a more challenging process than the technique of capturing single circulating cancer cells due to its limited lifespan and rarity. At that point, microfluidics offers an opportunity to work with minute sample volumes, parallelization, and low-cost; yet the hydrodynamics of a fluid flow needs to be well-arranged to isolate CTCs on-a-chip [146, 147]. In this chapter of the dissertation, we have denoted some of the numerical modeling and simulations to find the optimum flow conditions before designing and fabricating a microfluidic chip, which would be integrated with smart materials in the next chapters.

4.2 MATERIALS and METHODS: Numeric Flow Simulations and Chip Fabrication

The microfluidic chips could potentially be hindered by the entailment of hydrostatic pressure-related damages since the components locating the inner-surface of the chip are subjected to shear stress [148]. Investigating such shear stress-stemmed effects is merely enough in a microenvironment since volumetric inertial and gravitational forces are insignificant in the microenvironment, enabling the shear stress to become the leading force in the channel [149]. By effectively altering the flow rates of fluid, a uniform velocity gradient and shear stress would be achieved via designing the chip parameters with a low-aspect-ratio [150]. Furthermore, the topographic and biomechanical properties of elements on the chip surface would also have an impact on the shear stress distribution; yet the device geometry and aspect-ratio are the foremost factors to control it. Elaborating with an example from the literature, a range of 30-350 µL/min of flow rate was applied to "T" channel microfluidic chip with a 3/13 aspect ratio (width/length). While applying 30 µL min^{-1} and 80 µL min^{-1} of flow rates, the shear stress values were observed as 20.4 dyne cm^{-2} and 54.3 dyne cm^{-2}, respectively. The highest protein attachment to the surface was seen below 100 µL min^{-1} [151]. Considering another type of strategy, a pH-responsive platform was constructed in a microfluidic chip, which had crisscrossed multiwall carbon nanotubes. This platform was employed to capture (almost 80% of capture and release efficiency) and then, allowed to release CTCs [152]. In another study, Neoh et. al. employed 1007 kg m^{-3} (10 µL min^{-1}) as an optimal flow rate value to test the capture and release efficiency of the herringbone (HB)-based microfluidic platform [152].

4.2.1 Mathematical Modelling and Designing of Microfluidic

To envisage any effects of fluid flow velocity and shear stress on cell isolation kinetics, we simulated the microfluidic chip parameters (especially the microchannel portion) using COMSOL Multiphysics® 5.6. software. In this manner, by considering the flow rate (5, 10, 20, 50, and 100 µL min^{-1}), channel height (25, 50, and 100 µm), and analysis time, we have solved the Navier-Stokes equations **(Equation 4.1)** to find out the most convenient profiles.

$$\frac{\delta u}{\delta t} + (u\bigtriangledown)u - \frac{\gamma}{\rho}(\bigtriangledown)^2 u = -\frac{1}{\rho}(\bigtriangledown)(\rho) + g \tag{4.1}$$

Where u, t, γ, ρ, and g are the velocity, time, dynamic viscosity, density of the fluid, and gravitational force. As shear forces are more predominant than the gravitational force, and due to incompressible flow characteristics, velocity gradient and gravitation can be neglected **(Equation 4.2)**.

$$\frac{\delta u}{\delta t} - \frac{\gamma}{\rho}(\bigtriangledown)^2 u = -\frac{1}{\rho}(\bigtriangledown)(\rho) \tag{4.2}$$

4.2.2 The Fabrication of Microfluidic Chip

Microfluidic chip design consists of three main parts: (i) upper-layer, polymethyl methacrylate (PMMA, 2 mm thickness), (ii) double sided adhesive layer (DSA, 50 μm thickness), and (iii) glass slide (24 mm x 60 mm) (**Figure 4.1**). PMMA layer includes an inlet and an outlet, where specimens are introduced and retracted via the tubings. DSA layer is placed between PMMA layer and glass slide to enable a proper height of the channel. Before assembling them all, glass slides and PMMA were sonicated inside ethanol for 15 min, following the wash step with water and drying step with the compressed air. The CAD software (RDWorks) was used to design the PMMA and DSA layers, and accordingly, they were cut operating a laser cutter-operated with a CO_2 laser (LazerFix, Turkey) [153, 74, 154]. Additionally, semi-transparent, chemically inert, and non-toxic polytetrafluoroethylene (PTFE) tubings (15 cm) (ColePalmer (Vernon Hills, IL, United States)) were glued with epoxy resin onto the inlet and outlet ports of the PMMA layer.

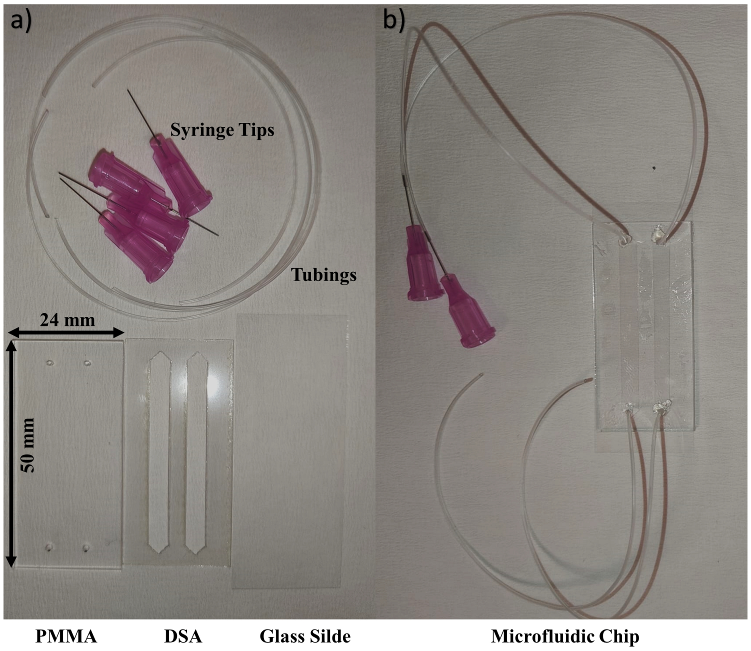

Figure 4.1: Microfluidic chip design consists of **a)** PMMA, DSA, glass slide, syringe tips, and tubings. **b)** The microfluidic chip and its components are shown after assembling parts of the chip.

4.2.3 Evaluating The Flow and Binding Properties of Fabricated Microfluidic Chip

After fabricating the microfluidic chip, the microfluidic channels were decorated with biotin protein. Before assembling the parts of the chip, glass slides were sonicated for 15 minutes in ethanol and dried with the compressed air. After that, the slides were treated with oxygen plasma (100 W, 2 min) to increase reactive radicals and hydroxyl (-OH) groups on the surface. Afterwards, the slides were placed and incubated in 3-mercaptopropyl-trimethoxysilane (3-MPS) (200 mM, in ethanol (10 mL)) at 25 °C for 1 h to augment the slide surfaces with thiol (-SH) groups. Subsequently, the parts of the chip were assembled, and (*N*-ρ-maleimidobutyryl-oxysuccinimide ester) GMBS (2 mM in ethanol) reagent was incubated by pausing the injection of fluid when the channels filled with the solution at 25 °C for 40 minutes. Since the GMBS reagent has thiol (-SH) groups on one-end, it binds and creates self-assembled monolayer structures on the surface of the glass slides via thioether linkages between maleimide groups and thiol groups. Furthermore, GMBS reagent holds a succinimide group at the other side in order to interact with amine groups of proteins [74]. Biotin protein (25 μg/mL prepared in water) was then injected to the channels and incubated for an hour. Once the incubation was over, the channels were washed with PBS for 3 times to remove unbound proteins.

4.3 RESULTS and DISCUSSION

4.3.1 Flow Simulations

By inspiring our previous work [155], the microfluidic channel reservoir was designed with a 1/10 aspect ratio (4 mm x 40 mm x 50 μm, width x length x height) (**Figure 4.2a**). Theoretically, flow velocity has a laminar flow characteristic, whereas the shear stress profile is higher at the edges of the microfluidic chip [149], and the general profile of shear stress in the channel is almost the same except inlet and outlet regions, including a minute portion of the channel. Therefore, we have investigated the shear stress profile from the middle of the channel with horizontal analyzing (1 and 2) and vertical analyzing (3 and 4) lines (**Figure 4.2b**). In particular, the microchannel fluid velocity and shear stress profiles were simulated until the flow is stabilized. As a note, t = 0 s states that the moment is the first time that fluid enters the chip from the inlet (0.4 mm diameter) and then exits from the outlet (0.4 mm diameter).

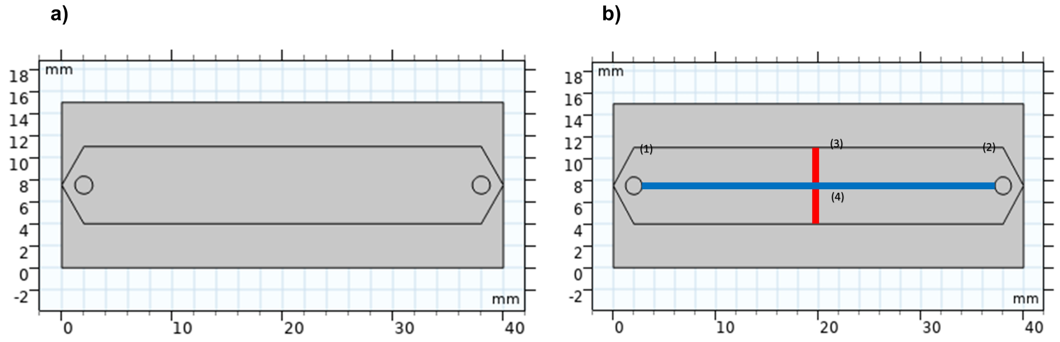

Figure 4.2: Simulation for designing a microfluidic chip. **a)** microchannel design is presented. For the analysis, **b)** horizontal (1 and 2) and vertical (3 and 4) lines are used.

4.3.2 Fluid Velocity Simulations

Initially, the flow velocity profiles were evaluated by different flow rates (5, 10, 20, 50, and 100 μL min^{-1}) while keeping the channel height (50 μm) constant at t = 0 s. (**Figure 4.3b-f**). The magnitude of flow velocity has increased at the middle of the microchannel, whilst it decreased at the edges and corners. Quantitatively, the highest velocity values were monitored at 5.71 x 10-4, 1.17 x 10-3, 2.27 x 10-3, 5.62 x 10-3, 0.01 m s^{-1}, for 5, 10, 20, and 100 µL min^{-1}, respectively. The lowest velocity profile was obtained at 5 µL min^{-1}, whereas the highest was observed at 100 µL min^{-1}. The fluid profile was stabilized and transformed to laminar flow.

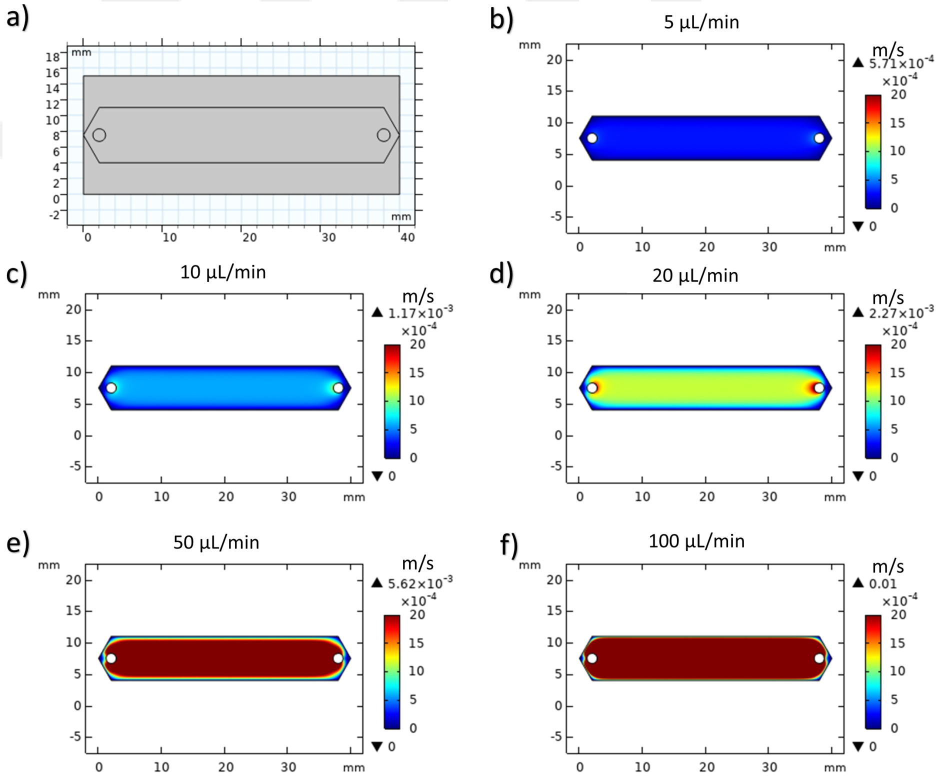

Figure 4.3: Microfluidic chip design is presented for the simulation. **a)** A microchannel design is depicted. The flow velocity profiles in **b)** 5 µL min^{-1}, **c)** 10 µL min^{-1}, **d)** 20 µL min^{-1}, **e)** 50 µL min^{-1}, and **f)** 100 µL min^{-1} of flow rates (at t = 0 s) are presented.

Furthermore, in order to assess time-dependent flow characteristics in the channels, flow velocity profiles were evaluated at t = 100 s and 1200 s for 10 μL min^{-1} (longer periods) while keeping the channel height constant (50 μm). The highest velocity values were monitored at 1.37 x 10-3 ve 1.22 x 10-3 m s^{-1} for 100 s and 1200 s, respectively (**Figure 4.4**).

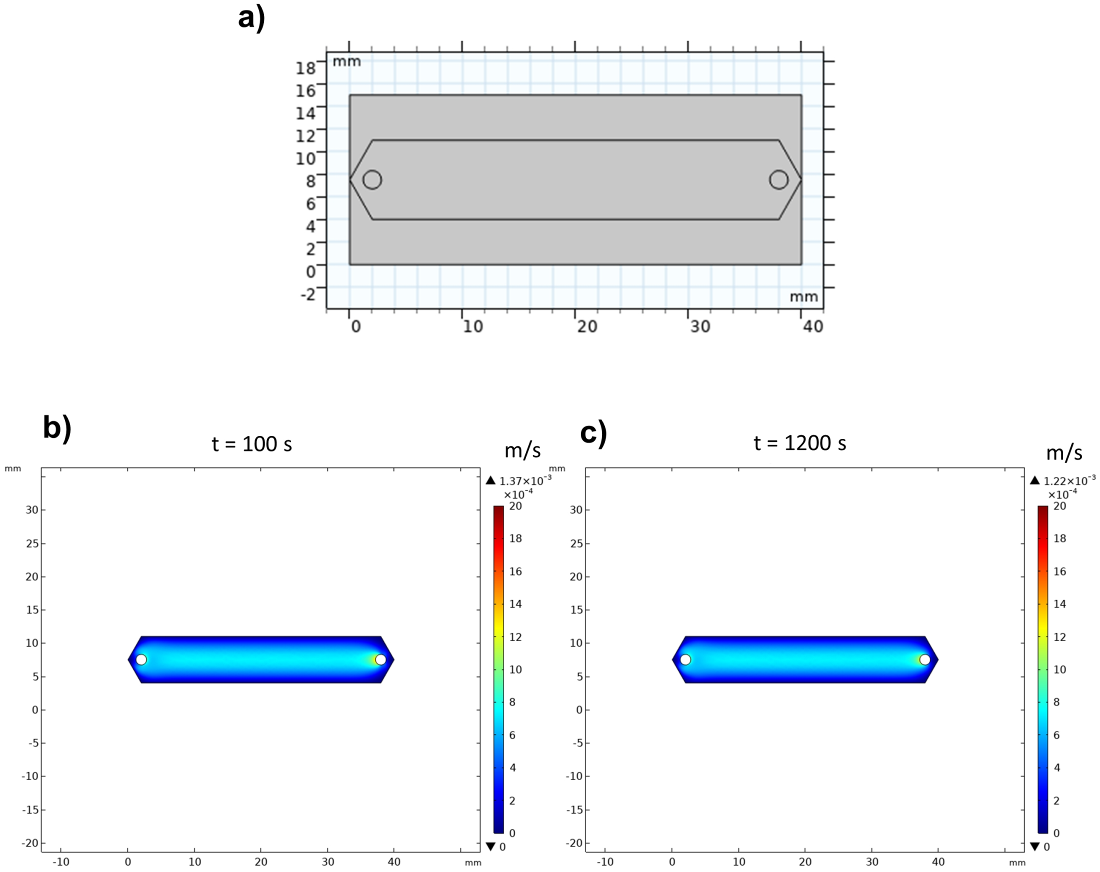

Figure 4.4: Microfluidic chip design is presented for the simulation. **a)** A microchannel design is depicted. The flow velocity profiles at 10 μL min^{-1} **b)** t = 100 s and **c)** t = 1200 s are shown.

4.3.3 Simulations For Shear Stress

After the flow velocity simulations, the shear stress profiles in the channel were investigated. The magnitude of shear stress increased at the edges of the microchannel, whilst it decreased at the corners. Similar to flow velocity simulations, we analyzed the shear stress for the flow rates between 5 and 100 µL min^{-1} at t = 0 s (**Figure 4.5**). We used the line analysis method through four (1-2 and 3-4) different regions and two (blue horizontal line and red vertical line) different analyzing lines. As a result, for the region of 1 (the inlet of the microchannel), the shear stress values were evaluated as 0.08, 0.15, 0.30, 0.74, and 1.48 dyne cm^{-2}, whereas for the region of 2 (the outlet of the microchannel), the shear stress values were found as 0.10, 0.20, 0.38, 0.95, and 1.95 dyne cm^{-2} for 5, 10, 20, 50, and 100 µL min^{-1}, respectively. On the other analyzing line, for the region of 3 (the ceiling area of the microchannel), the shear stress values were obtained as 0.03, 0.07, 0.13, 0.33, and 0.67 dyne cm^{-2} whereas for the region of 4 (the bottom area of the microchannel), the shear stress values were demonstrated as a symmetric shear stress profile to the 3rd region. In addition, the shear stress values at the inlet and the outlet resulted in similar profiles. From the literature, the shear stress resulting from the bloodstream in the circulatory system is revealed as $\geq$0.1 dyne cm^{-2} in the micro-scale [156], and also, veins display a shear stress profile between 1-10 dyne cm^{-2} in the mili-scale [149]. Therefore, especially for 50 µL min^{-1} and 100 µL min^{-1} of flow rate parameters, the immobilization and stabilization of biomolecules were found struggling due to the shear stress profile in the microfluidic platforms.

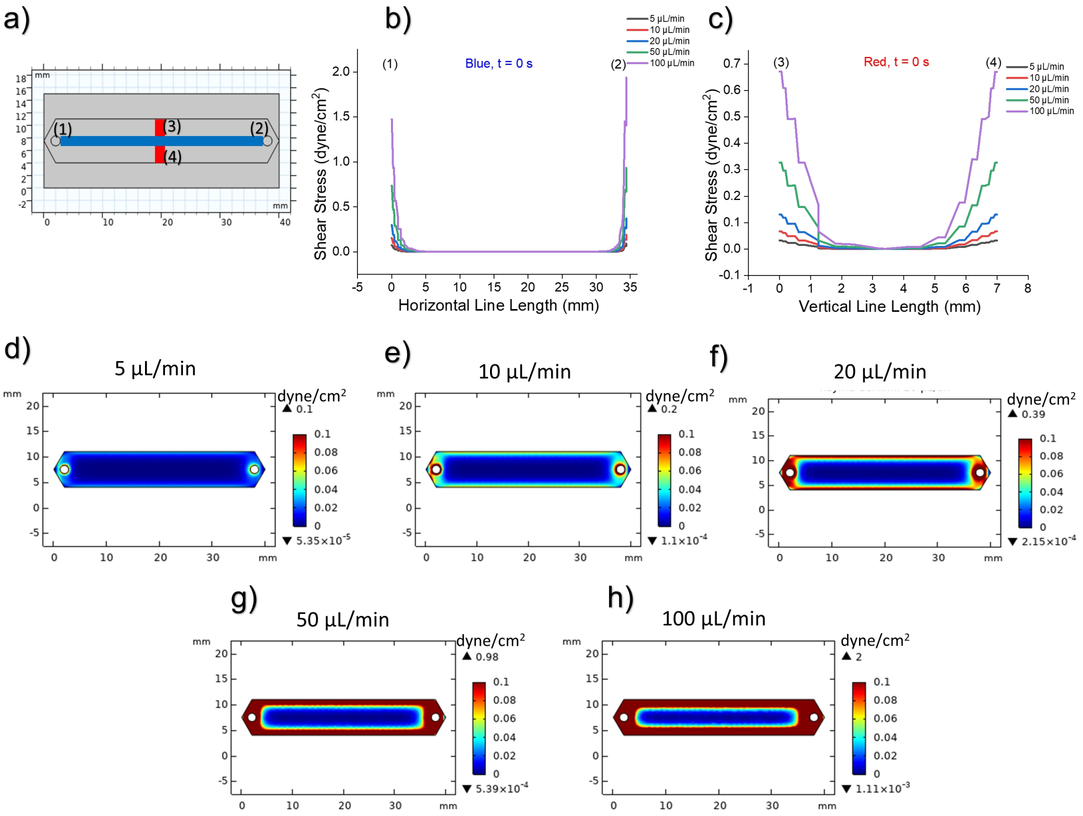

Figure 4.5: Microfluidic chip design along with analyzing lines is presented for the simulation. **a)** A microchannel design is depicted. **b)** Blue horizontal line and **c)** red vertical line results are shown. Shear stress profiles in **d)** 5 µL min^{-1}, **e)** 10 µL min^{-1}, **f)** 20 µL min^{-1}, **g)** 50 µL min^{-1}, and **h)** 100 µL min^{-1} of flow rates (at t = 0 s) are presented.

To evaluate the shear stress profile for a longer period of time, the shear stress was investigated at t = 100 s and 1200 s for 10 µL min^{-1} of flow rate while keeping the channel height constant (50 μm) (**Figure 4.6**). For the region of 1 (the inlet of the microchannel), the shear stress values were observed as 0.12 and 0.13 dyne cm^{-2}, whereas for the region of 2, the shear stress values were found as 0.09 and 0.19 dyne cm^{-2} for t = 100 s and 1200 s, respectively. On the other analyzing line, for the region of 3, the shear stress values were calculated as 0.036 and 0.37 dyne cm^{-2} whereas for the region of 4, the shear stress values were demonstrated as a symmetric shear stress profile to the 3rd region.

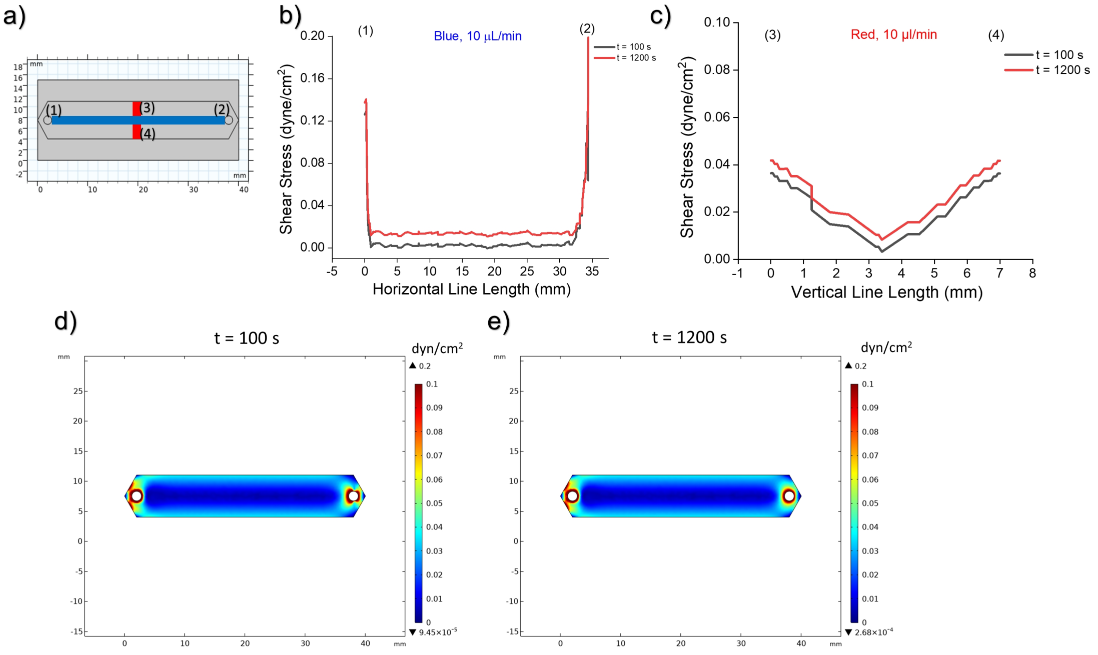

Figure 4.6: Microfluidic chip design along with analyzing lines is presented for the simulation. **a)** A microchannel design is depicted. Blue horizontal line and red vertical line are shown. Shear stress profiles at 10 µL min^{-1} are presented for **b)** blue **c)** red line profiles. Shear stress profiles at **d)** t = 100 s and **e)** t = 1200 s are presented.

In addition to the effect of flow rate on flow velocity and shear stress, the influence of different channel heights on shear stress was also investigated while keeping the time as t = 0 s (**Figure 4.7**). Since the channel height was determined by double sided adhesive (DSA) film thickness, the height-dependent shear stress profiles were examined for 25, 50, and 100 µm of channel height values via using the line analysis method. As a result of flow velocity and shear stress simulations, shown in **Figure 4.5**, we determined to continue with 5, 10, and 20 µL min^{-1} of flow values for further simulations due to the presence of low shear stress profile that enables more efficient immobilization. As depicted in Figure 30, at t = 0 s, for the vertical analyzing line, the shear stress values at the regions of 3 and 4 were evaluated as 0.016, 0.032 and 0,660 dyne cm^{-2} at 5 µL min^{-1}; 0.033, 0.068 and 0,135 dyne cm^{-2} at 10 µL min^{-1}, and 0.067, 0.132 and 0,264 dyne cm^{-2} at 20 µL min^{-1} for 100, 50, and 25 µm of channel heights, respectively. As shown above, the shear stress profile was similar at the top and bottom sides of the channel. The overall shear stress profile in the channels increased at the edges whilst it decreased in the central regions.

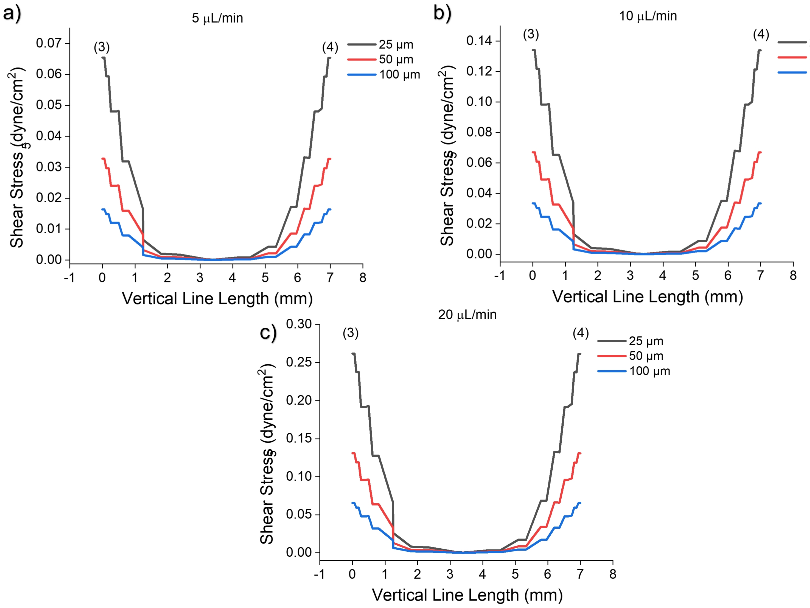

Figure 4.7: Shear stress profiles are depicted for different heights (25-50-100 μm) of channel; **a)** 5 µL min^{-1} **b)** 10 µL min^{-1}, and **c)** 20 µL min^{-1} of flow rates at t = 0 s.

4.3.4 Characterization of Testing Steps of Fabricated Chips

After numerical simulations and chip fabrication, the microfluidic platform was tested by applying specific surface chemistry and protein modification (**Figure 4.8a**). We initially characterized the surface chemistry developed on the chip via ATR-FTIR analysis spanning from 400 cm^{-1} to 4000 cm^{-1} of wavenumbers (**Figure 4.8b**). After each modification, ATR-FTIR was performed to the glass slide, 3-MPS, GMBS, and biotin-modified surface, respectively. As a result, the common stretchings and bending vibrations for each analysis were observed within 500-1000 cm^{-1} that indicate Si-CH_3 (asymmetric and symmetric SiO_3 (836 cm^{-1} and 581 cm^{-1}), and strongest on the glass surface 2950 cm^{-1} (-OH) was observed. After 3-MPS application, -OH stretching was suppressed. Although 3-MPS consists of thiol (-SH) groups, this stretching was not clearly observed as reported in the literature [157]. However, asymmetric and symmetrical -CH_2 bonds of 3-MPS, which are among the characteristic stretches of 3-MPS, appeared between 2800-3000 cm^{-1}. After the GMBS modification, the peaks were at 1600 cm^{-1} (C-H) and 1700 cm^{-1} (C-O), and the characteristic-CH_2 signal of biotin was detected between 2900-3000 cm^{-1} after the binding of biotin.

Here, we then performed contact angle measurements by operating the Contact Angle Measurement System (Dataphysics, OCA 30, Filderstadt, Germany) to characterize hydrophilicity and hydrophobicity after the surface chemistry was applied. The measurement was executed by drop-wisely adding 5 µL of ultrapure water (UPW) to the surfaces at sessile drop mode, and the images of these droplets were recorded. All measurements were repeated five times, and the resultant angles were analyzed through an in-house software. As a result, the bare glass surface provided relatively higher hydrophobicity (53.67° ± 8.49°) (**Figure 4.8c**). The contact angles after immobilizing 3-MPS and GMBS increased from 42.01° ± 7.72° to 67.97° ± 4.94°, respectively (**Figure 4.8d-e**). As can be seen from the literature, the surface tension of thiol (-SH) groups is lower than the other functional groups related to surface chemistries [158]. In contrast to the step of GMBS, the contact angle after capturing biotin decreased to 46.56° ±

4.48°, pointing out more hydrophilicity (**Figure 4.8f**). Taking together, the outcomes from two distinct, but complementary assessments confirmed the successful construction of our surface chemistry in the channel (**Figure 4.8g**).

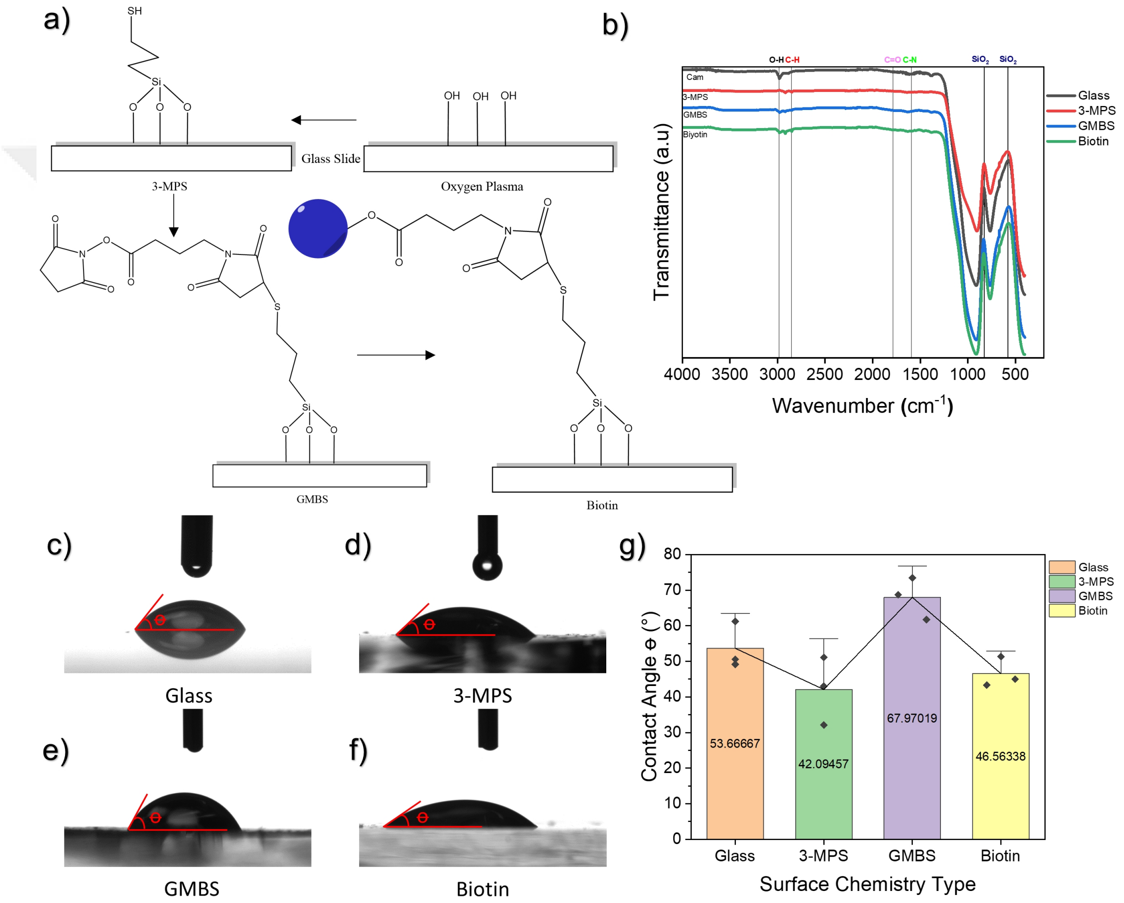

Figure 4.8: The characterization of surface chemistry on a microfluidic chip is illustrated. **a)** Surface chemistry steps include oxygen plasma, 3-MPS, GMBS, and biotin treatment, respectively. **b)** FTIR analysis is presented. **c-f)** Contact angle images, and **g)** their results are shown.

Next, XPS (K-Alpha XPS, ThermoFisher Scientific, U.S.A) was performed to characterize the surface chemistry in terms of chemical composition and chemical state developed in the channel. Initially, XPS analysis of O1s (532.42 eV), N1s (400 eV), C1s (285.04 eV), Si2s (153.21 eV), and Si2p (102.78 eV) scans were performed for the glass slide, 3-MPS, GMBS, and biotin-applied surfaces (**Figure 4.9**). C1s peak was stronger at the 3-MPS, GMBS, and biotin modification, whereas Si2s (153.21 eV) and Si2p were weak in these modifications. 3-MPS modified surface presented the S2p (217.05 eV) signal due to sulfur content. After applying GMBS to the same surface, the N1s (398.03 eV) peak appeared due to the nitrogen content. Finally, N1s and S2p signals were observed as a result of biotin application on the same surface.

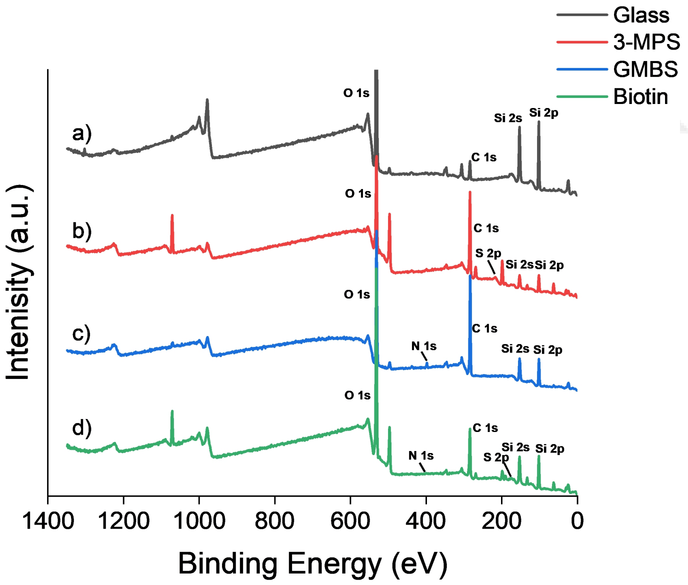

Figure 4.9: XPS general survey spectra of **a)** glass slide, **b)** 3-MPS, **c)** GMBS, and **d)** biotin treatment are depicted.

In particular, in order to examine carbon (C) element binding (**Figure 4.10**), XPS results were analyzed via baseline correction and Gaussian function application. Corresponding peaks of C element for glass surface provided C-C (284.87 ± 0.06 eV) C-H (285.67 ± 0.25 eV), C-O (286.62 ± 0.10 eV), and C=O (287.40 ± 0.11 eV) associated signals. For 3-MPS, the signals were found as C-C (284.61 ± 0.10 eV), C-H (284.90 ± 0.04 eV), and C-O (285.81 ± 0.23 eV) with higher intensities. After the GMBS application, the signal intensity increased even more and C-C (284.70 ± 0.14 eV), C-O (285.33 ± 0.85 eV), and C=O (286.42 ± 0.16 eV) signals were observed. After applying biotin protein, C-C (284.92 ± 0.11 eV), C-H (285.76 ± 0.07 eV), C-O (286.15 ± 0.51 eV), and C=O (288.49 ± 0.16 eV) peaks were observed. When the signal intensities of C1s were compared for each modification, the stretchings of C-H (183, 573, 20, and 471 a.u.), C-O (410, 2380, 2183, and 1045 a.u.), and lastly C=O (275, 30, 461, and 427 a.u.) were observed, respectively.

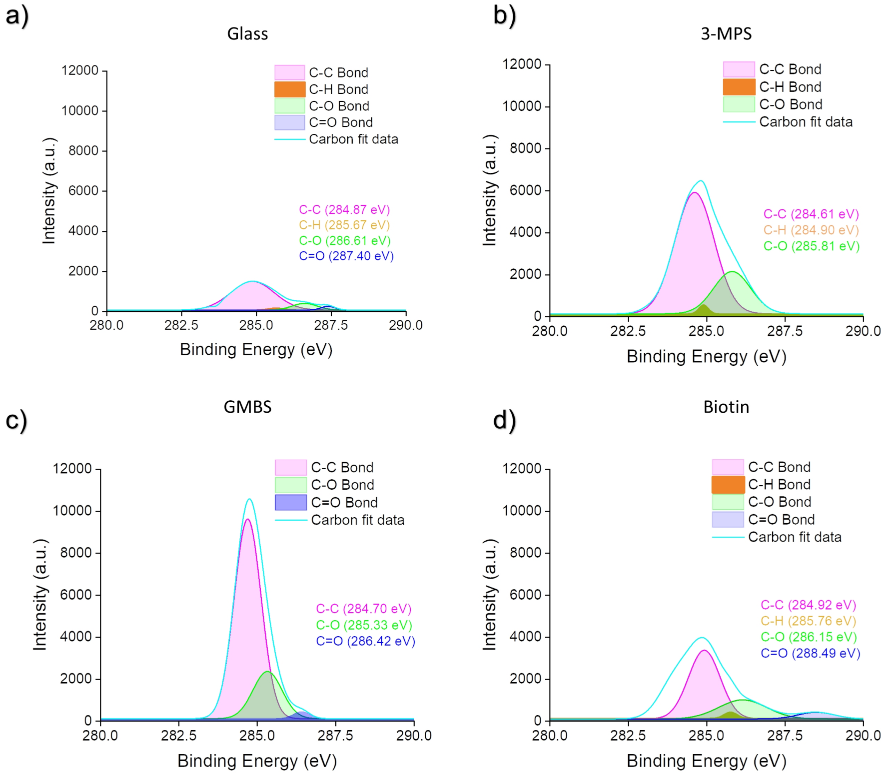

Figure 4.10: Carbon (C) spectra of **a)** glass slide, **b)** 3-MPS, **c)** GMBS, and **d)** biotin treatment are presented.

To survey oxygen (O) element bindings (**Figure 4.11**), XPS results were similarly analyzed via baseline correction and Gaussian function application. Corresponding peaks of O element for glass surface provided C-O (532.43 ± 0.01 eV) and C=O (532.71 ± 0.01 eV) associated signals. For 3-MPS, the signals were found as C-O (532.14 ± 0.10 eV), C=O (532.15 ± 0.30 eV), and O-H (536.63 ± 0.19 eV) with lower intensities. After the GMBS application, the signal intensity increased and C-O (532.37 ± 0.02 eV), and C=O (532.56 ± 0.01 eV) signals were observed. Once biotin was applied, the related peaks increased even more, and they were found as C-O (531.02 ± 0.39 eV), C=O (532.31 ± 0.07 eV), and O-H (535.68 ± 0.16 eV). If the signal intensities were compared for specific bonds, stretchings of C-O (8921, 7597, 5280, and 4142 a.u.), C=O (20984, 517, 7359, and 15161 a.u.) were observed. Lastly, for -OH bonding, only 3-MPS (797 a.u.) and biotin (1120 a.u.) were recorded.

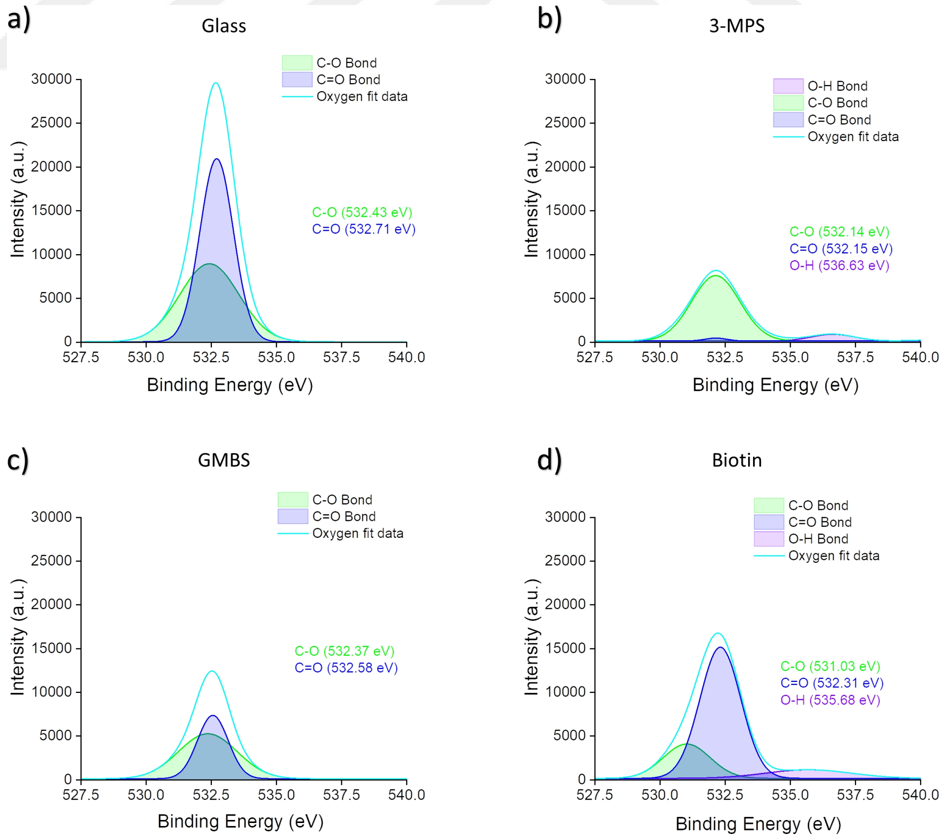

Figure 4.11: Oxygen (O) spectra of **a)** glass slide, **b)** 3-MPS, **c)** GMBS, and **d)** biotin treatment are depicted.

In addition, in order to assess silicon (Si) element bindings (**Figure 4.12**), similar pre analyses steps were applied. Corresponding peaks of Si element for glass surface provided SiO_2 (103.27 ± 0.01 eV) associated signal. For 3-MPS, the signals were found as Si-C (102.77 ± 0.05 eV) and SiO_2 (103.22 ± 0.10 eV) with higher intensities. After the GMBS application, the signal intensity increased even more and Si-C (102.91 ± 4.75 eV) and SiO_2 (103.37 ± 6.74 eV) signals were observed. After the application of biotin protein, the peaks were found as Si-C (101.34 ± 0.24 eV) and SiO_2 (102.68 ± 0.02 eV). When the signal intensities of Si were compared for each modification, the stretching of SiO_2 (6000, 286, 1582, and 2974 a.u.) was observed in each modification, and Si-C was observed for 3-MPS, GMBS, and biotin (1183, 745, and 265 a.u.), respectively.

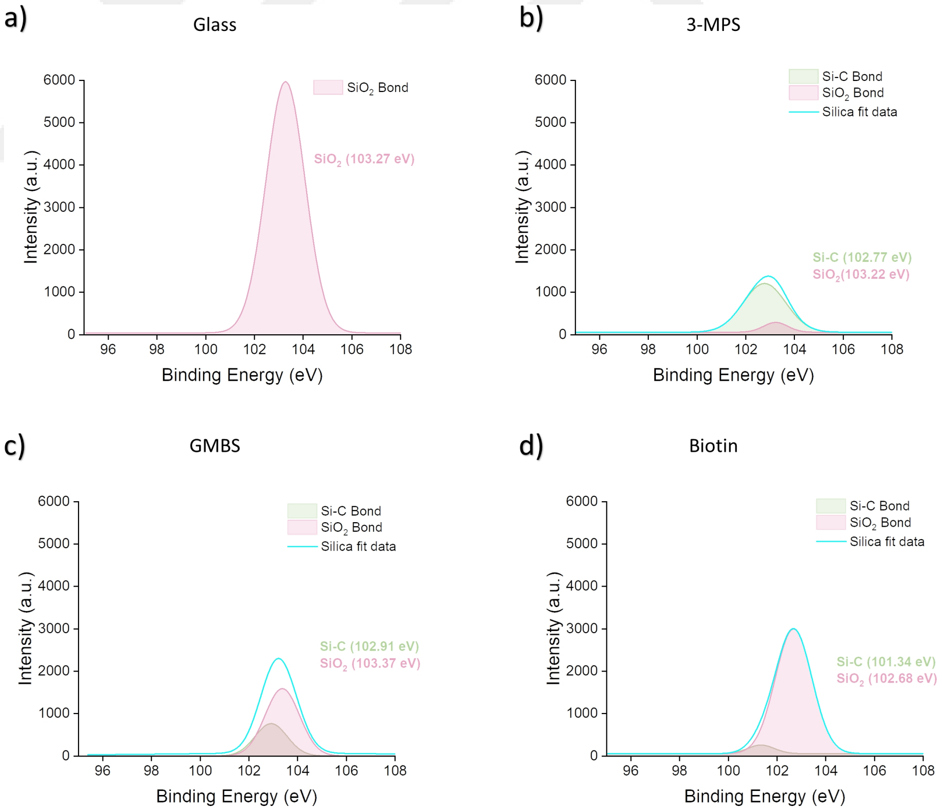

Figure 4.12: Silica/Silicon (Si) spectra of **a)** glass slide, **b)** 3-MPS, **c)** GMBS, and **d)** biotin treatment are demonstrated.

Lastly, in order to survey nitrogen (N) elements (**Figure 4.13**), XPS results were similarly analyzed via baseline correction and Gaussian function application. Corresponding peaks of N element provided only for GMBS ((C=O)-N-(C=O), 399.42 ± 0.02 eV) and biotin (C-N, 400.90 ± 0.58 eV) associated signals. For 3-MPS, the signals revealed C-O (532.14 ± 0.10 eV), C=O (532.15 ± 0.30 eV), and O-H (536.63 ± 0.19 eV) with lower intensities. After the GMBS application, the signal intensity increased and found as C-O at 532.37 ± 0.02 eV and lastly, C=O at 532.56 ± 0.01 eV. Finally, after applying biotin protein, the related peaks (C-O at 531.02 ± 0.39 eV, C=O at 532.31 ± 0.07 eV, and O-H at 535.68 ± 0.16 eV) increased even more. In addition, GMBS provided the stretching of (C=O)-N-(C=O) (420 a.u.), and biotin had the stretching of C-N (320 a.u.).

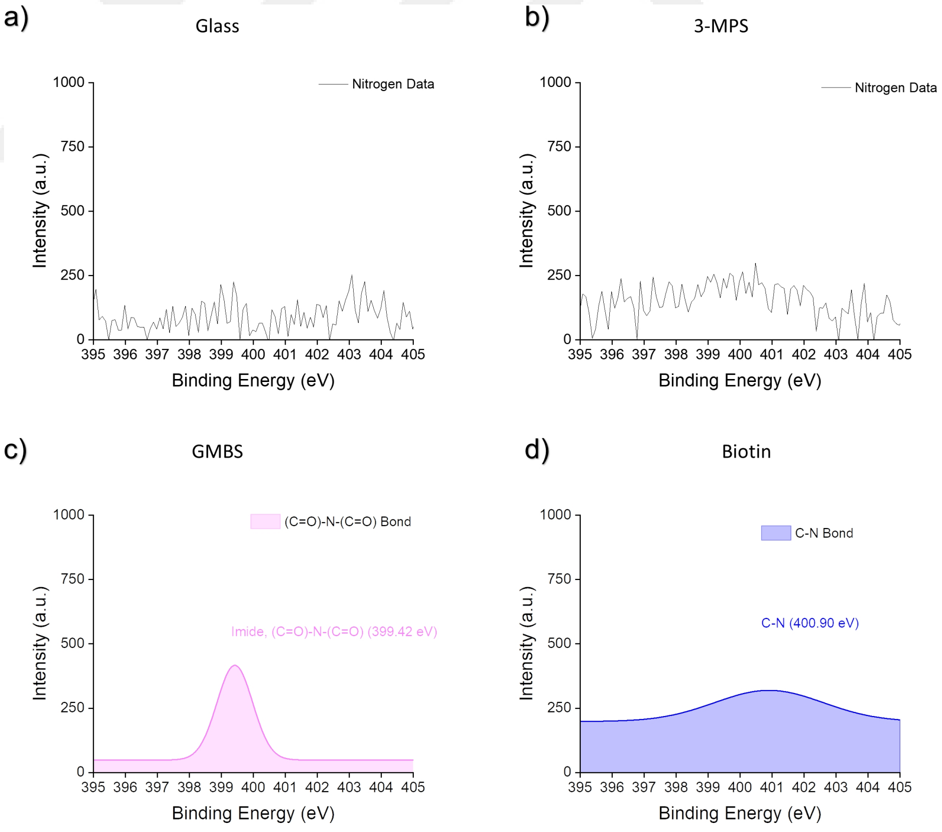

Figure 4.13: Nitrogen (N) spectra of **a)** glass slide, **b)** 3-MPS, **c)** GMBS, and **d)** biotin treatment are shown.

4.4 CONCLUSION

In sum, with the aim of stabilizing flow velocity and shear stress profile in the microchannel, we optimized the laminar flow characteristics to immobilize biomolecules into the channels with 5, 10, and 20 µL min^{-1} of flow rates. The topographic and biomechanic properties of microfluidics surfaces are the mainstay for controlling the shear stress profile. For example, in living creatures, for minimal shear damages, the shear stress profile should be in the range of 0-0.5 dyne cm^{-2} as a result of the stream of the circulatory system [156]. Per the simulation results, due to higher shear stress and turbulence profile, we did not choose 20 µL min^{-1} of flow rate. Moreover, 5 µL min^{-1} of flow rate value was not enough to release CTCs from the microchannels, as well as requiring one magnitude more time for this process, and thus, we selected 10 µL min^{-1} of flow rate for further experiments. Moreover, typical shear stress profiles of microfluidic devices along with 50 and 100 µm of channel heights were found more suitable for biomolecule immobilization due to low shear stress profiles. Although the shear stress was lower at 100 µm of channel height, we determined to use 50 µm of channel height by considering the usage of less volume of reagent, and possible higher interactions between biomolecules and channel surface. Furthermore, biotin was successfully bound to the glass surface by applying layer-by-layer surface chemistry to channels. All the steps in surface chemistry were characterized by FTIR, XPS, and contact angle analyses, and we observed the successful binding of proteins in the channels.

Chapter 5

DISTANCE-DEPENDENT SURFACE CHEMISTRY for DIFFERENT SHAPED BIOINSPIRED SMART POLYMERS/MATERIALS INTEGRATION into MICROFLUIDICS

5.1 INTRODUCTION: Length-Dependent Immobilization of Bio-Inspired Smart Polymers/Materials to Microfluidic Chips

In order to evaluate the optimum distance for biomolecules integration into the microfluidic design, as stated in the aim of the dissertation, three different distance-dependent surface linkers were assigned to tether into the microfluidic chip, including (i) short-length (1 nm, 3-mercaptopropyl-trimethoxysilane (3-MPS)), (ii) medium-length (7-9 nm, silane-polyethyleneglycol-thiol, 1 kDa (Silane-PEG-SH 1k)), and (iii) long-length (32-42 nm, silane-polyethyleneglycol-thiol, 5 kDa (Silane-PEG-SH 5k)) linkers. 3-MPS is mostly performed for modifying biosensor platforms in order to enhance the stability and sensitivity of surfaces by utilizing self-assembled monolayers (SAMs). On the other hand, PEG polymeric brushes have hydrophilic characteristics and they have been demonstrated to remain biocompatible and readily functionalizable properties [159].

5.2 MATERIALS and METHODS: Short-Medium and Long Modification

Briefly, (i) the short distance modification between polymer-integrated silica particles (bio-inspired smart polymers/materials) and the glass layer was enabled through the formation of a self-assembled monolayer (SAM) structure with the binding of 3-MPS molecules. The distance of silica particles from the microchannel surface is predicted to be equivalent to approximately 1 nm. For the size of (ii) medium (Silane-PEG-SH 1k) and (iii) long-distance interactions (Silane-PEG-SH 5k), the number of repetitive ethylene glycol molecules (n) were utilized for the length estimation of PEGylated surface modifications. The molar mass of PEG polymers was calculated by the following equation, (18.02 + (44.05 x n)) [160]. For instance, 22 sub-unit (ethylene glycol) was found in PEG 1k. Relying on the orientation of covalent bonds, each segment of sub-unit is between 0.278-0.358 nm

[161]. Hence, the medium and long-distance surface modifications are estimated between 7.1 - 8.9 nm and 32 – 42 nm, respectively.

Considering all these three distances, 3-MPS was decorated for the short distance (∼1 nm) from the glass slide part of the chips, whereas larger distances were obtained with Silane-PEG-SH 1k (∼7 nm - 9 nm) and Silane-PEG-SH 1k molecules (∼32 nm - 42 nm). Since all these modifications involve thiol (-SH) groups on one-end, they bind the surface of different-shaped p(NIPAAm)@SiO_2 via thioether linkages between maleimide groups and sulfhydryl groups. Furthermore, all of the length-dependent linkers hold a silane group at the other side to bind the glass layer of the microfluidic platforms. After all the modifications were performed, avidin-FITC protein was initially applied to length-dependent substrates and fluorescence signals of specimens were correlated in order to find the optimum distance for the experiments.

5.2.1 Short Modification

By considering the distance from the glass slide part of the chips, three different modifications were designed as detailed above. In the first one—short modification, we initially cleaned glass slides, and treated them with oxygen plasma (100 W, 2 min). After this step, the glass slides were placed and incubated in 3-MPS (200 mM, in ethanol (10 mL)) at 25 °C for 1 h to augment the slide surfaces with thiol (-SH) groups [162], thereby forming approximately 1 nm of distance from the surface. Briefly, 3-MPS contains a thiol group at one-end that binds to the surface of different-shaped p(NIPAAm)@SiO_2 . Considering the favor of thiol groups, maleimide groups (from surface modification of different-shaped p(NIPAAm)@SiO_2 described in **(Chapter 3)** of different-shaped p(NIPAAm)@SiO_2 react with thiol groups known as thiol-Michael addition [163], as well as 3-MPS presents silane groups at the other side of the molecule for binding to the glass layer of the microfluidic platforms. After the incubation of the ingredients, the glass slides were rinsed with ethanol. Next, the glass slides were assembled with a microfluidic chip for further use. The different-shaped p(NIPAAm)@SiO_2 (100 µg/mL) particles were injected to separate microchannels through tubes and incubated at 25 °C for 1 h. Then, the surface of the glass slides was washed with dH_2O three times (**Figure 5.1**).

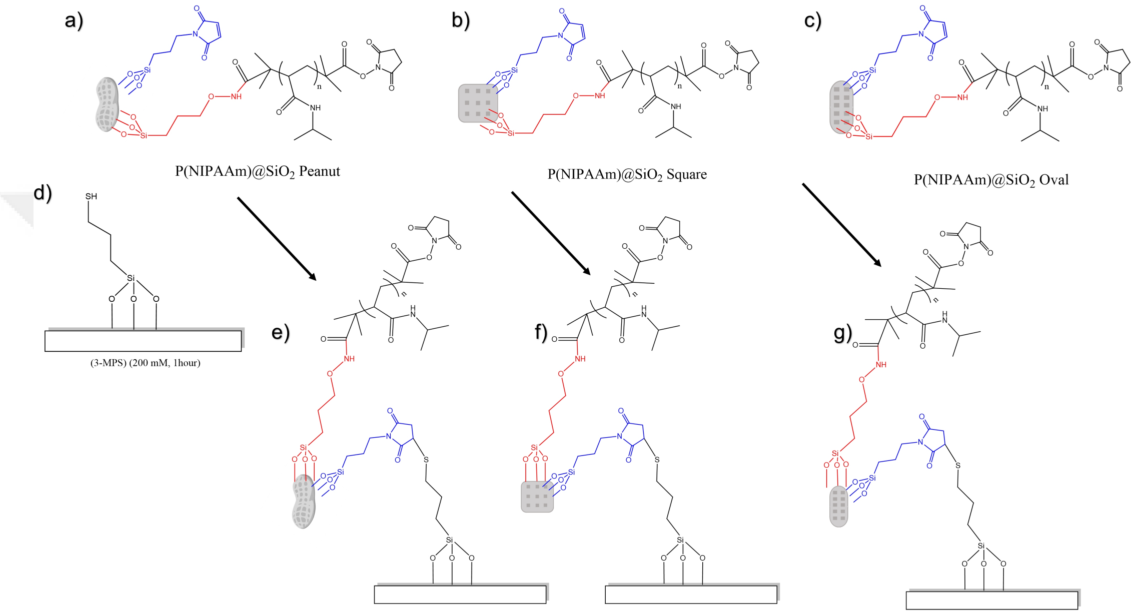

Figure 5.1: Short (3-MPS) modification onto the glass surface and immobilization of different shapes of p(NIPAAm)@SiO_2 particles are depicted. **a)** Peanut **b)** square **c)** oval shapes of p(NIPAAm)@SiO_2 particles are modified with maleimide. The schematic of **d)** 3-MPS modified glass surface, and different shapes of particles integration onto 3-MPS modified surfaces including **e)** peanut **f)** square, and **g)** oval shapes.

5.2.2 Medium Modification

For the medium modification, Silane-PEG-SH 1k was utilized to develop tethering layers ranging from ∼7 nm to ∼ 9 nm. Similarly, thiol-ends (-SH) of these polymers bind to the surface of different-shaped p(NIPAAm)@SiO_2, and at the same time, they denote silane groups for binding to the glass surface of the microfluidic platforms. For this process, 10 mg/mL of Silane-PEG-thiol (Silane-PEG-SH 1k (1 kDa) NANOCS INC.) was dissolved in dH_2O, and injected into 3 different microfluidic channels for an hour at a 10 µL min^{-1} of flow rate. Afterwards, the microfluidic chips were washed with dH_2O for 5 minutes. Later, peanut, square, and oval shapes of p(NIPAAm)@SiO_2 (100 µg/mL) (dispersed in ethanol) particles were separately introduced through tubes at a 10 µL min^{-1} of flow rate and incubated by pausing the injection of fluid when the channels filled with the solution at 25 °C for an hour. After all modifications were accomplished, the surface of the glass slides was cleaned with dH_2O for 5 minutes (**Figure 5.2**).

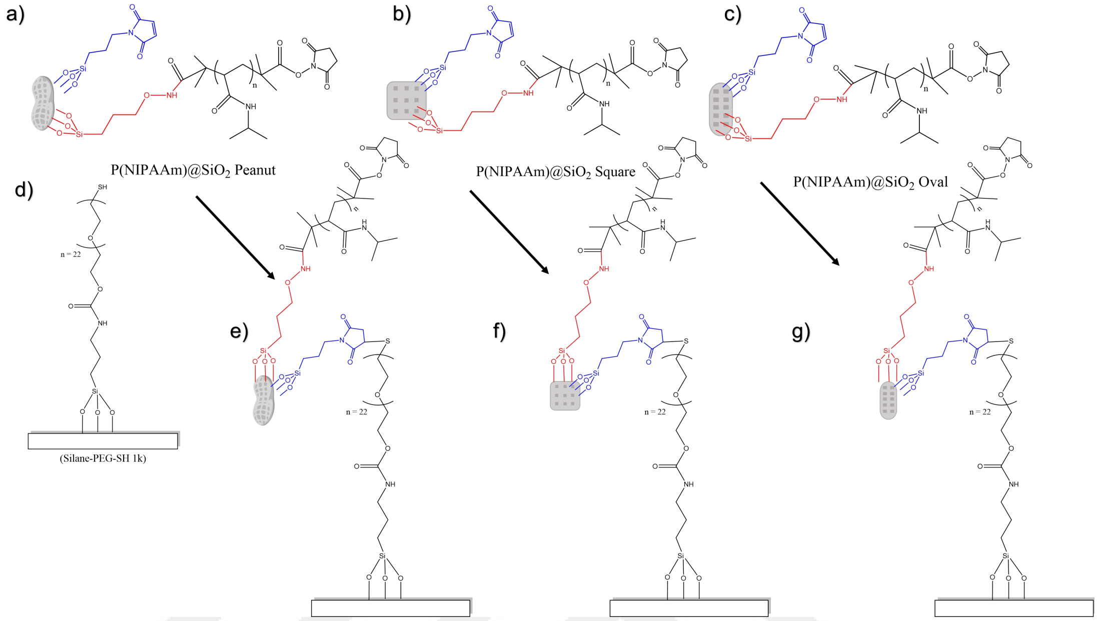

Figure 5.2: Medium (Silane-PEG-SH 1k) modification onto the glass surface and immobilization of different shapes of p(NIPAAm)@SiO_2 particles are depicted. **a)** Peanut **b)** square **c)** oval shapes of p(NIPAAm)@SiO_2 particles are modified with maleimide. The schematic of **d)** Silane-PEG-SH 1k modified glass surface, and different shapes of particles integration onto Silane-PEG-SH 1k modified surfaces including **e)** peanut **f)** square, and **g)** oval shapes.

5.2.3 Long Modification

For the long modification, Silane-PEG-SH 5k was utilized to develop tethering layers ranging from ∼32 nm to ∼ 42 nm. Similar to 3-MPS and Silane-PEG-SH 1k, thiol-ends (-SH) of these polymers bind to the surface of different-shaped p(NIPAAm)@SiO_2, and at the same time, they provide silane groups for binding to the glass layer of the microfluidic platforms. In this manner, 10 mg/mL of Silane-PEG-thiol (Silane-PEG-SH 5k (5 kDa) NANOCS INC.) (dissolved in dH_2O) was injected into 3 different microfluidic channels for an hour at a 10 µL min^{-1} of flow rate. After that, the microfluidic platforms were washed with dH_2O for 5 minutes. Afterwards, peanut, square, and oval shapes of p(NIPAAm)@SiO_2 (100 µg/mL) (dispersed in ethanol) particles were separately introduced through tubes at a 10 µL min^{-1} of flow rate and incubated by pausing the injection of fluid when the channels filled with the solution at 25 °C for an hour. After all modifications were completed, the surface of the glass slides was cleaned with dH_2O for 5 minutes (**Figure 5.3**).

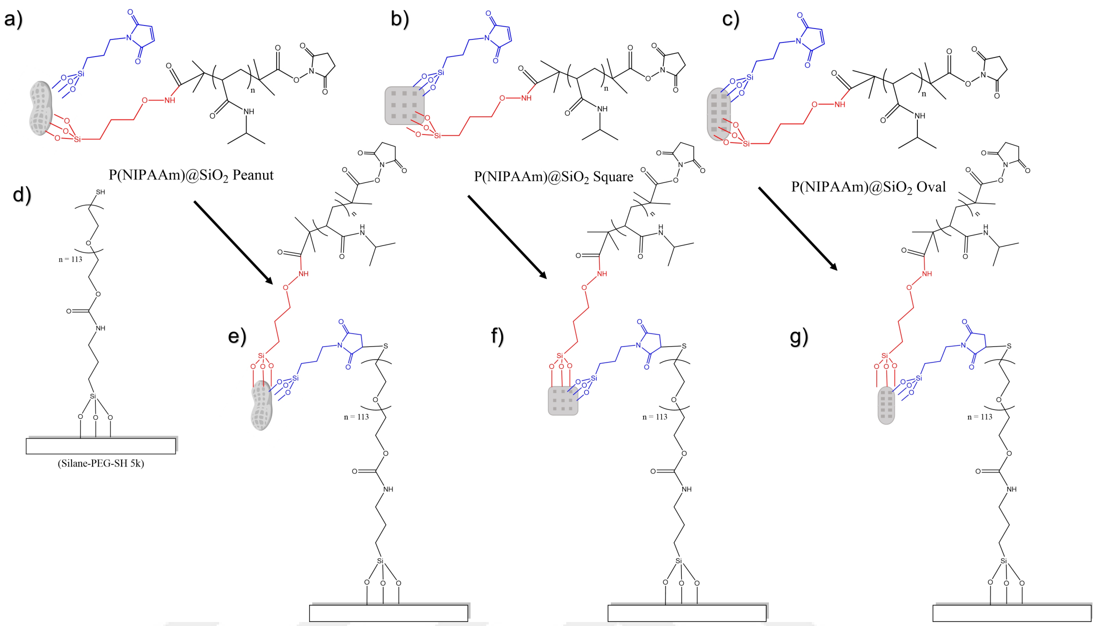

Figure 5.3: Long (Silane-PEG-SH 5k) modification onto the glass surface and immobilization of different shapes of p(NIPAAm)@SiO$_2$ particles are depicted. **a)** Peanut **b)** square **c)** oval shapes of p(NIPAAm)@SiO$_2$ particles are modified with maleimide. The schematic of **d)** Silane-PEG-SH 5k modified glass surface, and different shapes of particles integration onto Silane-PEG-SH 5k modified surfaces including **e)** peanut **f)** square, and **g)** oval shapes.

5.3 RESULTS and DISCUSSION

5.3.1 Characterization of Length-Dependent Modifications

As stated above, three different length-dependent surface chemistry approaches were assigned to assess the optimum length for the immobilization of silica particles. In this manner, we employed some chemical and polymeric linkers to tune the distance as detailed above. Once the microfluidic chips were decorated with three linkers (short, medium, and long-distance linkers), contact angle, AFM, XPS, and SEM analysis were performed to determine the success of the surface modifications, and also to find the compositions and chemical states of substrates.

Initially, we performed contact angle measurements by operating the Contact Angle Measurement System (Dataphysics, OCA 30, Filderstadt, Germany) to characterize hydrophilicity and hydrophobicity after the length-dependent surface chemistry application [164]. The measurement was executed by drop-wisely adding 5 µL of ultrapure water (UPW) to the surfaces at sessile drop mode, and the images of these drops were recorded. Accordingly, the resultant angles were analyzed through an in-house software (n=3). The bare surface provided relatively higher hydrophobicity than the surface modifications (53.67° ± 8.49°) (**Figure 5.4a**). The contact angle values were taken for each modification separately. (i) After the short modification (3-MPS), the contact angle decreased to 38.76° ± 5.82°; (ii) for the medium size modification, the contact angle decreased to 40.20° ± 1.01°; and finally (iii) for the long modification, the contact angle was higher than medium modification 42.63° ± 1.53° (**Figure 5.4b-d**). In sum, the short modification (3-MPS) provided more hydrophilic characteristics than PEG integrated substrates, which support the literature [165]. Basically, Silane-PEG-SH groups create self-assemble structures, and the contact angle of the surface increase when the chain number of PEG increases. Our results also confirmed this outcome from the literature as well (**Figure 5.4e**) [165].

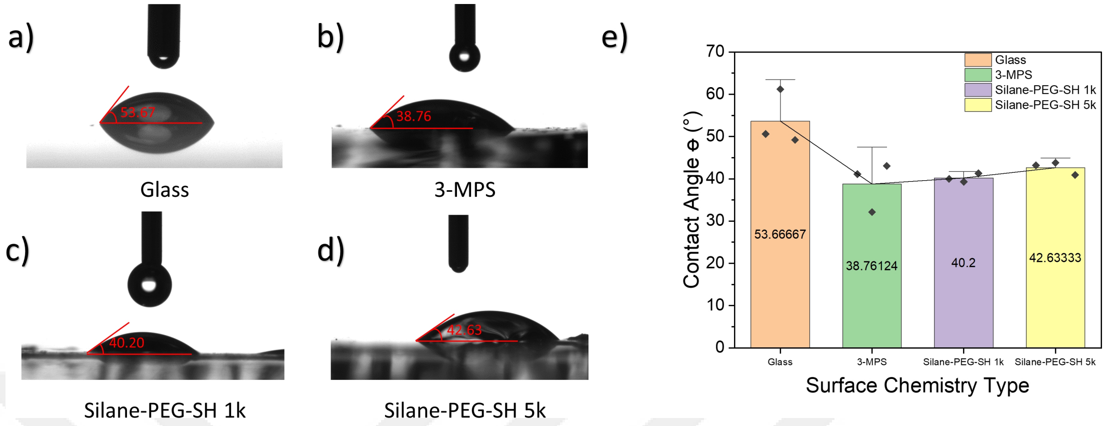

Figure 5.4: Contact angle analysis is performed for **a)** 3-MPS, **b)** Silane-PEG-SH 1k, and **c)** Silane-PEG-SH 5k modifications onto the glass, and **e)** their overall results are presented.

The nano-scale imaging of the short, medium, and long-distance linkers modified surfaces was carried out via Atomic Force Microscopy (AFM) (Asylum, Oxford Instrument, U.K.) in order to measure the height of modifications, topographic characteristics, and profiles (**Figure 5.5**). For the AFM analysis, a cantilever (Nanosensors PPP-NCHR tip) using 42 N m^{-1} force constant was employed on AC Air Topography mode. Imaging was performed with a scan rate of 0.6 Hz, and the images were evaluated using Gwyddion with aligning rows via 4th-degree polynomial fitting. According to the AFM results, the roughness values were found as 6.82 nm, 10.57 nm, and 35.3 nm for short, medium, and long modification, respectively. In addition, the maximum height points of the modifications were evaluated as 16.3 nm, 40.5 nm, and 114.7 nm. If the experimental data is compared to theoretical length calculations, medium and long modification evaluations are matching to our data. On the other hand, the short modification's roughness value was higher than the calculated value due to the fact that the cantilever tip and the taping mode restrict to measure below a certain value. Furthermore, as can be seen from line analysis, the texture of the modified substrates was enlightened that the short modification's overall height profile is <5 nm, whereas the medium linker is between 5-10 nm and the long is around 30 nm height. As a result, the experimental and theoretical data have matched according to numeric evaluations and AFM results.

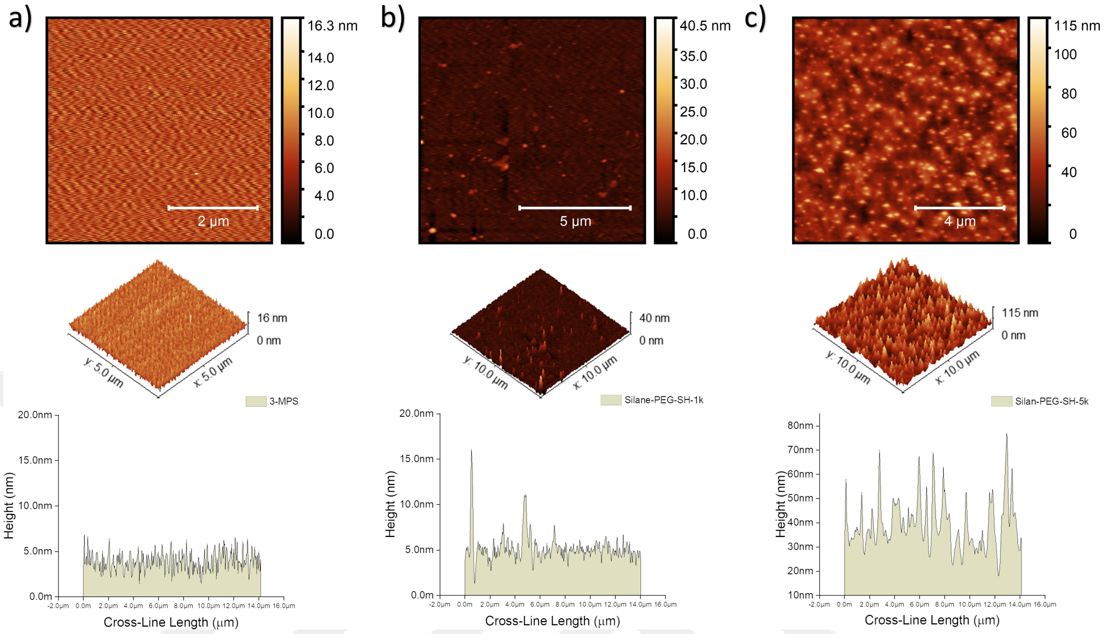

Figure 5.5: AFM images, topographies, and line analysis of **a)** glass, **b)** 3-MPS, **c)** Silane-PEG-SH 1k, and **d)** Silane-PEG-SH 5k modifications are presented.

Afterwards, once the microfluidic surfaces were decorated with short (3-MPS) and medium (Silane-PEG-SH 1k) linkers, XPS analysis was operated to determine the chemical states in 3-MPS and PEG chains' material and elemental composition by utilizing the photoelectric effect. The measurements were taken place in the XPS tray by cutting the bottom layer (glass slide) of microfluidics (1 cm x 1cm). Here, we evaluated the composition of each surface modification applied onto glass substrates (**Figure 5.6**). The elements of C1s, O1s, Si2s, and Si2p were found as common contents for each modification, while 3-MPS, and Silane-PEG SH 1k, were provided S2p element, and N1s was encountered only in Silane-PEG SH 1k.

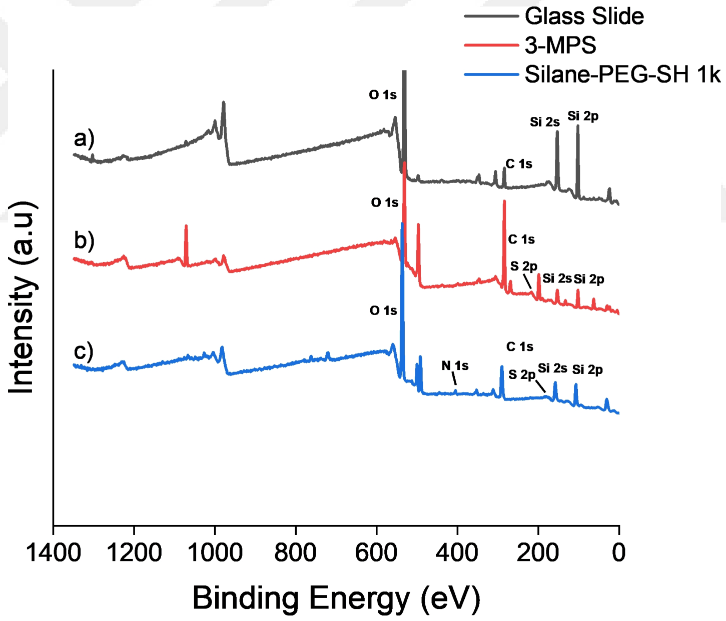

Figure 5.6: XPS general survey spectra of **a)** glass slide, **b)** 3-MPS, and **c)** Silane-PEG-SH 1k modifications are depicted.

Considering the scan of C1s for bare surface, short, and medium modifications provided four distinct peaks. XPS results were analyzed via baseline correction and Gaussian function application, and XPS analysis of each distance-dependent modification was performed separately. The bare surface's peaks were located at C-C (284.87 ± 0.06 eV) C-H (285.67 ± 0.25 eV), C-O (286.62 ± 0.10 eV) and lastly, C=O (287.40 ± 0.11 eV). After short (3-MPS) modification, the signal intensities increased, and they were C-C at 284.61 ± 0.10 eV, C-H at 284.90 ± 0.04 eV, and C-O at 285.81 ± 0.23 eV. For the Silane-PEG-SH 1k modified surfaces, signal intensities were lower compared to short modification, and associated signals were C-C at 283.72 ± 0.11 eV, C-H at 285.50 ± 0.33 eV, C-O at 286.71 ± 0.23 eV, and C=O at 288.71 ± 0.35 eV (**Figure 5.7**). When the signal intensities of C1s were specifically compared for different surface modifications, short modification provided the highest intensities for C-C and C-O.

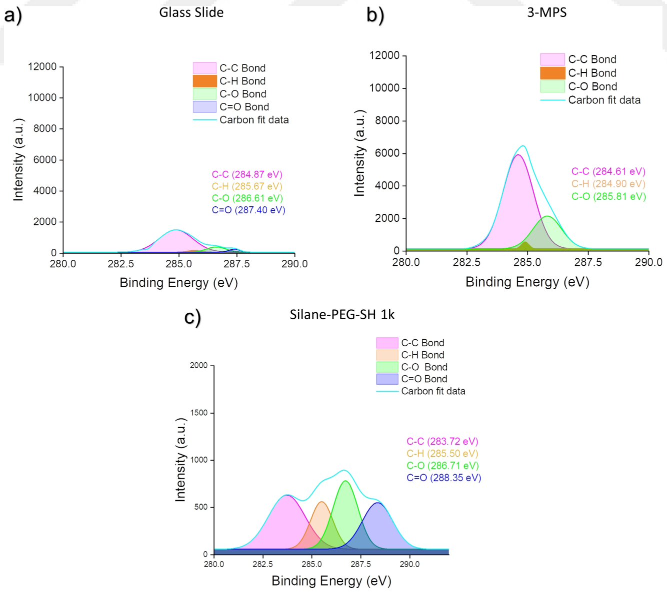

Figure 5.7: Carbon (C) spectra of **a)** glass slide, **b)** 3-MPS, and **c)** Silane-PEG-SH 1k modifications are shown.

In order to examine oxygen (O1s) element (**Figure 5.8**), XPS results were similarly analyzed as described above. Corresponding peaks of O element for glass surface were C-O at 532.43 ± 0.01 eV and lastly, C=O at 532.71 ± 0.01 eV. For short modification, the signals were found as C-O at 532.14 ± 0.10 eV, C=O at 532.15 ± 0.30 eV, and O-H at 536.63 ± 0.19 eV at with lower intensities. For the medium modification, the signal intensities were C-O at 528.75 ± 0.07 eV and C=O at 531.42 ± 0.31 eV. The related O bond densities were found to be the highest for bare glass due to the rich oxygen content in the natural structure of the glass surface. Comparing the other modifications, the short (3-MPS) modification had more intensity of oxygen content.

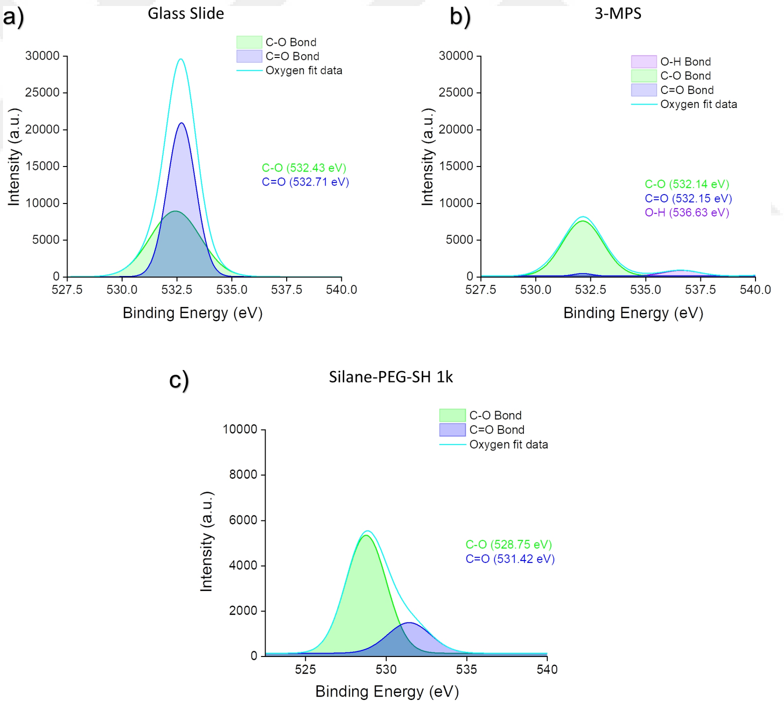

Figure 5.8: Oxygen (O) spectra of **a)** glass slide, **b)** 3-MPS and **c)** Silane-PEG-SH 1k modifications are depicted.

In order to examine Si element (**Figure 5.9**), XPS results were similarly analyzed. Corresponding peaks of Si element for glass surface provided SiO_2 (103.27 ± 0.01 eV) associated signal. For 3-MPS, the signals were found as Si-C (102.77 ± 0.05 eV) and SiO_2 (103.22 ± 0.10 eV) with higher intensities. For the medium modification, the signal intensities Si-C (104.63 ± 6.50 eV) and SiO_2 (105.05 ± 12.98 eV) signals were observed. When the signal intensities of Si element were specifically compared, due to the rich oxygen, as well as the presence of silicon content in the natural structure of the glass surface, Si bond densities were found to be high. If the other modifications were compared, it was seen that the short (3-MPS) modification had more intensity of oxygen content.

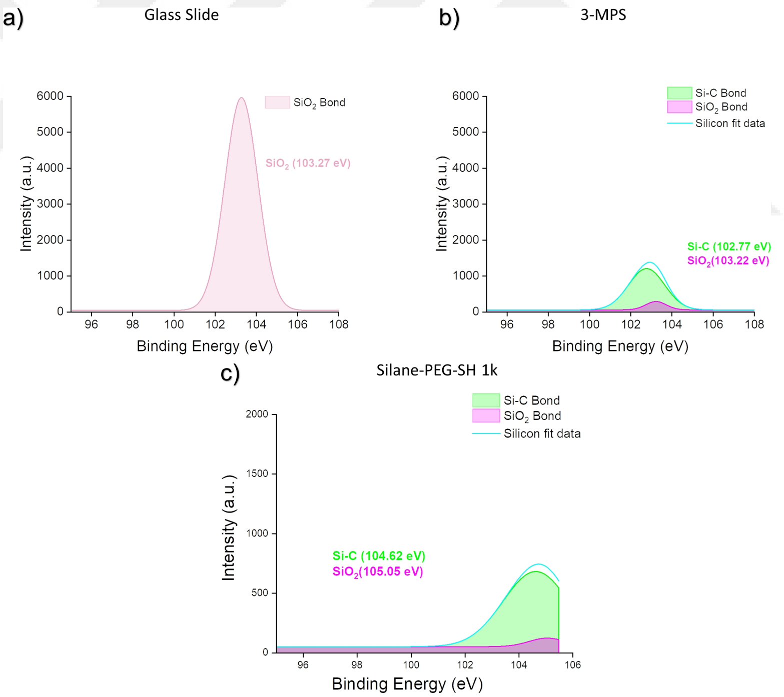

Figure 5.9: Silicon (Si) spectra of **a)** glass slide, **b)** 3-MPS, and **c)** Silane-PEG-SH 1k modifications are depicted.

Additionally, considering nitrogen (N) element (**Figure 5.10**) XPS measurements were performed. Corresponding peaks of N element for glass surface provided only for medium modification. For medium modification, the related peaks were evaluated as C-N/N-H (398.94 ± 0.35 eV). As reported in the literature [163, 166], when the glass substrate lacks of a thick layer of PEG chains, N1s peak intensity may not be high enough.

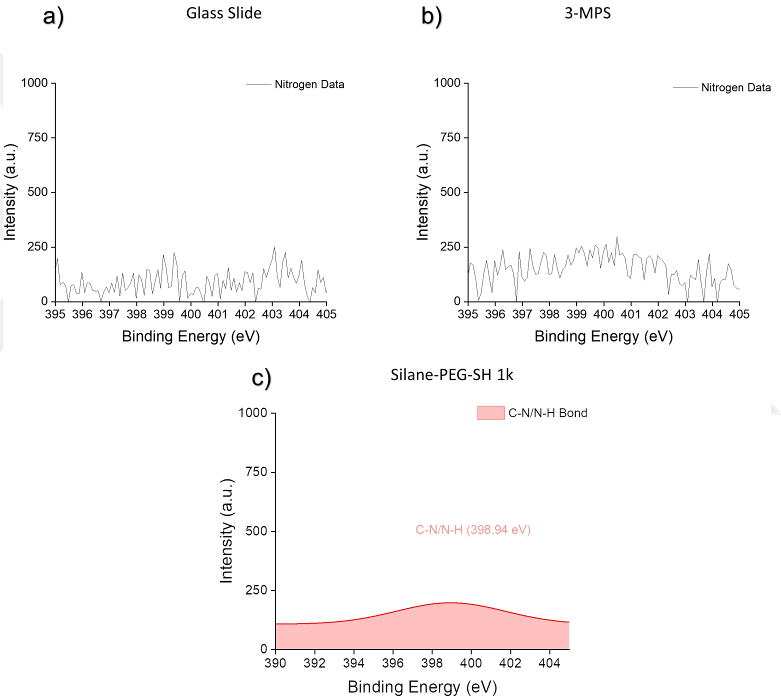

Figure 5.10: Nitrogen (N) spectra of **a)** glass slide, **b)** 3-MPS, and **c)** Silane-PEG-SH 1k modifications are presented.

Finally, in order to exami sulphur (S) element (**Figure 5.11**), XPS analysis was performed. Corresponding peaks of S element provided by for each distance-dependent modification except bare glass surface. Due to the rich thiol (-SH) content of the short (3-MPS) modification, the highest S element was observed in this modification. For 3-MPS, the signals were found as S-C/S-H at 158.15 ± 0.01 eV. For the medium modification, the signal intensities were shifted due to variation of silicon (Si2s) content in the PEG chains, and S-C/S-H bound was observed as (155.40 ± 0.03 eV).

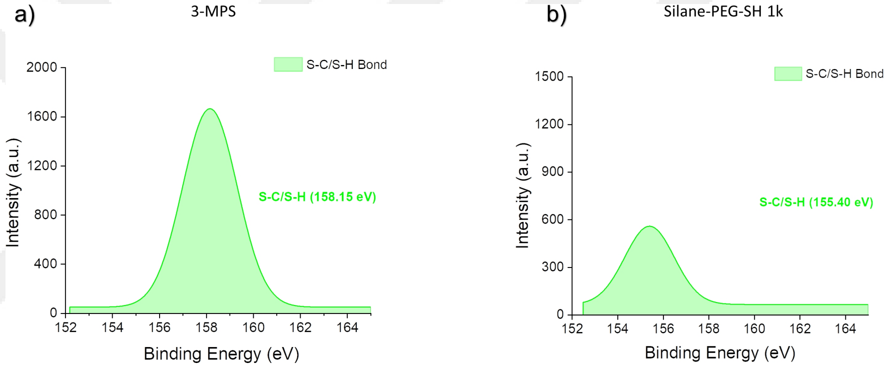

Figure 5.11: Sulphur (S) spectra of **a)** 3-MPS, and **b)** Silane-PEG-SH 1k modifications are depicted.

Once XPS analysis was accomplished, Scanning Electron Microscope (SEM, FEI Quanta 200 FEG) was performed. Here, we used peanut p(NIPAAm)@SiO_2 particles as a model for short, medium, and long-distance modified surfaces. Before the characterization takes place, in order to make the samples conductive, approximately 10 nm of gold-palladium (Au-Pd) mixture was coated into the substrates using the Precision Etching and Coating System (PECS). During this procedure, the device parameters were adjusted to a coating density of 19.32 g/cm^{3}s and an acoustic resistance of 23.20 x 105 gm/cm^{2}s (acoustic impedance). The measurements were performed by cutting the bottom layer (glass slide) of microfluidics (1 cm x 1 cm) for each modification. As a result of SEM characterization, p(NIPAAm)@SiO_2 particles bonded to the surface most intensely for the short (3-MPS) modification, and it was understood that there was a similar rate of particle adhesion for the medium and long modifications, yet more adhesion in the medium modification (**Figure 5.12**).

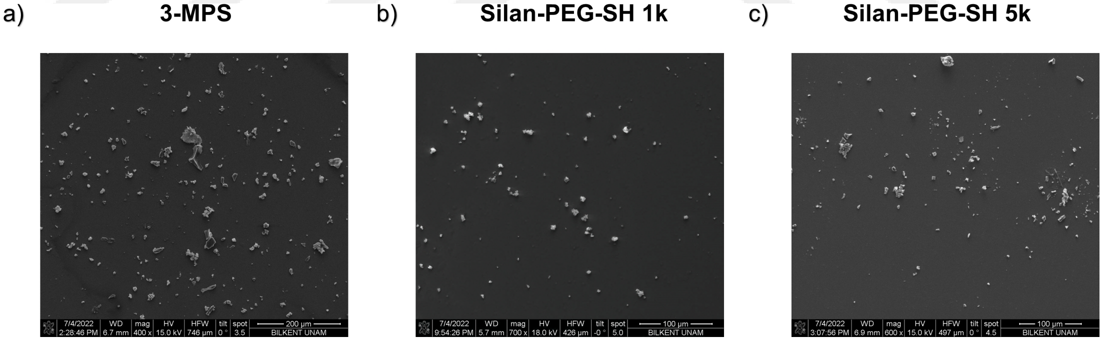

Figure 5.12: SEM images show the immobilization of model peanut p(NIPAAm)@SiO_2 particles on the surfaces which ware modified with **a)** 3-MPS, **b)** Silane-PEG-SH 1k, and **c)** Silane-PEG-SH 5k.

To observe any potential steric hindrance, short (3-MPS), medium (Silane-PEG-SH 1k), and long (Silane-PEG-SH 5k) linkers were modified with p(NIPAAm)@SiO_2. Then, biomolecule loading capacity was analyzed by applying avidin-fluorescein isothiocyanate (Avidin-FITC) protein to distance-dependent substrates in order to visualize absorption of them and find the optimum distance for further experiments. Avidin-FITC conjugate protein has an excitation and emission spectrum ∼494/518 nm. Avidin is a type of protein which consist can bind to glycosylated biotin, and it gives green light when we shine blue light into it. By using this property, we visualized the fluorescence intensity of distance-dependent avidin-FITC modified substrates to understand which modification has a better biomolecule loading capacity (**Figure 5.13**).

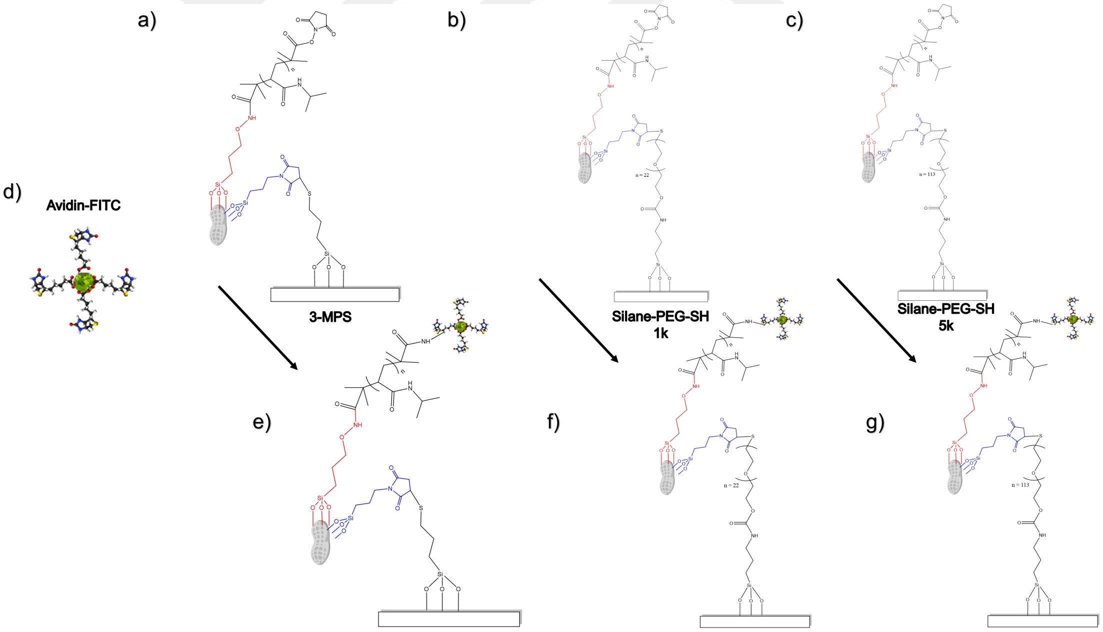

Figure 5.13: The schematic of **a)** short (3-MPS), **b)** medium (Silane-PEG-SH 1k), **c)** long (Silane-PEG-SH 5k) modified surfaces are represented. The illustration of **d)** avidin-FITC protein, and its interaction with **e)** short, **f)** medium, and **g)** long-distance linkers are shown.

After the modification of distance-dependent linkers to separate substrates, peanut shape p(NIPAAm)@SiO_2 (100 µg/mL) was applied to these chips, and after 1 hour of incubation time and cleaning the substrates with PBS, the first images were taken from p(NIPAAm)@SiO_2 introduced microchannels. Later, 150 nM of avidin-FITC was applied to the substrates for an hour, after cleaning the substrates to remove unbound proteins, new images were recorded through a fluorescence microscope (Upright fluorescence microscope, Zeiss) (n=3) (**Figure 5.14**). By using the characteristic green color of avidin-FITC, the green light intensity was employed to determine the amount of protein attached to the surface. The green color intensity increased for each modification, proving that all of the modifications interacted with avidin-FITC [167]. Additionally, the highest attachment of avidin-FITC protein was observed in the short (3-MPS) modification, which was followed by medium (Silane-PEG-SH 1k) and long (Silane-PEG-SH 5k) linkers modified substrates. When the green light intensity data were normalized (0-1), it was calculated as 0.34, 0.93, 0.34 and 0.25 for bare glass, medium (Silane-PEG-SH 1k) and long (Silane-PEG-SH 5k) linkers, respectively (**Figure 5.14d**).

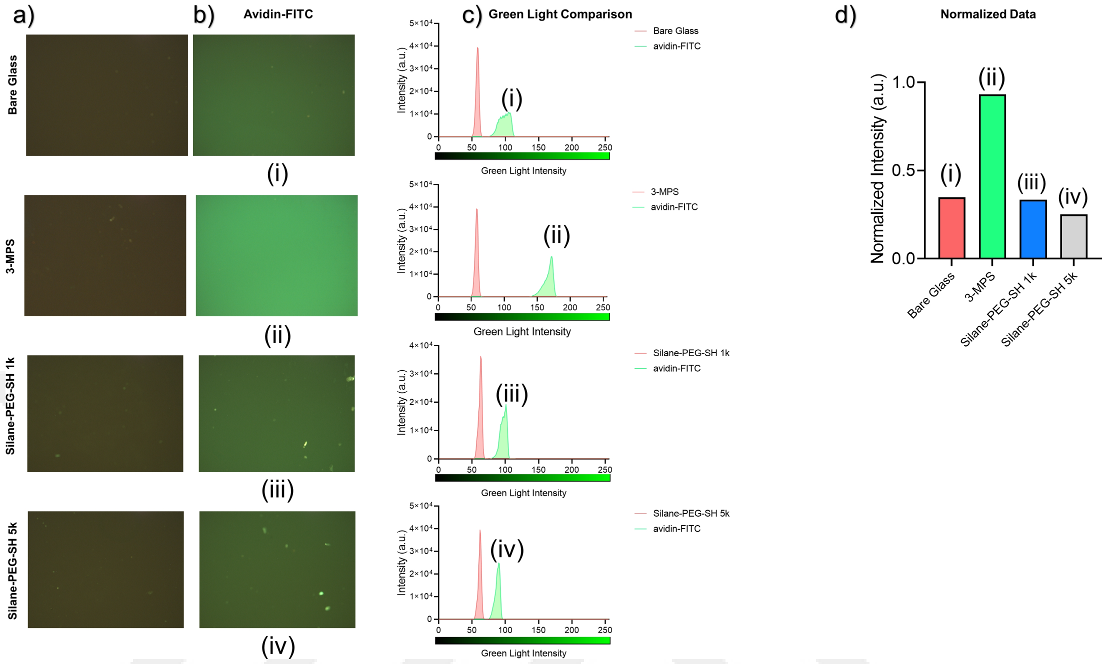

Figure 5.14: Avidin-FITC protein integration into bare glass, short (3-MPS), medium (Silane-PEG-SH 1k), and long (Silane-PEG-SH 5k) modified surfaces are depicted. **a)** Before avidin-FITC injection to the surfaces, **b)** avidin-FITC molecule modified surfaces, **c)** green light comparison, and **d)** normalized data are shown.

5.4 CONCLUSION

Taking together, the outcomes from five distinct characterization methods (contact angle, AFM, XPS, SEM, and Upright fluorescence microscopy) complementary assessments confirmed the successful construction of our length-dependent surface chemistry application on the microfluidic surfaces. As a result of the analyses, short (3-MPS) modification was found to be able to create highly active surfaces, thus it could absorb more proteins than the other distance-dependent modifications. Especially, the capture yield of the platform is a crucial parameter for such platforms. Therefore, we decided to continue with the short (3-MPS) modification for further experiments.

Chapter 6

TEMPERATURE SENSITIVE ADSORPTION and DESORPTION of MODEL PROTEINS on a CHIP

6.1 INTRODUCTION: Controlled Adsorption & Desorption of Model Proteins as a Preliminary Work

Before initiating actual experiments on the CTC capture and release, we performed preliminary experiments via model proteins through adsorption and desorption studies in the microfluidic chips. Protein adsorption and desorption incorporates profound science in physics and surface chemistry since high loading efficiency, capacity, minimum volume, low-cost and minimum non-specific interactions are required for extracting proteins from complicated biological samples [168]. Compared to conventional strategies, microfluidics would play a pivotal role in biomedical studies as it requires a small analyte volume, and provides high-throughput, and controllable manner in a short period of time [169]. Hence, we have designed efficient, accurate, and easy-to-use microfluidic chips that address real-world obstacles for the adsorption and desorption rate of proteins. To change, increase, and control the surface area of the microfluidic devices, bio-inspired different shapes of (peanut, square, and oval) silica particles were integrated with the short-length modification (3-MPS) applied chips. By harmonizing thermosensitive smart NIPAAm polymers with different-shaped silica particles by surface initiated atom transfer radical polymerization (ATRP) method, model protein adsorption and desorption can be controlled precisely across the LCST. In this part of the dissertation, we aim to investigate model proteins (bovine serum albumin (BSA) and avidin-fluorescein isothiocyanate (avidin-FITC) loading capacity into short distance-modified p(NIPAAm)-functionalized different-shaped silica particles via their ability to bind BSA and avidin-FITC noncovalently without altering biological functionality [126]. Furthermore, the effect of different temperatures on BSA and avidin-FITC desorption was examined for different shapes of p(NIPAAm)-functionalized silica particles on chip by measuring absorbance and fluorescence of the released products with a microplate spectrophotometer.

6.2 MATERIALS and METHODS: Model Proteins Adsorption & Desorption via Different-Shaped Bioinspired Smart Polymers/Materials in Microfluidics

To test the adsorption & desorption performance of the short-modified different shapes of (peanut, square, and oval) p(NIPAAm)@SiO_2 particles on chip, Bovine Serum Albumin (BSA) and avidin fluorescein isothiocyanate conjugate (avidin-FITC) were used as model proteins (**Figure 6.1**).

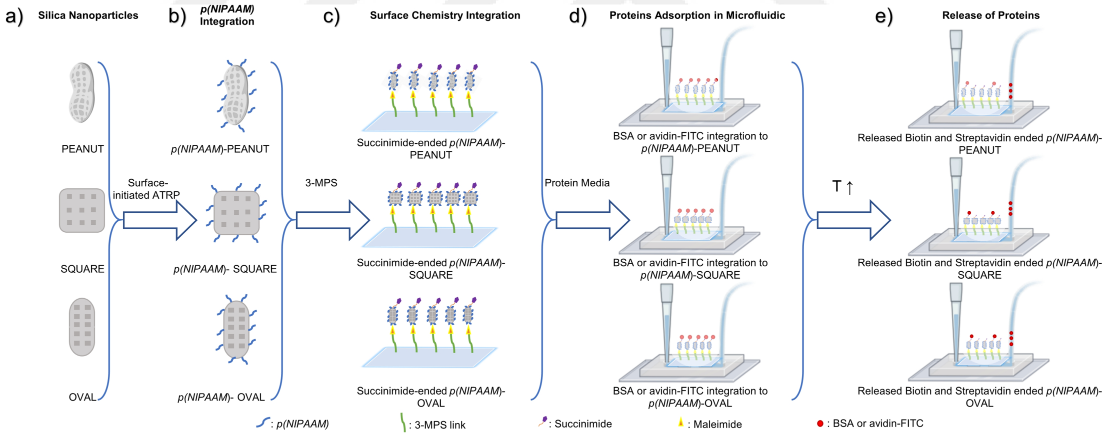

Figure 6.1: Avidin-FITC modification onto the microfluidic channels is depicted. **a)** Different shapes of silica particles are used in this study. **b)** NIPAAm polymer integration into different shapes of silica particles is shown. **c)** Surface chemistry integration. Short (3-MPS) modification into glass substrate and attachment of succinimide-ended p(NIPAAm)@SiO_2 particles are illustrated. Model proteins (BSA or avidin-FITC) are introduced into the microfluidic channels in order to **d)** adsorb, and then **e)** desorb via temperature increase.

6.2.1 The Integration of Peanut, Square, and Oval Particles Into Microfluidics

After the microfluidic device fabrication **(Chapter 4-section 2.2)**, different shapes of p(NIPAAm)@SiO_2 were immobilized on the microchannels. Initially, before bringing together the compartments of the chip, the glass slides were cleaned with ethanol; dried with the compressed air , and then, treated with oxygen plasma (100 W, 2 min) in order to increase reactive hydroxyl (-OH) radical groups on the inner surface of the chip. After enrichment of plasma, the glass surface has gained a more hydrophilic property [170]. Subsequently, the glass slides were placed and incubated in short modification (3-mercaptopropyltrimethoxysilane (3-MPS) (200 mM, in ethanol (10 mL))) at 25 °C for an hour to augment the slide surfaces with thiol (-SH) groups [162]. Therefore, maleimide groups (from surface modification of particles) of p(NIPAAm)@SiO_2 react with thiol groups known as thiol-Michael addition [163]. In this step, microfluidic chip compartments were assembled together. To tackle any possible steric repulsion on the glass surface, p(NIPAAm)@SiO_2 (100 µg/mL) particles were introduced through tubes and incubated at 25 °C for an hour. After all modifications successfully initiated, the surface of the glass slides was cleaned with dH_2O three times. This procedure was repeated for each peanut, square, and oval-shaped p(NIPAAm)@SiO_2 particles.

6.2.2 Model Proteins Adsorption via Different-Shaped Particles

To analyze the capture yield of the different shapes of p(NIPAAm)@SiO_2 on chip, Bovine Serum Albumin (BSA) and avidin fluorescein isothiocyanate conjugate (avidin-FITC) were used as model proteins. The model proteins were introduced to microfluidic channels with a 10:1 (protein :polymer) concentration ratio [171, 125]. Initially, in order to evaluate the capture efficiency and yield on the chips, BSA (1 mg/mL, dispersed in PBS (pH 7.4)) was injected through the different shapes of p(NIPAAm)@SiO_2 integrated chips at a 10 µL min^{-1} of flow rate for an hour with and without incubation. After injecting BSA into the microchannels, the flowing protein solutions were transferred to the Eppendorf's through the tubings. The amount of protein captured in the chips was evaluated as **(Equation 6.1)**. Model $Protein_{input}$ represents the introduced protein; and Model $Protein_{output}$ states non-captured protein after the injection process. Finally, the chips were rinsed with 1×PBS for further release experiments. The absorbance value of the BSA samples which are the transferred specimens to Eppendorf's tubes, were taken at 280 nm wavelength via the Microplate Reader (Multiskan GO, Thermo Scientific).

$$CaptureRatio = \frac{ModelProtein_{Input} - ModelProtein_{Output}}{ModelProtein_{Input}} x100 \tag{6.1}$$

The binding of avidin-FITC protein—emits green light when it is excited with a blue light source, was analyzed by fluorescence microscopy on different shapes of p(NIPAAm)@SiO_2 modified microchannels. The adsorption of the avidin-FITC (1 mg/ml, in water) model protein was performed via a syringe pump using a 10 µL min^{-1} of flow rate for 20 minutes, followingly incubated for an hour, and washed with water for 15 minutes to remove unbound avidin-FITC proteins.

6.2.3 Desorption of Model Proteins

The desorption/release of BSA proteins was taken place after PBS wash and the experiment was employed at 37 °C to demonstrate protein release alteration depending on the shape of the particles. After injecting BSA into the microchannels at 25 °C, the temperature was increased to 37 °C, and PBS solution was introduced to microfluidic chips to extract desorbed protein from the microfluidic chip. After that, the flowing solutions were transferred to the Eppendorf's tubes through the tubings at a 10 µL min^{-1} of flow rate after 1, 2, 4, and 8 hours of intervals. The release ratio of protein released in the chips was evaluated by utilizing **Equation 6.2**. Model $Protein_{output}$ represents the amount of desorbed protein during the release process, whereas Model Protein$_{capture}$ states the adsorbed protein during the capture process. The absorbance value of the flowing samples in Eppendorf's tubes were taken at 280 nm wavelength via the Microplate Reader (Multiskan GO, Thermo Scientific).

$$ReleaseRatio = \frac{ModelProtein_{Output}}{ModelProtein_{Capture}} x100 \tag{6.2}$$

The desorption/release of avidin-FITC proteins was taken place with water wash which was employed both at 25 °C and 37 °C to demonstrate protein release alteration at room temperature and body temperature. After injecting avidin-FITC into the microchannels, the water was introduced to microfluidic chips to extract the desorbed proteins from the microfluidic chips for 15 minutes, both at 25 °C and 37 °C. The avidin-FITC has a characteristic of time-dependent fluorescent photostability; hence we kept the desorption/release time for 15 minutes [172]. To snapshot fluorescent ratios in the microfluidics, the chips were adjusted under the fluorescent microscope, and the microchannels images were snapped (i) before avidin-FITC protein binding (bare surface, different shapes of p(NIPAAm)@SiO$_2$ modified microchannels), (ii) after protein binding, and after 15 minutes wash at (iii) 25 °C and (iv) 37 °C. The microfluidic chips were visualized under the fluorescence microscope (Upright fluorescence microscope, Zeiss). Using the open-source software "Fiji - ImageJ Wiki", green light intensity (captured and released model protein) analysis was performed on the images taken for the aforementioned three cases by correlating raw data and normalized green light intensity.

6.3 RESULTS and DISCUSSION

6.3.1 Characterization of BSA Model Protein Adsorption and Desorption

To analyze the capture yield of the three different shapes (peanut, square, and oval) of p(NIPAAm)@SiO_2 particles-modified microfluidic chips, BSA protein was adsorbed through the microchannels. Quantifying the capture yield of three designs revealed that the peanut-shaped p(NIPAAm)@SiO_2 particles-integrated chip had the highest capture performance in the conditions of incubation and no-incubation (**Figure 6.2**). As depicted in BET analysis **(Chapter 3-section 3.3)** the peanut-shaped particles have a higher surface area than those of square and oval shapes; hence peanut shapes of p(NIPAAm)@SiO_2 particles adsorbed/captured more BSA protein than the other shapes. On the other hand, oval-shaped p(NIPAAm)@SiO_2 particles provided higher adsorption/capture values than square-shaped ones. Analyzing the capture results with incubation revealed that peanut, square, and oval shapes of p(NIPAAm)@SiO_2 particles modified microfluidic chips have capture yields of 74.0% ± 3.0%, 62.7% ± 6.7%, and 72.7% ± 8.67%, respectively However, while performing the experiment in the flow condition (without the incubation), the capture yields dropped rapidly to 54.4% ± 1.8%, 48.4% ± 3.0%, and 53.4% ± 1.6%, respectively. These results revealed the synergistic effects of different shapes, such that the high surface area of the peanut-shaped enabled high hydrophilic interactions compared to other shapes, and provided higher capture efficiency, especially in the incubated period.

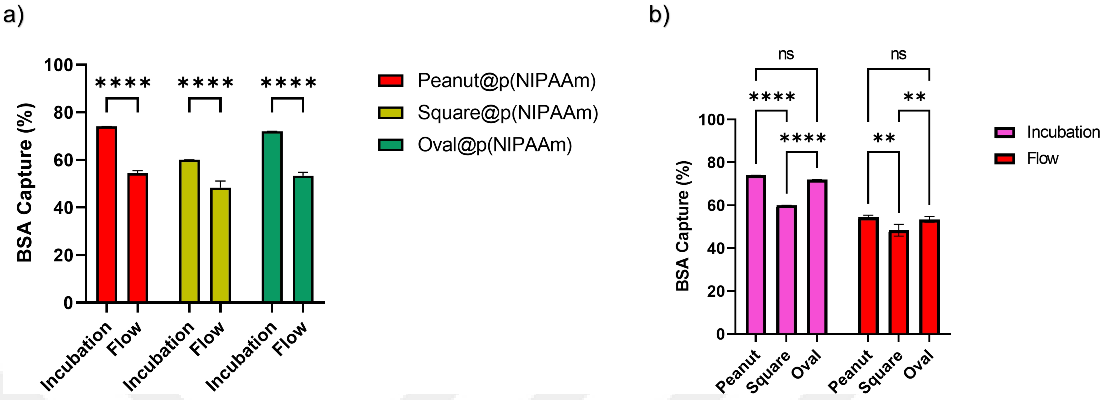

Figure 6.2: Capture efficiencies of BSA protein are presented for peanut, square, and oval p(NIPAAm)@SiO_2 particles which are immobilized on the microfluidic chips while evaluating incubation and flow (without incubation) processes. **a)** Each specific type of shape was individually compared depending on incubation and flow conditions, the data is analyzed by performing a non-parametric two-way ANOVA statistical analysis, the statistical difference is found as ****$p<0.0001$. **b)** Incubation and flow conditions were analyzed depending on shape of particles, the data is analyzed by performing a non-parametric two-way ANOVA statistical analysis, the statistical difference is found as non-significant, **$p<0.006$, and ****$p<0.0001$. "ns" stands for non-significant. Error bars stand for standard deviations ($n = 3$).

The release efficiency of different shapes of p(NIPAAm)@SiO_2 particles modified microfluidic chips was analyzed via time-dependent desorption of BSA protein throughout the microchannels. The cumulative release of BSA protein increased for each shape of particles throughout the time (**Figure 6.3**). Within an hour, peanut, square, and oval shapes provided 26.25% ± 0.67%, 18.10% ± 0.18%, and 20.60% ± 0.28%. Within 2 hours, the cumulative release of BSA was found as 27.15% ± 1.62%, 19.31% ± 1.55%, and 23.16% ± 2.11%. Within 4 hours, the release was determined as 28.05% ± 0.44%, 21.45% ± 0.20%, and 23.55% ± 1.19%. Within 8 hours, the cumulative release of BSA was revealed as 30.20% ± 0.09%, 24.60% ± 0.99%, and 25.20% ± 0.93%. Clearly, larger surface area provided higher cumulative release of BSA, which was observed in the peanut-shaped particles on the chip. Furthermore, these results confirmed that the highest release was observed in the 1st hour of desorption process due to the burst effect of the streamline at the initial stage of release [173]. Lastly, it was also proved that the shift from hydrophilic to hydrophobic phase enabled the blockage of hydrophilic interaction between BSA and p(NIPAAm)@SiO_2 particles, and therefore, that proteins were released from the microchannels.

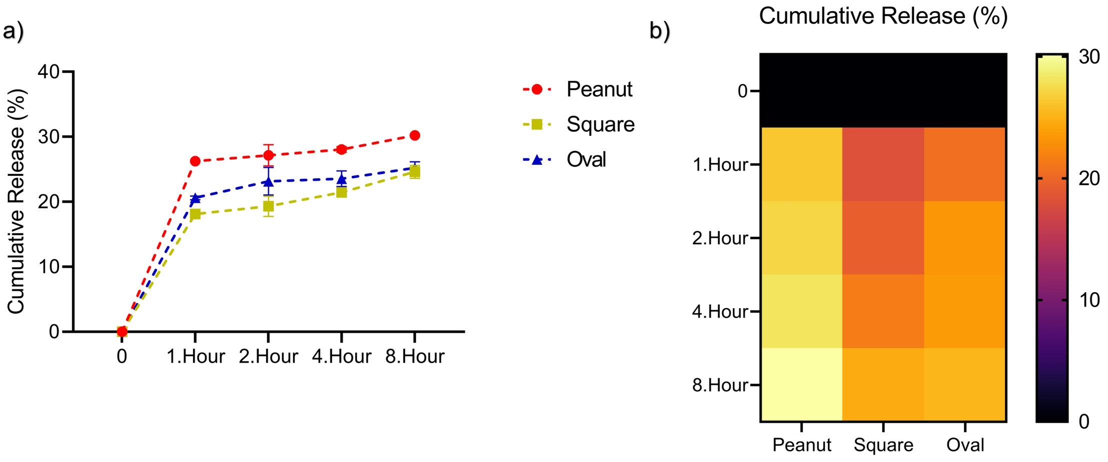

Figure 6.3: Cumulative release efficiencies are presented for peanut, square, and oval p(NIPAAm)@SiO_2 particles modified microfluidic chips. **a)** Time-dependent release of BSA and **b)** overall visualized result are depicted. The data is analyzed by performing a non-parametric two-way ANOVA statistical analysis, the statistical difference is found as $p<0.0001$. Error bars are standard deviations (n = 3).

6.3.2 Characterization of avidin-FITC Model Protein Adsorption and Desoprtion

The adsorption & desorption of avidin-FITC proteins was visualized using a fluorescence microscope. These fluorescent images for the experiments of three different shapes (peanut, square, and oval) of p(NIPAAm)@SiO_2 particles were depicted in (**Figure 6.4**). After the modification of different shapes of p(NIPAAm)@SiO_2 particles, the first image was taken from microchannels (**Figure 6.4a**), and later, 150 nM of avidin-FITC was applied to the chips (**Figure 6.4b**), and new images was recorded. After washing the platform with water at 25 °C (Figure 54c) and 37 °C (**Figure 6.4d**), the third images were collected. Finally, all of the images were assembled and analyzed through a green bar scale (RGB, 0-255) (**Figure 6.4e**). The fluorescent results revealed that the green color intensity was the highest on the step of (i) adsorption of avidin-FITC, which was followed by (ii) desorption of avidin-FITC at 25 °C and (iii) at 37 °C (**Figure 6.5**).

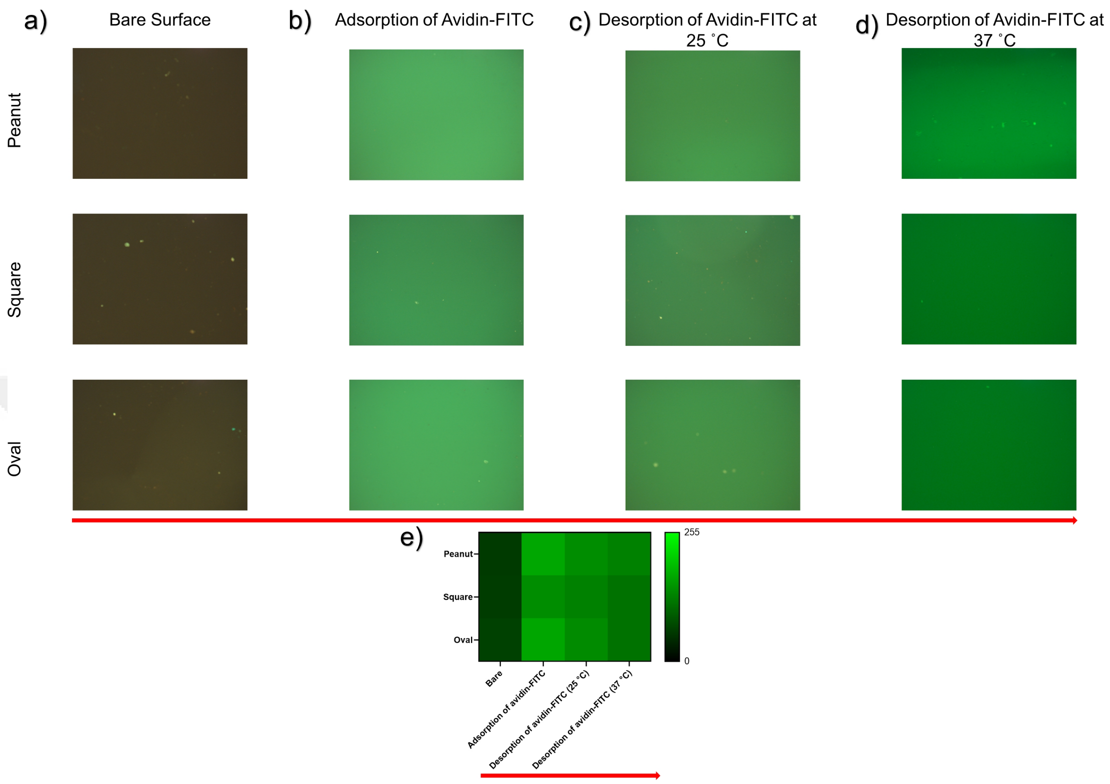

Figure 6.4: Adsorption and desorption images of avidin-FITC molecules are presented for peanut, square, and oval shapes of p(NIPAAm)@SiO_2 particles modified microfluidic chips. **a)** Bare surface, **b)** adsorption and **c)** desorption of avidin-FITC at 25 °C and **d)** 37 °C, and **e)** overall fluorescence result are shown.

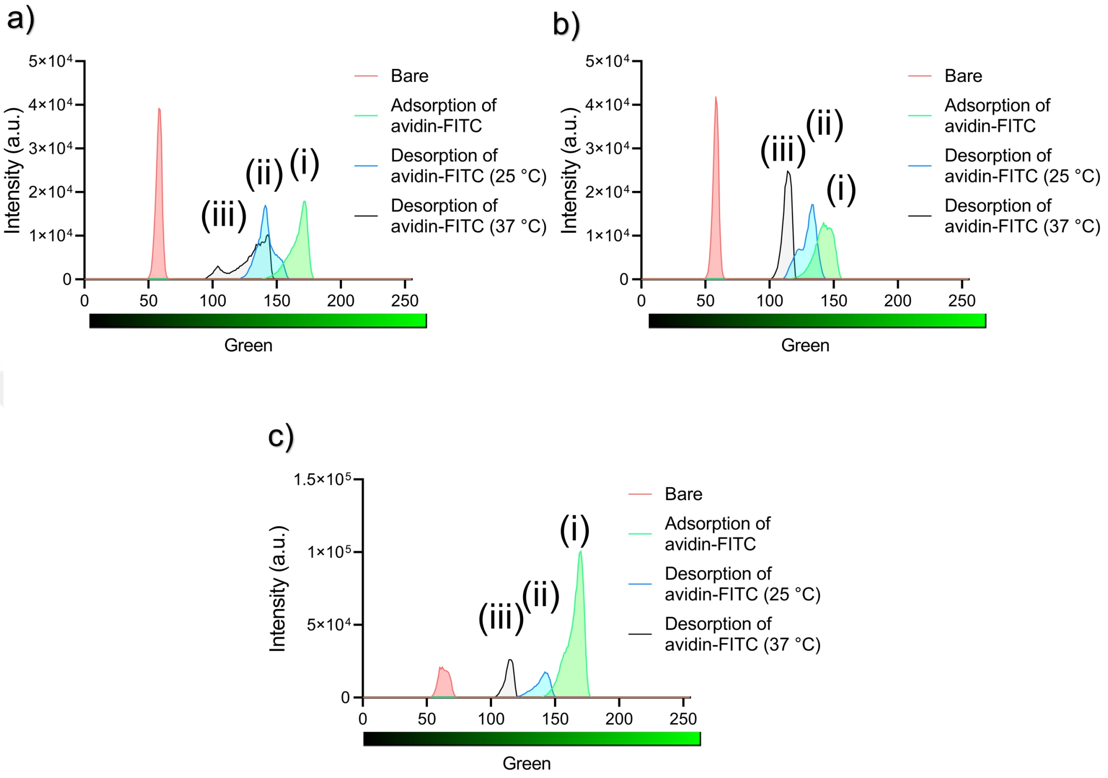

Figure 6.5: Adsorption and desorption of avidin-FITC molecules in **a)** peanut, **b)** square, **c)** oval shapes of p(NIPAAm)@SiO_2 particles modified microfluidic chips are depicted. (i) Adsorption of avidin-FITC, (ii) desorption at 25 °C, and (iii) desorption at 37 °C are represented.

When the green light mean intensity data was normalized and correlated to 0-1, it was observed that the adsorption of peanut, square, and oval shapes was found as 0.74, 0.12, and 0.70, respectively (**Figure 6.6a**). Moreover, their desorption at 25 °C resulted in 0.77, 0.13, and 0.65 for peanut, square, and oval shapes, respectively (**Figure 6.6b**). Lastly, their desorption at 37 °C were 0.87, 0.27, and 0.29 for peanut, square, and oval shapes, respectively (**Figure 6.6c**).

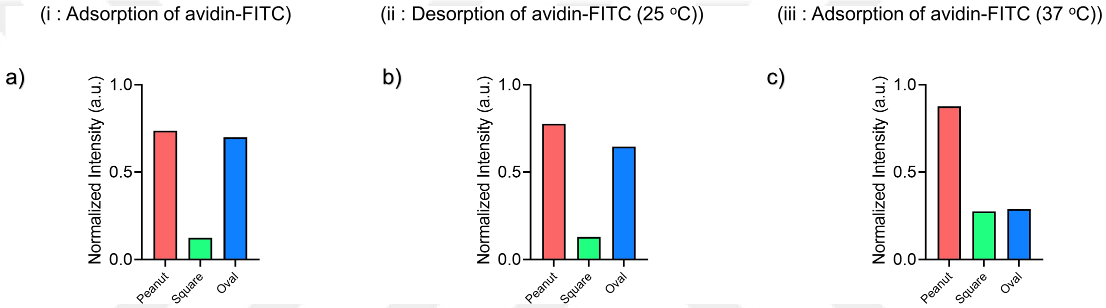

Figure 6.6: Normalized fluorescence data of avidin-FITC studies is compared for peanut, square, and oval shapes of p(NIPAAm)@SiO_2 particles modified microfluidic chips. **a)** (i : adsorption of avidin-FITC) **b)** (ii :desorption of avidin-FITC at 25 °C, and **c)** (iii :desorption of avidin-FITC at 37 °C).

Additionally, the adsorption and desorption rates for peanut, square and oval shapes of particles integrated microfluidic platforms were correlated individually. In each type of shape, adsorption of avidin-FITC provided more green light intensity (**Figure 6.7**). Similar to BSA experiments, these results showed that the peanut shape of particles provided a higher adsorption effect than those of other conditions, and the release of avidin-FITC at 37 °C enabled a higher release efficiency than that of 25 °C.

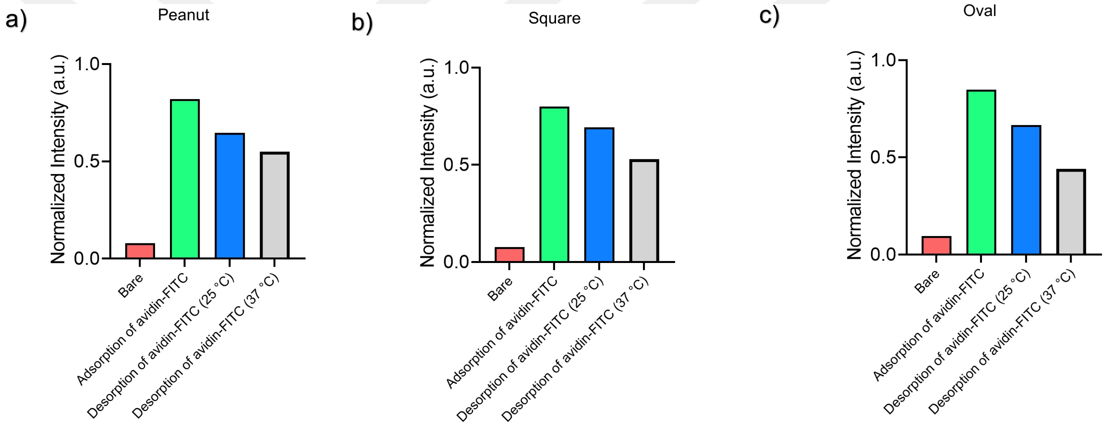

Figure 6.7: Overall normalized fluorescent data of avidin-FITC studies is compared for bare surfaces, adsorption of avidin-FITC, desorption at 25 °C, and desorption at 37 °C for **a)** peanut, **b)** square, and **c)** oval shapes of particles.

6.4 CONCLUSION

In summary, we have shown temperature-sensitivity property of different-shaped p(NIPAAm)@SiO_2 particles on the chip, and examined adsorption & desorption of model proteins to evaluate these features. Not only adsorbing proteins, but also releasing/desorbing them with high efficiency, particularly at body temperature (37 °C), demonstrated the phase alterations from hydrophobic to hydrophilic. This strategy also has enabled the controlled adsorption & desorption rate and the particle shape was also one of the striking parameters in this manner. Therefore, we here demonstrated a proof-of-concept study revealing temperature-induced phase transition on the particles that could also lead to protein release and isolation. Therefore, this smart platform is a strong candidate for the effective capture and release of CTCs, thereby we continued with this chip's experimental design and parameters for further isolation of cancer cells.

Chapter 7

CELL CULTURE, TOXICITY, and VIABILITY EXPERIMENTS

7.1 INTRODUCTION: Cancer Cells and Biomarker Types

CTCs and their 3-100 cells clusters identified as CTM [16, 17] can provide real-time information and present heterogeneity. Among all of the cancer cell types, MCF-7 cell line is the most examined human breast cancer cell type in cancer research, and the investigations from this cell type have an impact upon patient outcomes and breast cancer research [174]. MCF-7 cells have a number of biomarkers including estrogen receptor (ER), CD45, human epidermal growth factor receptor (HER), progesterone receptor (PR), and CK which are already being employed in the clinical applications, but variations among specific patients hinder effective treatment and the diagnosis of breast cancer [175]. In particular, a type I glycosylated transmembrane protein-epithelial cell adhesion molecule (EpCAM) is overexpressed in several neoplasms, including glioma, hepatocellular carcinoma, colorectal cancer, and breast cancer. Because of the fact that EpCAM has been associated with cancer prognosis and progression of breast cancer cells (MCF-7), it is used as a diagnostic marker for a myriad of diseases. In this dissertation and chapter, we also used anti-EpCAM antibodies in order to capture MCF-7 circulating tumor cells since they have high EpCAM expression. For assessing the capture and release capability of our platform, MCF-7 cells were used as a model cell line, and these cells were cultured and proliferated while maintaining them in appropriate conditions. Subsequently, before applying them to the microfluidic capture platform, MCF-7 cells were dissociated from flasks. The cytotoxicity of SiO_2 and p(NIPAAm)@SiO_2 particles, which were employed into microfluidic channels, was tested via 3-(4,5-dimethylthiazol-2-yl)-2,5-diphenyltetrazolium bromide assay (MTT, Sigma Aldrich), live/dead viability/cytotoxicity (ThermoFisher) kit and long-term culturing of MCF-7 cells with SiO_2 and p(NIPAAm)@SiO_2 particles.

7.2 MATERIALS and METHODS: MCF-7 Culture and Analysis, Bicompability of Particles

In this part of the dissertation, we tested the cytotoxicity activities of SiO_2 and p(NIPAAm)@SiO_2 particles against MCF-7 cells. Recently, a myriad of studies were reported on the toxic effects of versatile silica and other materials [176, 177]. It was clearly mentioned that the silica particles have a decent biocompatibility on different cells, especially on MCF-7 cells and less than 100 µg/mL of silica particles has no cytotoxic effect on cancer cells [176, 177]. Furthermore, the biological toxicity of NIPAAm polymer was also investigated in a capture and release platform through live/dead staining assay; for instance, Wang et. al. treated NIPAAm hydrogel coatings with MCF-7 cells and observed 96.8% and 98.7% viability respectively for before capture and after release [122]. Finally, the cytotoxic effect of p(NIPAAm)-integrated silica particles was tested against MCF-7 cell lines via MTT assay analysis [116]. Either silica particles or p(NIPAAm)-integrated silica particles showed no toxic effect against the MCF-7 cells. Here, we worked with MCF-7 cells which have high EpCAM expression and tested them in different conditions for observing the biocompatibility of our platform.

7.2.1 Cell Culture Experiments

MCF-7 breast cancer cells were used as model cancer cells in order to investigate the capture and release yields of the microfluidic chip. MCF-7 cells are EpCAM-positive, and they were cultured with DMEM/F-12 (500 mL) (Dulbecco's Modified Eagle's Medium/Nutrient Mixture F-12, Biowest with L-glutamine 1%, (5mL) and sodium bicarbonate, without HEPES, liquid, sterile-filtered) containing Fetal Bovine Serum (FBS, 10%, 50 mL) and Penicillin-Streptomycin (100 µg/ml, 1%, 5 mL). Cells were cultured in 80% of humidified cell culture incubator at 37 °C along with 5% of CO_2. Once the cells reached to 85-90% confluency in the flasks, the cells were treated with 0.25% of trypsin-0.02% of ethylenediaminetetraacetic acid (EDTA) for 5 minutes at 37 °C in order to extract cells from the flask. The hood to be used to passage the cells was first sterilized through UV light for 15 minutes. After the UV light process was over, the cell culture hood area was cleaned with ethanol. After extracting cells from the flask, hemocytometer was used to calculate the cell number by using Trypan Blue solution (0.4%) (10 µL of trypan blue dye + 10 µL of the extracted MCF-7 cell media). Once all the logistics were completed, the confluency and number of MCF-7 cells were evaluated using a microscope (Zeiss Inverted Fluorescence Microscope). The following **Equation 7.1** states the way for counting for dead and live cells:

$$TotalCellNumber = CountedCellNumberxDilutionFactorxSampleVolumex10^4 \tag{7.1}$$

7.2.2 Live/Dead Analysis of MCF-7 Cells

To assess the viability of MCF-7 cells before treating them with particles, Live/Dead staining method was employed as a control group [178]. For this purpose, as previously stated in **Chapter 7-section 2.1**, MCF-7 cells were extracted from a cell culture flask via trypsin-EDTA solution. Afterwards, the extracted MCF-7 containing medium was added into a falcon tube, and then, centrifuged at 8600 g (6000 rpm) for 5 minutes at room temperature, thereby precipitating MCF-7 cells before applying the medium to the chip. After the centrifugation, since the precipitation contains MCF-7 cells, the supernatant was removed and precipitation was diluted with 1 mL of PBS and transferred to a new tube and used in the experiment. The Live/Dead (ThermoFisher) reagent containing 5 µL of calcein AM stain and 20 µL of ethidium homodimer-1 was diluted with 1 mL of PBS. All of the solution was added to MCF-7 cells containing Eppendorf tube. Calcein-AM emits green fluorescence and stains viable cells, while ethidium homodimer-1 emits red fluorescence and stains dead cells. Excitation/emission values for calcein-AM are 494/517 nm with a FITC or GFP filter set, while it is 528/617 nm for ethidium homodimer-1 with an RFP filter set. The solution was incubated for 30 minutes at 25 °C at a dark place. Afterwards, the stained MCF-7 cells were evaluated using a microscope (Zeiss Inverted Fluorescence Microscope). According to the Live/Dead assay staining method, the following **Equation 7.2** states how the evaluating viability of MCF-7 cells was performed.

$$CellViability = \frac{LiveCells_{Green}}{LiveCells_{Green} + DeadCells_{Red}} x100 \tag{7.2}$$

7.2.3 Cytotoxicity Studies

The cytotoxicity of the SiO_2 and p(NIPAAm)@SiO_2 particles against MCF-7 cells were evaluated by long-term culturing cells with SiO_2 and p(NIPAAm)@SiO_2 particles, MTT assay, and Live/Dead viability/cytotoxicity analysis. At the first glance, long-term culturing of MCF-7 cells with SiO_2 and p(NIPAAm)@SiO_2 particles was performed for 7 days. Before seeding cells, SiO_2 and p(NIPAAm)@SiO_2 particles were sterilized via a dry heat sterilization method, and the particles were heated in a standard oven for an hour at 180 °C [179]. Afterwards, MCF-7 cells were treated with 100 µg/mL of SiO_2 and p(NIPAAm)@SiO_2 in separate cell culture flasks. As previously stated in **Chapter 7-section 2.1**, the same cell culture ingredients and conditions were also applied for this long-term cell culture cytotoxicity analysis. The cells treated particles were left in 80% of humidified cell culturing incubator at 37 °C with 5% of CO_2 for 7 days in order to observe whether any potential cytotoxic effects occur during the culturing. The cell analyses (morphological and physical variations) were observed using Zeiss Inverted Fluorescence Microscope.

Second, another cytotoxicity investigation was performed via the MTT assay analysis method. Subsequently, as previously stated in **Chapter 7-section 2.1**, MCF-7 cells were extracted from cell culture flasks. After that, for the short-term (3-day) MTT analysis, the cell density was evaluated via hemocytometry, and MCF-7 cells with 200 µL of DMEM were seeded onto 96-well plates, in which the number of cells per well was 3000, and incubated for 24 h to allow cell attachment into the wells. After 24 hours, DMEM was withdrawn from each well plate via micropipette, and the treated wells were washed with PBS 2 times, followed by discarding PBS solution from the wells. After that, fresh DMEM (200 μL) was separately added to 96-well plates, which were treated with (i) SiO_2 (100 µg/mL) and (ii) p(NIPAAm)@SiO_2 particles (100 µg/mL). Moreover, we designed additional experimental sets for MTT analyses: (iii) DMEM with MCF-7 cells, (iv) DMEM without MCF-7 cells, (v) SiO_2, and (vi) p(NIPAAm)@SiO_2 particles treated DMEM without MCF-7 cells, and blank (DMSO). After 24 hours, DMEM was withdrawn from each well via a micropipette and washed with PBS and DMEM two times, followed by discarding solutions. After that, 10 μL of MTT solution (5 mg/ml in PBS) was replaced in each well and then, incubated for an additional 5 hours with 90 μL of DMEM. Upon discarding the MTT solution, each well was washed with PBS, followed by discarding PBS solution. Afterward, in the cell culture hood, the purple formazan crystals were dissolved in 100 μL of DMSO and added to each well with a blank DMSO, and after 45 seconds of incubation, the absorbance of the samples was recorded at 570 nm with a multi-well plate reader. The MCF-7 cells in the DMEM (no particle treatement) were used as a control. All experiments were performed with three replicates. Furthermore, these procedures were repeated for long-term (7-day) MTT analysis. For this case, the short-term investigation parameters that we discussed above, were performed again. Instead of 1 day, the specimens have been emplaced to cell culture hood for 6 days more, after incubation of 1 day. After 7 days, MTT assay was performed to the wells, and the absorbance values of these samples were recorded at 570 nm with three replicates. The following **Equation 7.3** states how the evaluating viability of particles treated MCF-7 cells was performed:

$$CellViability = \frac{OpticalAbsorbanceValueofSample}{OpticalAbsorbanceValueofControl}x100 \tag{7.3}$$

7.3 RESULTS and DISCUSSION

7.3.1 Cell Culture Results

In each culturing period, cells were grown properly, and they had more confluency in long-term culturing. On the 4^{th} day of the culturing period (**Figure 7.1a**), cells were almost 50% of confluent, whereas, on the 7^{th} day of the culturing (**Figure 7.1b**), it was around 85-90% confluent. After imaging cells on the microscope, on the 7^{th} day, in order to dissociate cells from the flasks. The medium in the cell flask was drawn and discarded using a pipettor. Cell culture flasks and cells were washed with 2 mL of PBS, followed by discarding PBS solution. Once this step was repeated two times, 0.25% of Trypsin-EDTA (1 mL) was applied to the cells. The flask was then kept in the incubator (37 °C) for 5 minutes, and 3 mL of medium was applied to the flask to neutralize Trypsin-EDTA effect over the cells. Finally, we added 3 mL of a new medium to 1 mL of cell from the flask (1:4 cell/media dilution), and the cells were then transferred into new flasks. After that, new flasks were placed in an incubator at 37 °C under a 5% of CO_2 atmosphere.

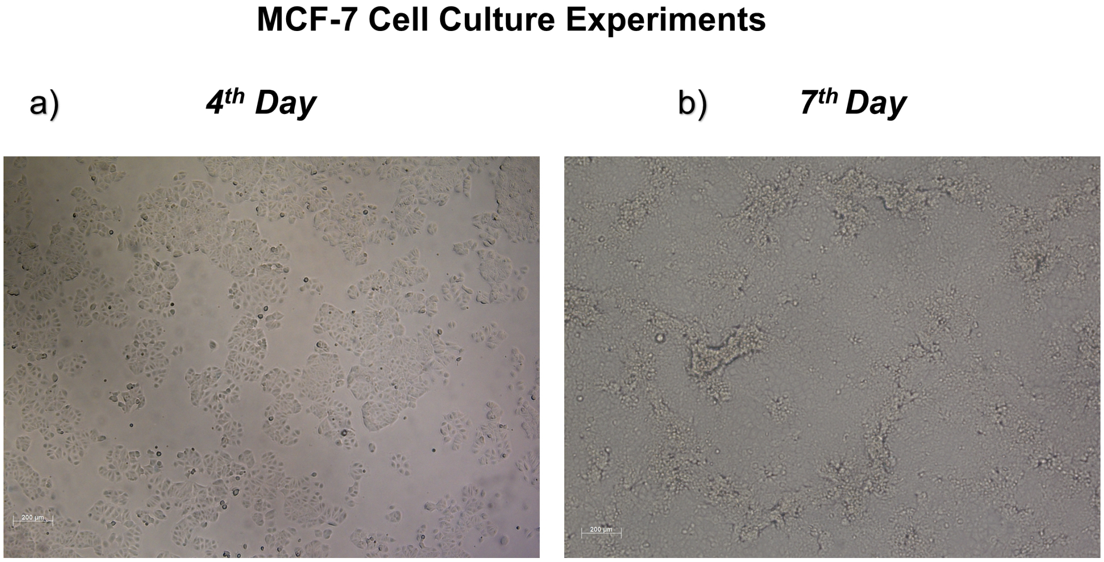

Figure 7.1: MCF-7 cell culture experiments are presented. The confluency results on **a)** 4^{th} day and **b)** 7^{th} day are imaged.

On the course of the passaging process, some cells were used for counting via the hemocytometry method. Briefly, 10 µL of cells were added into an Eppendorf tube, and 10 µL of Trypan Blue dye was added to this tube. While this dye stained dead cells in blue color, it did not stain live cells, and live cells thus appear transparent (white) under the microscope (**Figure 7.2**).

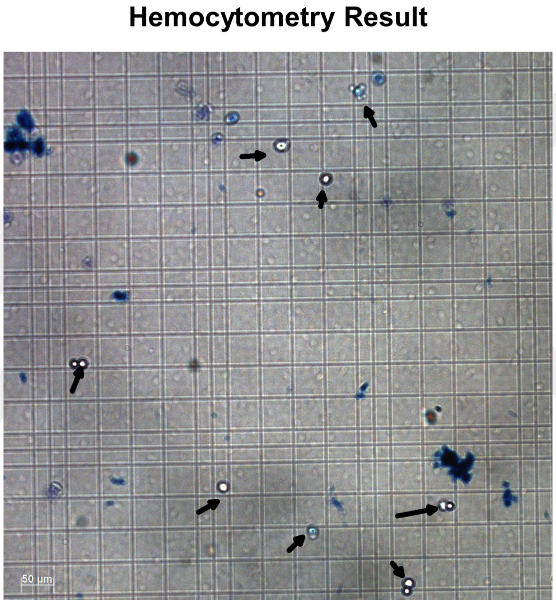

Figure 7.2: Hemocytometry results of MCF-7 cell culture experiments are presented.

The hemocytometry result shows the viability rates of cells according to the counts made after certain passages. To assess the capture efficiency of the microfluidic chip, we applied two concentration values of MCF-7 cells for further experiments. The concentrations were 60.000 cells/mL (for control experiment), 75.000 cells/mL and 150.000 cells/ml prepared in PBS.

7.3.2 Cytotoxicity Analysis Results

Thermoresponsive p(NIPAAm)-based biomaterials have been widely used for different biomedical applications including discriminating cancer cells, protein delivery, and cell sheets [180]. Hence, p(NIPAAm)-integrated silica particles are expected to display biocompatibility [171]. Even if the decreased temperature might cause a cytotoxicity risk, we are increasing the temperature of platform to release CTCs in this CTCs isolation platform [181]. For this purpose, we cultured MCF-7 cells with SiO_2 and p(NIPAAm)@SiO_2 particles for 7 days as the long-term culturing. The confluency of MCF-7 cells was evaluated using a microscope (Zeiss Inverted Fluorescence Microscope), and we observed the confluency of cells at the end of 7 days (**Figure 7.3**). On the 4^{th} day of the cell culture, p(NIPAAm)@SiO_2 applied MCF-7 cells were more confluent than those of SiO_2, whereas on the 7^{th} day of the cell culturing, both flasks were more confluent than 4^{th} day results and the confluency was around 90%. Furthermore, p(NIPAAm)@SiO_2 enabled more confluency of cells than the condition under SiO_2 on the 7^{th} day.

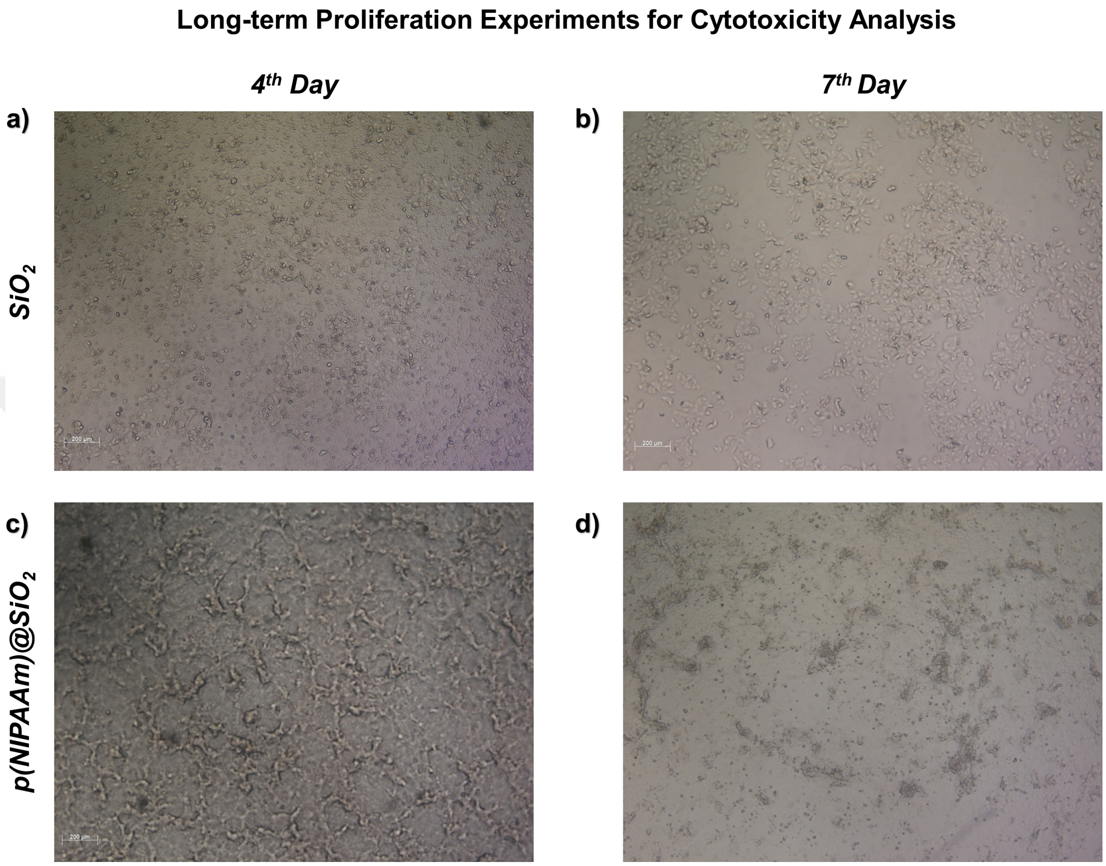

Figure 7.3: During long-term culture, MCF-7 cells are imaged for cytotoxicity analysis. The cell confluency images are presented for cultures with $\mathrm{SiO_2}$ **a)** on the 4^{th} day and **b)** 7^{th} day. The cell confluency images are presented for cultures with p(NIPAAm)$\mathrm{SiO_2}$ **c)** on the 4^{th} day and **d)** 7^{th} day.

Indeed, MTT assays demonstrated that p(NIPAAm)-based materials were effectively non-toxic to MCF-7 cells (cell viability $\geq 80\%$) up to a tested concentration of 200 µg/mL of these materials [171]. Particularly, in our study, the preparation of particles treated with MCF-7 cells were carried out under a maximum concentration of 100 µg/mL. The MTT toxicity analysis for (i) SiO_2 (100 µg/mL) and (ii) p(NIPAAm)@SiO_2 particles (100 µg/mL) with MCF-7 cells, (iii) DMEM with MCF-7 cells, (iv) DMEM without MCF-7 cells, (v) SiO_2, (100 µg/mL) and (vi) p(NIPAAm)@SiO_2 (100 µg/mL) particles treated DMEM without MCF-7 cells were presented in **Figure 7.4**. The results showed high biocompatibility for both (i) SiO_2 and (ii) p(NIPAAm)@SiO_2. Investigations showed that both particles exhibited no obvious toxic effect against MCF-7 cells, whereas cells grown with p(NIPAAm)@SiO_2 (111.04 ± 2.59%) showed more biocompatibility compared to those with SiO_2 (109.06 ± 3.68%) for the short-term (3-day) analysis (**Figure 7.4a**). In the long-term (7-day) MTT analysis, again both particles exhibited no obvious toxic effect against MCF-7 cells, whereas cells grown with p(NIPAAm)@SiO_2 (101.48 ± 4.60%) had more biocompatibility than those with SiO_2 (97.49 ± 3.02%) (**Figure 7.4b**). It was worthy to note that the viability rate was higher in SiO_2 and p(NIPAAm)@SiO_2 than only the MCF-7 group (control) and it can be expectable for MTT analysis [182]. Therefore, these particles can be expected not to be harmful or toxic for MCF-7 cells.

On the other hand, cell viability analysis for (v) SiO_2, and (vi) p(NIPAAm)@SiO_2 particles treated DMEM without MCF-7 cells showed controversial results compared to (i) SiO_2 and (ii) p(NIPAAm)@SiO_2 particles with MCF-7 cells in terms of short and long term analysis. The cell viability results were found as (v) SiO_2 (14.97 ± 1.93%) and p(NIPAAm)@SiO_2 (13.74 ± 1.79%) for the short-term (3-day) analysis (**Figure 7.4a**). In the long-term (7-day) MTT analysis, cell viabilities revealed as SiO_2 (15.95 ± 1.37%) and p(NIPAAm)@SiO_2 (16.10 ± 2.03%) (**Figure 7.4b**). These results show that there are minor differences in cell viability between short-term (3-day) and long-term (7-day) analysis of (v) SiO_2, and (vi) p(NIPAAm)@SiO_2 particles treated DMEM without MCF-7 cells. Hence, these particles can preserve themselves in both short-term and long-term MTT investigations against any contaminations or undesired cell growth.

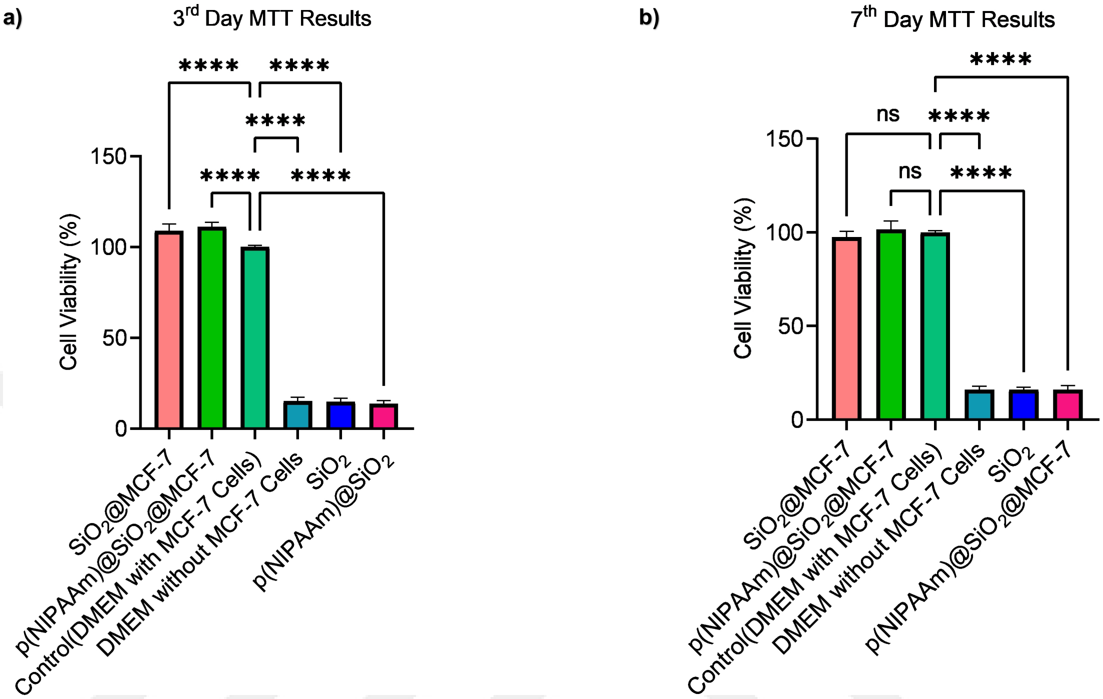

Figure 7.4: MTT assay viability shows the results of MCF-7 cells treated with; (i) SiO_2, (ii) p(NIPAAm)@SiO_2, (iii) DMEM; and (iv) DMEM, (v) SiO_2, and (vi) p(NIPAAm)@SiO_2 without MCF-7 cells in the durations of **a)** 3 days and **b)** 7 days. MCF-7 cells incubated with standard DMEM culture media are defined as the control. The data is analyzed by performing an ordinary one-way ANOVA statistical analysis, and the statistical difference is found as non-significant, ****$p<0.0001$. "ns" stands for non-significant. Error bars stand for standard deviations (n = 3).

Through Live/Dead assay, we also checked the cell viability of MCF-7 before the capture process in this chapter (control). In addition, the investigation of cell viability after cell release from the chip will be covered in **Chapter 8**. To investigate cell viability before the capture, we applied a drop of the Live/Dead (ThermoFisher) reagent and MCF-7 containing solution (5 μL), which was described in **Chapter 7-section 2.2**, into a glass slide and covered with a glass slip. Afterwards, we took images in order to evaluate the cell viability using a fluorescence microscope (Zeiss Inverted Fluorescence Microscope) and counted them manually. Cell viability before the capture process was calculated as 82.33% ± 11.09% (**Figure 7.5**).

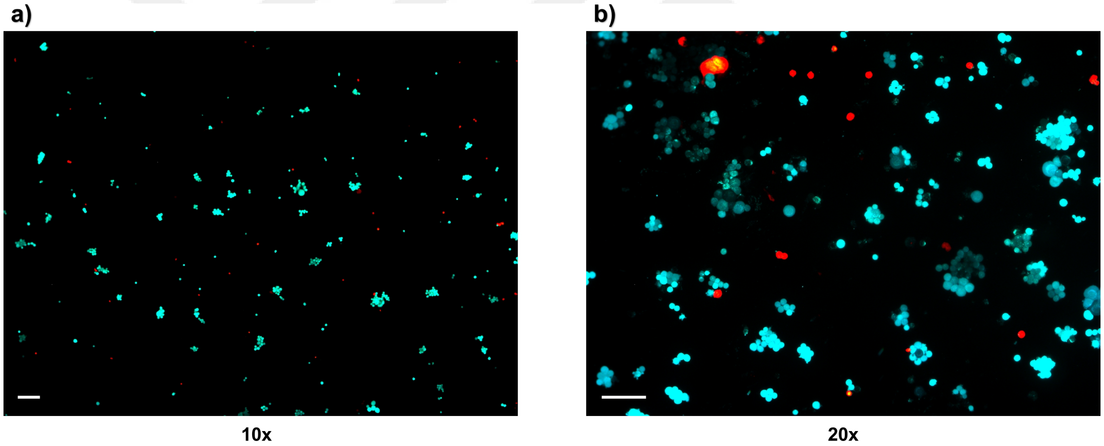

Figure 7.5: Live/Dead assay is demonstrated for MCF-7 cells before the capture experiments. Green cells represent live whereas red cells **a)** 10x and **b)** 20x are dead. Scale bar = 100 μm.

7.4 CONCLUSION

In summary, EpCAM-positive MCF-7 cancer cells were successfully cultured in a cell culture incubator at 37 °C under 5% of CO_2 atmosphere. Once the cells reached to 85-90% of confluency, they were dissociated from flasks to use for the microfluidic chips. Furthermore, we have tested the cytotoxicity activities of SiO_2 and p(NIPAAm)@SiO_2 particles against MCF-7 cells in different conditions. For this purpose, the cytotoxicity of the SiO_2 and p(NIPAAm)@SiO_2 particles against MCF-7 cells were analyzed for long-term culturing with SiO_2 and p(NIPAAm)@SiO_2 particles, MTT assay analysis, and Live/Dead viability/cytotoxicity methods. As a result, we did not observe any toxic effects of SiO_2 and p(NIPAAm)@SiO_2 particles against MCF-7 cells in terms of culturing and proliferating cancer cells with these particles for 7 days of culturing according to the aforementioned analyses. Particularly, p(NIPAAm)@SiO_2 particles that we integrated into the microfluidic platform exhibited higher cell viability than the cells treated with SiO_2 particles. Hence, we decided to employ 100 µg/mL of particle concentration for further analysis in the next chapter.

Chapter 8

CAPTURE and RELEASE of CANCER CELLS via DIFFERENT-SHAPED SMART POLYMERS/MATERIALS in MICROFLUIDICS

8.1 INTRODUCTION: Significance of Specific Capture and Release

So far, we have elaborated on fundamental aspects of CTCs isolation through discussing the challenges in detecting CTCs; providing insights on novel solutions; and introducing our method, and experimental steps. In this part of thesis, we expanded this view to employing MCF-7 cells into our microfluidic platform for cell capture and release regard. Once CTCs are captured, it is essential to comprehend their cell heterogeneity and origin to deploy the most effective therapy. Therefore, their release/isolation from a microfluidic chip is a strong mainstay in this manner. Particularizing this focus, the release method of cancer cells would provide phenotype identification, culture expansion, and molecular analysis in the near future. Hereinto, surface chemistry is the key aspect that enables to control the release aspect. During this action, cancer cells may have held some contaminations or structural damages that could possibly hinder the studies after their release. Keeping performance yield as high as possible would enable accurate analysis of CTCs in the future. For example, in the circumstance of low intact cell viability, the impurity of cancer cells hinders true positive signals [47]. To tackle these challenges, we here proposed a solution by harmonizing different shapes (peanut, square, and oval) of smart-polymers (p(NIPAAm)@SiO_2) and specific anti-EPCAM antibodies into short-distance modification. We aim to efficiently capture MCF-7 human breast cancer cells (high-EpCAM-expression) cells on-a-chip, and then, release them through the alterations in the 3-D structure of smart-polymer caused by temperature changes.

8.2 Materials and Methods: Capture and Release of MCF-7 Cells

In previous chapters, we prepared different-shaped p(NIPAAm)@SiO_2 particles-immobilized on microfluidic chips. Here, we decorated anti-EpCAM antibodies on the particle surface due to the abundancy of EpCAM biomarkers on the membrane of MCF-7 cells [1]. In this case, the proper orientation of anti-EpCAM antibodies were enabled with protein G since the Fc portion of antibodies have affinity to this protein. Afterwards, 1% of BSA was applied to minimize any potential non-specific bindings due to the medium used in this experiment. In **Chapter 5**, we also optimized and selected the optimized length-dependent surface modification as short (3-MPS). In **Chapter 7**, we cultured and proliferated MCF-7 cell lines as a cell model in the designed microfluidic chips. We also have tested the biocompatibility of these particles (SiO_2 and p(NIPAAm)@SiO_2) and observed non-toxic effect of the p(NIPAAm)@SiO_2 particles while culturing them with cells. In this chapter of thesis, we applied MCF-7 cells into microfluidic chip, which were modified with different shapes of p(NIPAAm)@SiO_2 particles that are modified with anti-EpCAM antibodies and immobilized with a short-length linkers to the chip surface. After enabling the capture process, we change the temperature to release the cells from the chip, and consequently, evaluated their viability again after the release process.

8.2.1 Immobilizing Antibodies to the Microfluidic Chips

We initially modified the microfluidic chips with p(NIPAAm)@SiO_2 particles through a short-length modification (3-MPS), which was detailed in **Chapter 5**. Later, in order to immobilize anti-EpCAM antibodies on these particles, we initially decorated the microchannels with protein G, hence enabling the proper orientation of antibody immobilization through the Fc portion of antibodies. Here, first of all, 100 µg/mL of protein G (dispersed in PBS) was introduced at a 10 µL min^{-1} of flow rate and incubated by pausing the injection of fluid when the channels were filled with the solution at 25 °C for an hour. Second, anti-EPCAM antibodies were diluted and dispersed with PBS to adjust the concentrations to 50 µg/mL. The antibody solution was then applied to the microfluidic platforms at a 10 µL min^{-1} of flow rate and incubated by stopping the fluid injection when the channels filled with the liquid at 25 °C for an hour. After the incubation, the microfluidic chips were cleaned with PBS for 5 minutes at a flow rate of 10 µL min^{-1} to remove any unbound moieties, and therefore, the microfluidic chips were ready for the application of MCF-7 as a CTC model.

8.2.2 Capture and Release of MCF-7 Cells

MCF-7 human breast cancer cells were employed to demonstrate capture and release yields of the microfluidic chip. For extracting MCF-7 cells from cell culture flasks, passaging of the cells is needed. Before passaging cells, DMEM and 0.25% of Trypsin-EDTA (Gibco) filled falcons were kept in a water bath at 37 °C. Once the cells reached around 85-90% confluency, the extraction of cells was performed. The medium in the cell flask was drawn and discarded using a pipettor. Cell culture flasks and cells were washed and cleaned with 2 mL of PBS, followed by discarding PBS solution. After this step was repeated two times, 0.25% of Trypsin-EDTA (1 mL) was introduced onto the cells. The flask was then kept in the incubator (37 °C) for 5 minutes, and 3 mL of medium was applied to the flask to neutralize Trypsin-EDTA interferes the cell membrane if incubated for long time. Afterwards, the medium containing MCF-7 cells was added into a falcon tube, and then, centrifuged at 8600 g (6000 rpm) for 5 minutes at the room temperature, thereby precipitating MCF-7 cells before applying them to the chip. After the centrifugation, since the precipitation contains MCF-7 cells, the supernatant was extracted and precipitation was diluted by using 1 mL of PBS and transferred to a new tube and used in the capture experiments. Thereafter, MCF-7 cells were stained with Hoechst stain (2 $^{\mu}$g/mL) (Hoechst 33342, Trihydrochloride, Trihydrate, ThermoFisher) for 30 min. Hoechst dye is a type of cell-permeant nuclear counterstain that emits blue color fluorescence with 350/461 nm excitation wavelength when bound to dsDNA. The blue fluorescent signal was observed using Zeiss Inverted Fluorescence Microscope with a DAPI filter set. The images were taken from the entire surface area (152 mm^2) of the microfluidic chip.

After that, MCF-7 containing PBS solution was applied into different shapes of p(NIPAAm)@SiO_2 particles integrated microfluidic chips. The particles had already anti-EPCAM antibodies, and they are tethered via short length linkers. before sampling, we also applied 1% of BSA, and then, MCF-7 cells were introduced to the chip surface with a 10 µL min^{-1} of flow rate for 15 minutes via syringe pump, followingly incubated for an hour, and washed with PBS for 15 minutes to remove unbound MCF-7 cells. As stated in **Chapter 7-section 3.1**, we evaluated different concentrations of MCF-7 cells (60.000 cells/mL, 75.000 cells/mL and 150.000 cells/mL) in order to understand any effects over the capture efficiency due to the cell concentration. MCF-7 capture experiments in this chapter were performed for each cancer cell concentration value. After cell capture and wash, we took images (n=3) from different shapes of p(NIPAAm)@SiO_2 integrated chips in order to evaluate the capture efficiency using a fluorescence microscope (Zeiss Inverted Fluorescence Microscope) and we manually counted the captured cells. The number of captured cells within a small scale in the chip was multiplied by a ratio, defined as that the entire surface area of the chip is divided by the surface area of experimental images. The evaluation of capture efficiency was depicted as (**Equation 8.1**):

$$CaptureEfficiency = \frac{CapturedCellsinChip}{ExpectedTotalCellsinChip} x100 \tag{8.1}$$

After that, the release process was employed at 37 °C due to the phase transition ıon the particles. MCF-7 cells were released from the microfluidic platforms with a 10 µL min^{-1} of flow rate for an hour via syringe pump at 37 °C (LCST of p(NIPAAm)). Afterwards, we took images (n=3) from different shapes of p(NIPAAm)@SiO_2 integrated chips in order to evaluate the release efficiency using a fluorescence microscope (Zeiss Inverted Fluorescence Microscope) and manually counted. The number of released cells within a small scale in the chip was multiplied by a ratio, defined as that the entire surface area of the chip is divided by the surface area of experimental images. The release efficiency was defined as (**Equation 8.2**):

$$ReleaseEfficiency = \frac{CapturedCellsinChip - RemainingCellsinChip}{CapturedCellsinChip} x100 \tag{8.2}$$

8.2.3 Viability Analysis of Released Cells

After the release process, we collected the released MCF-7 cells in Eppendorf tubes. Each collected sample was centrifuged at 8600 g (6000 rpm) for 5 minutes at the room temperature, thereby precipitating the released MCF-7 cells. After the centrifugation, since the precipitation contains MCF-7 cells, supernatants were removed and precipitation was diluted with 1 mL of PBS and 900 µL of them were transferred to other Eppendorf tubes. Subsequently, the Live/Dead (ThermoFisher) reagent consisting of 5 µL of calcein AM stain and 20 µL of ethidium homodimer-1 was diluted with 1 mL of PBS, and 900 µL of it was added to 900 µL of MCF-7 cells containing Eppendorf tube (1:1 reagent/cell ratio). In the Live/Dead assay staining method, the following **Equation 8.3** states how the evaluating viability of MCF-7 cells after the release process was performed:

$$CellViability = \frac{LiveCells_{Green}}{LiveCells_{Green} + DeadCells_{Red}} x100 \tag{8.3}$$

Later on, we performed flow cytometry analysis (BD Accuri™ C6 Plus, Biosciences) in order to evaluate live/dead of MCF-7 cells before capture and after release. Flow cytometer measures certain cell parameters such as shape and size, as the cells flow in an environment of fluid stream and a single-file past an analytical laser light resource that has two specific wavelengths (488/640 nm) [183]. The analysis is mainly performed via emission detection of stained particles after applying illumination and collecting scatters. For this purpose, specific emission detectors should be used for different colors. For example, filter 1 (FL1) is mainly applied for FITC or GFP (533/30 nm) stained samples. Here, with the aiming to evaluate the viability rate of MCF-7 cells before the capture and after the release, we perform flow cytometry. For this purpose, we prepared fresh reagent solutions only containing 5 µL of calcein AM (diluted with 1 mL PBS) as a positive control, 20 µL of ethidium homodimer-1 (diluted with 1 mL PBS) as a negative control, and 5 µL of calcein AM stain and 20 µL of ethidium homodimer-1 (diluted with 1 mL PBS) as both staining sample (positively and negatively expressing particles). Afterwards, by using the released MCF-7 cells as we discussed above (remaining 100 µL of MCF-7 cells), 50 µL of MCF-7 cells containing sample were mixed with 50 µL of calcein-AM (PBS diluted) emitting green fluorescence that stains viable cells (positive control), while the remaining 50 µL of MCF-7 cells were mixed with 50 µL of ethidium homodimer-1 emitting red fluorescence that stains dead cells. Furthermore, we took 100 µL of non-stained MCF-7 cells before the capture and after release as additional control groups. Excitation/emission values for calcein-AM are 494/517 nm with a FITC or GFP filter set 1, whereas excitation/emission values are 528/617 nm for ethidium homodimer-1 with an RFP filter set 3. The stained solutions were placed and incubated for 30 minutes at 25 °C in a dark place, and then, the action was operated.

8.3 RESULTS and DISCUSSION

8.3.1 Characterization of Antibody Integration

First, short (3-MPS) linkers were separately modified to the bottom layer of the microfluidic chips (glass slides), and different shapes of p(NIPAAm)@SiO_2 were applied to these substrates. Then, anti-EpCAM antibodies (50 µg/mL) were applied to the surface after decorating them with protein G (100 µg/mL, 1 hour of incubation time), hence enabling the proper orientation of antibody immobilization through the Fc portion of antibodies. After the incubation, the sensors were simply washed with PBS to remove any unbound moieties. Afterwards, to understand any potential non-specific binding due to the medium used in this experiment, 1% of BSA was incubated for 15 minutes after the antibody immobilization step. The immobilization of particles and the surface chemistry on each step were characterized by SEM and ATR-FTIR. In SEM images, we observed better distribution of p(NIPAAm)@SiO_2 particles in the surfaces of the microchannels than the other counterparts (**Figure 8.1**). Moreover, after the decoration of antibodies, the homogeneous surfaces are not expected to see because either p(NIPAAm)@SiO_2 or anti-EpCAM antibodies are not dissolved in their solvent. Hence, observing well-distrubuted particles in the microfluidic channels is a natural result of the applying particle consisting solutions.

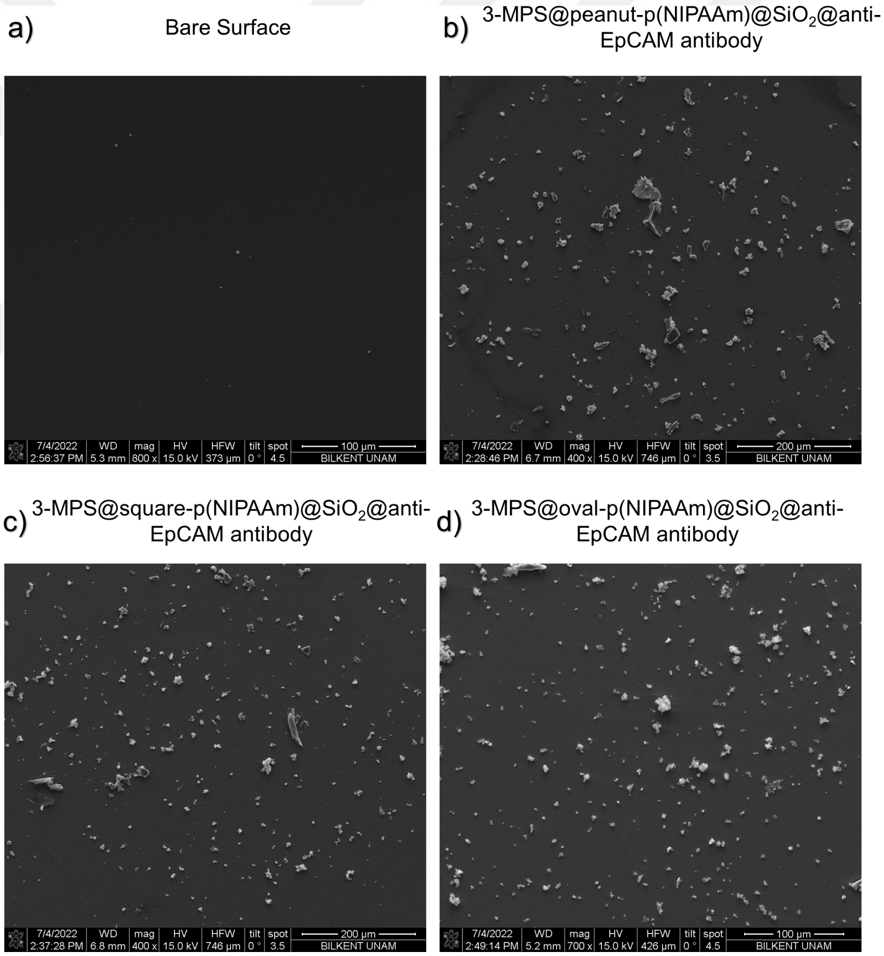

Figure 8.1: SEM images are taken for the microfluidic chips which are modified with smart materials through short linkers. Anti-EpCAM antibodies are decorated on **a)** bare surface, **b)** peanut, **c)** square, and **d)** oval shapes of p(NIPAAm)@SiO_2 particles.

In addition, ATR-FTIR analysis were performed after the application of anti-EpCAM antibodies to different-shaped p(NIPAAm)@SiO_2, which were tethered via short linkers to the chip surafce (**Figure 8.2**). The common stretchings and bending vibrations were observed at between 3300-3500 cm^{-1} (-NH), 2850-2950 cm^{-1} aliphatic groups of (C-H), 1374 cm^{-1} (C=O), and 1274 cm^{-1} carbonyl peaks of maleimide groups, while C-C/=C-H in- vibration observed at 1068 cm^{-1}. Double bond vibrations –HC=CH- were located at 1468 cm^{-1} and 1156 cm^{-1} (C-N). Symmetrical and asymmetrical peaks of the SiO_2 structure were observed stretchings around 900 cm^{-1} and 600 cm^{-1}, while the peak of 750 cm^{-1} indicates a Si-C signal. As a result of the analysis, anti-EpCAM antibody were successfully immobilized to all p(NIPAAm)@SiO_2 particles, resulting in high signal intensities.

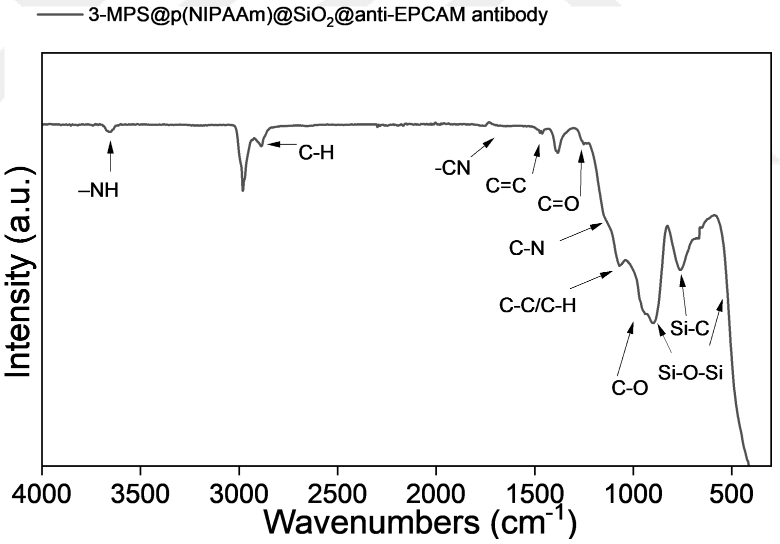

Figure 8.2: FTIR analysis presents the decoration of anti-EpCAM antibodies on short linker (3-MPS)-modified p(NIPAAm)@SiO_2 particles on the chip.

8.3.2 Analysis of Capture and Release Efficiency of MCF-7 Cells from the Microfluidic Chips

Captured cells in the microfluidic platforms were observed via the fluorescence microscope (Upright fluorescence microscope, Zeiss, Excitation = 350 nm and Emission = 461 nm). The microfluidic chips modified with peanut, square, and oval shapes of p(NIPAAm)@SiO_2 were adjusted under the fluorescent microscope, and we snapshotted them with three replicates. Using an open-source software "Fiji - ImageJ Wiki", the stained and captured MCF-7 cells, which emit blue light, were evaluated and we counted them manually.

Firstly, to test the temperature effect on MCF-7 cells release, MCF-7 cells were introduced to the chip, which was modified with peanut shape of particle as a model shape for the control experiment, with a 10 µL min^{-1} of flow rate for 15 minutes, followingly incubated for an hour, and washed with PBS for 15 minutes to remove unbound MCF-7 cells. We here used 60.000 cells/mL of MCF-7 cells As can be seen from **Figure 8.3a**, captured MCF-7 cells were visualized inside microchannels (n=3). After that, MCF-7 cells were released from the microfluidic platforms with a 10 µL min^{-1} of flow rate for an hour via syringe pump both at 25 °C (**Figure 8.3b**) and 37 °C (**Figure 8.3b**), and we took images from microchannels. As a result of experiments, the captured cell numbers were calculated as 6.692 ± 1.647, released cell numbers at 25 °C were found as 6.238 ± 2.894, and released cell numbers at 37 °C were evaluated as 2.797 ± 458 (**Figure 8.3d**). Moreover, the capture efficiency was 74.35% ± 18.30%, whereas, the release yields were 7.97% ± 45.01% and 58.19% ± 6.84% for respectively, 25 °C and 37 °C. These results confirmed the temperature-sensitive release of MCF-7 cells as a result of the hydrophilic (25 °C) to hydrophobic (37 °C) across the LCST (**Figure 8.3e**).

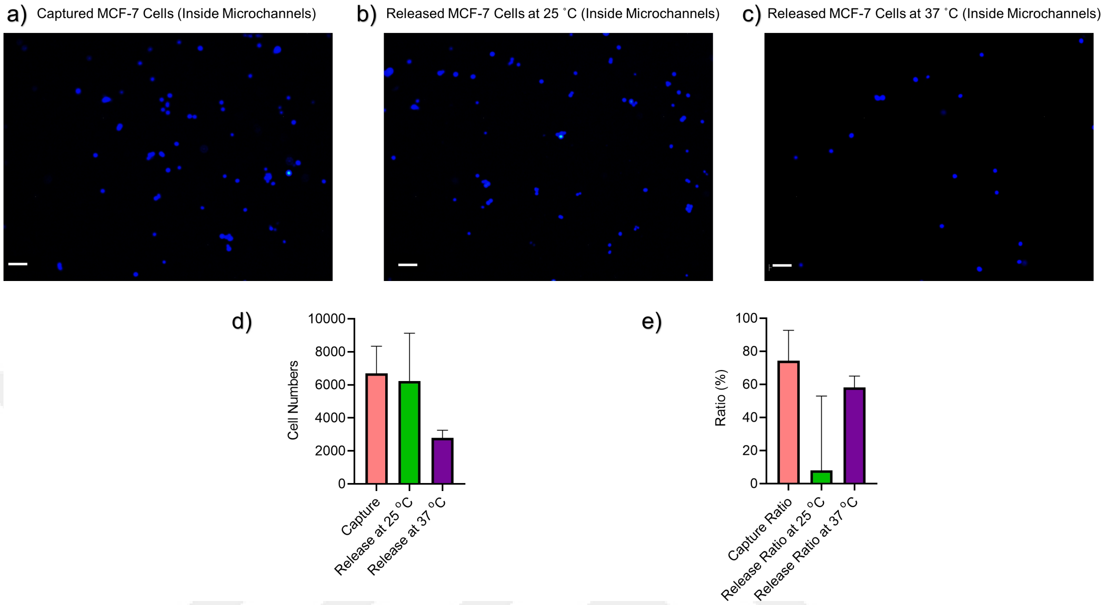

Figure 8.3: Control experiment for analyzing the temperature effect on MCF-7 cells release is depicted. **a)** Fluorescent images of captured MCF-7 cells, **b)** released MCF-7 cells at 25 °C and **c)** at 37 °C. The cells are stained with Hoechst 33342, blue dye. The data is analyzed by performing a non-parametric two-way ANOVA statistical analysis, and the statistical difference is found as non-significant. Error bars stand for standard deviations (n = 3). Scale bar = 100 μm.

The captured cell numbers and capture ratios were evaluated according to **Equation 14**. According to our results in **Chapter 7-section 3.1**, we here used 150.000 cells/mL of MCF-7 cells. As depicted in **Figure 8.4**, each type of shape including peanut, square, and oval shapes of particles modified chips were able to capture the stained MCF-7 cells. In particular, the captured cell numbers were calculated as 15.265 ± 3.397, 8.453 ± 1.283, and 11.116 ± 3.681, and their capture efficiencies were 72.69% ± 16.18%, 40.26% ± 6.11%, and 52.935% ± 17.53% for the cells captured on peanut, square, and oval shapes of particles, respectively. This result was comparable to those of the adsorption & desorption for model protein in the Chapter 6. Moreover, as shown in the BET analysis **(Chapter 3-section 3.3)** peanut-shaped particles have a higher surface area than those of square and oval shapes; hence it was expected that peanut-shaped particles capture more cells than the other shapes. Moreover, oval-shaped particles captured more cells than the square-shaped particles; and thereby these results showed the synergistic effect of morphology to capture yield.

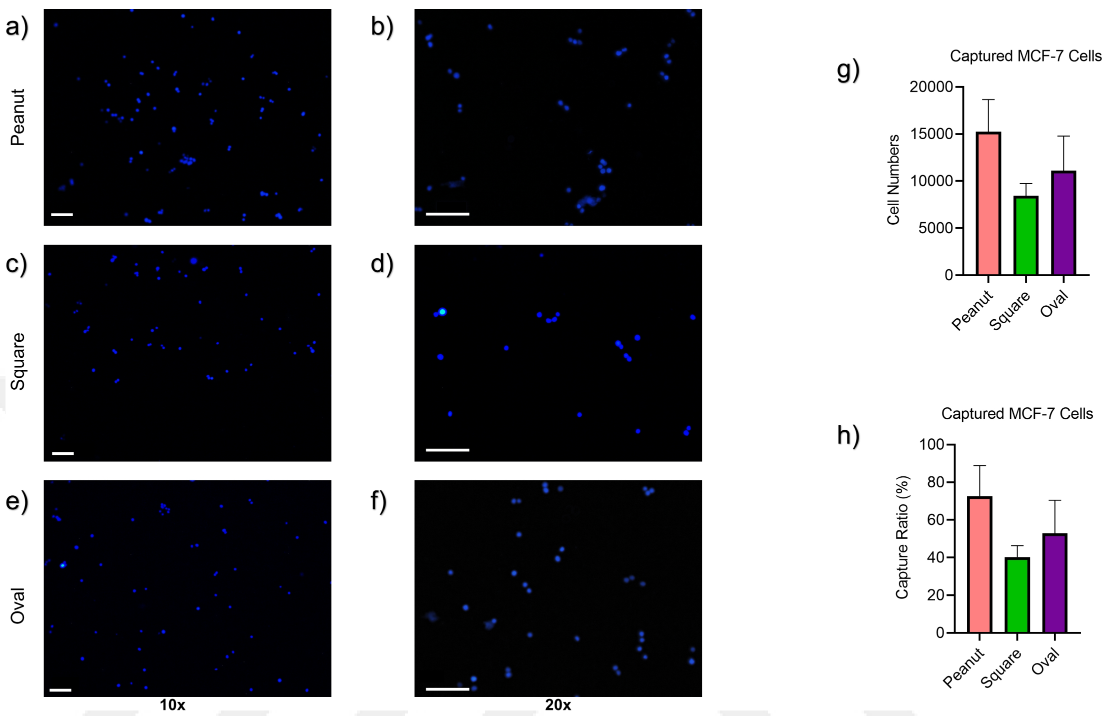

Figure 8.4: MCF-7 cells (150.000 cells/mL) are captured via different shapes of p(NIPAAm)@SiO_2 particles modified microfluidic chips. Fluorescent images of MCF-7 cells captured by **a-b)** peanut, **c-d)** square, and **e-f)** oval-shaped p(NIPAAm)@SiO_2 modified chips are shown. **g)** The captured cell numbers and **h)** cell capture ratio are depicted. The cells are stained with Hoechst 33342, blue dye. The data is analyzed by performing a non-parametric two-way ANOVA statistical analysis, and the statistical difference is found as non-significant ($p>0.05$). Error bars stand for standard deviations ($n = 3$). Scale bar = 100 μm.

In order to evaluate the effects of cell concentrations on the capture yields, we also applied 75.000 cells/mL of MCF-7 cells. As shown in **Figure 8.5**, the chips modified with each type of particles including peanut, square, and oval shapes provided capture efficiencies as 66.43 ± 34.11%, 40.38 ± 21.81%, and 54.88 ± 34.34% for peanut, square, and oval shapes, respectively. In particular, captured cell numbers were calculated as 7.307 ± 3.752, 4.441 ± 2.339, and 6.037 ± 3.777. The capture yield demonstrated that the microfluidic chips modified with different particle shapes achieved a consistent capture yield regardless of the concentration of rare cancer cells values, pointing out that the aforementioned design may have potential to be used with blood samples consisting of trace numbers of CTCs in the future [31].

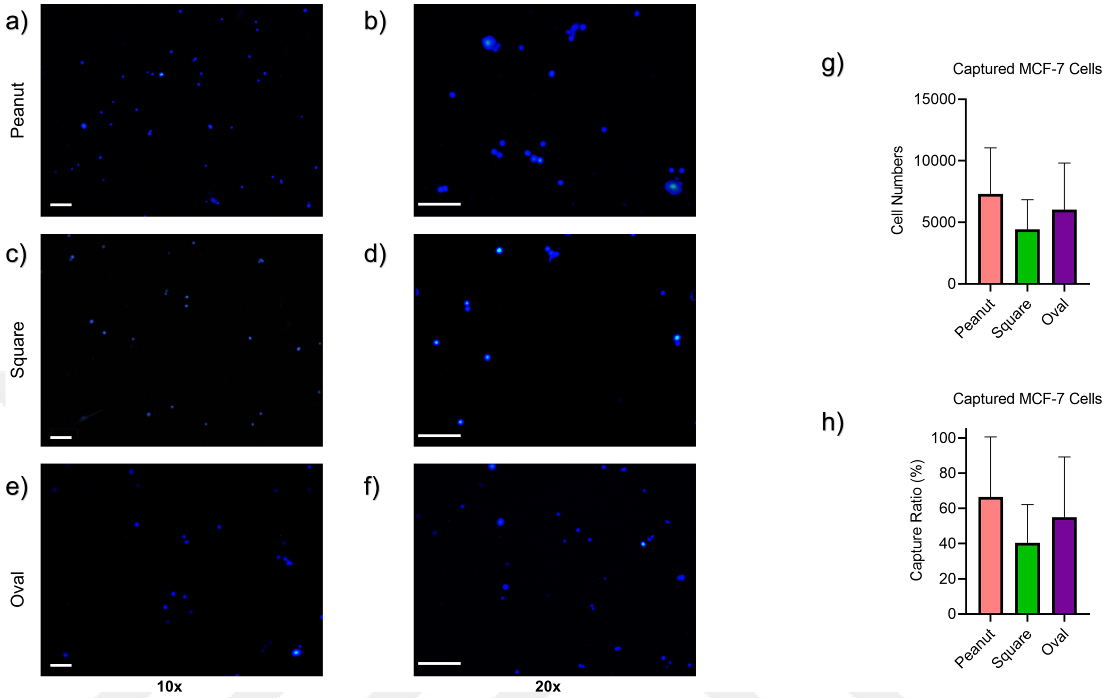

Figure 8.5: MCF-7 cells (75.000 cells/mL) are captured via different shapes of p(NIPAAm)@SiO_2 particles modified microfluidic chips. Fluorescent images of MCF-7 cells captured by **a-b)** peanut, **c-d)** square, and **e-f)** oval-shaped p(NIPAAm)@SiO_2 modified chips are presented. **g)** The captured cell numbers and **h)** cell capture ratio are depicted. The cells are stained with Hoechst 33342, blue dye. The data is analyzed by performing a non-parametric two-way ANOVA statistical analysis, and the statistical difference is found as $p>0.04$. Error bars stand for standard deviations ($n = 3$). Scale bar = 100 μm.

After that, the temperature was increased from 25 °C to 37 °C to evaluate the phase-transition of the different shapes of p(NIPAAm)@SiO_2 particles from hydrophobic to hydrophilic. Afterwards, in order to observe the release of MCF-7 cells from the microfluidic chip during the phase change from hydrophilic to hydrophobic, the temperature was increased from the room (25 °C) to the body (37 °C) temperature. After the release process, the remaining cells in microfluidic platforms were imaged on a fluorescence microscope. The microfluidic chips, which were modified with different shapes of p(NIPAAm)@SiO_2, were adjusted under the fluorescent microscope, and we then snapshotted each shape of particles with three replicates. Using an open-source software "Fiji - ImageJ Wiki", the remaining MCF-7 cells were evaluated and counted manually. The released cell numbers and release ratios were evaluated according to the **Equation 15**. As depicted in **Figure 8.6**, the chips modified with peanut, square, and oval shapes provided the release yields of 43.59% ± 16.63%, 47.67% ± 2.68%, and 42.338% ± 17.78%, respectively. In particular, the released cell numbers were calculated as 8.610 ± 2.539, 4.423 ± 226, and 6.410 ± 1.976. This stated that the highest release rate was observed in the peanut shape, whereas the lowest was found in the square shape proportional to the surface area. In **Chapter 6**, the desorbed avidin-FITC's normalized fluorescent data values were also similar to MCF-7 cell release results. Both model protein (adsorption and desorption studies) and CTC (capture and release studies) experiments demonstrated high capture and release yields of our platform. Particularly, due to controllable shape, surface areas, pore volume, pore size, and diameter differences of p(NIPAAm)@SiO_2 particles, we controlled and tuned the interactions between surface-biomolecule. These investigations confirmed that shape dependency alone would not control the capture yield of the cells; yet the cell release was also consistent and reliable as a result of the temperature-dependent phase transition of smart particles.

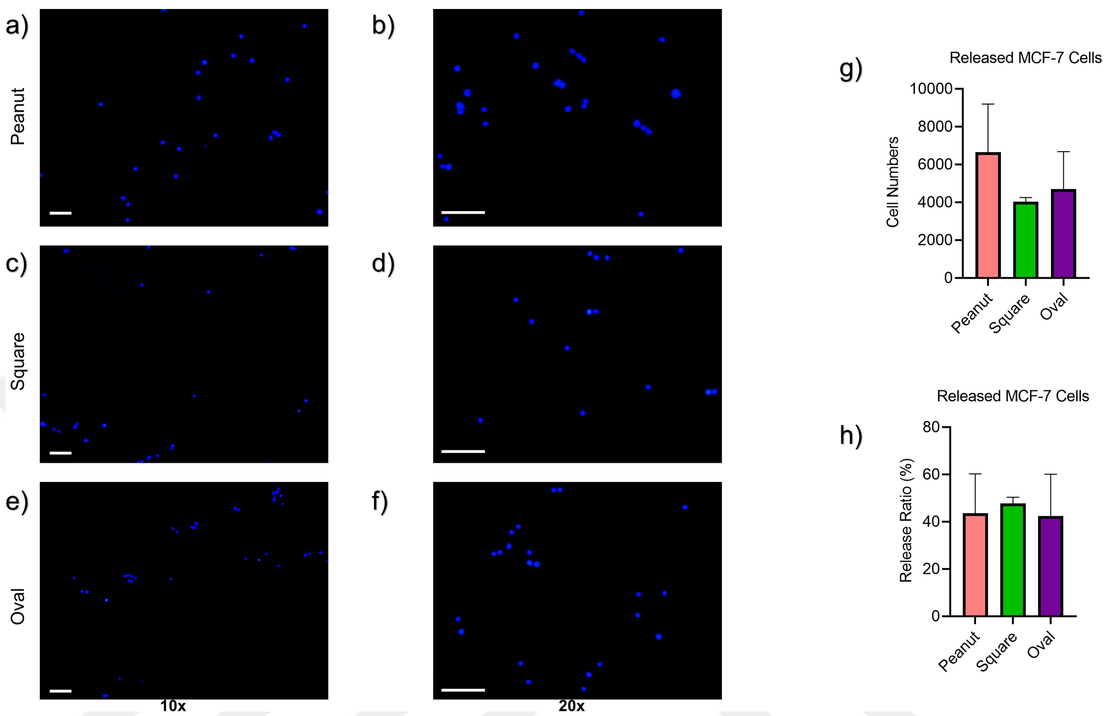

Figure 8.6: MCF-7 cells (150.000 cells/mL) are released via different shapes of p(NIPAAm)@SiO_2 particles modified microfluidic chips. Fluorescent images of MCF-7 cells released by **a-b)** peanut, **c-d)** square, and **e-f)** oval-shaped p(NIPAAm)@SiO_2 modified chips are presented. **g)** The released cell numbers and **h)** cell release ratio are depicted. The cells are stained with Hoechst 33342, blue dye. The data is analyzed by performing a non-parametric two-way ANOVA statistical analysis, and the statistical difference is found as non-significant ($p>0.05$). Error bars represent standard deviations (n = 3). Scale bar = 100 μm.

8.3.3 Viability Analysis for Isolated MCF-7 Cells

Afterwards, we took images to assess cell viability using a fluorescence microscope (Zeiss Inverted Fluorescence Microscope) and manually counted. For the investigation of cell viability after MCF-7 release, we poured a drop of the Live/Dead (ThermoFisher) reagent and MCF-7 containing solution (5 μL), which was described in **Chapter 8-section 2.3** into a glass slide and covered with a glass slip. Afterwards, we took images to evaluate the cell viability using a fluorescence microscope (Zeiss Inverted Fluorescence Microscope), and we counted them manually. Cell viability was defined as 72.02% ± 1.84%, 74.11% ± 3.76%, and 72.38% ± 2.48% for the cells released from peanut, square and oval shapes of particles, respectively. This results showed us that the cell release procedure had negligible damage to cells compared to 82.33% ± 11.09% before capture cell viability rate (**Figure 8.7**).

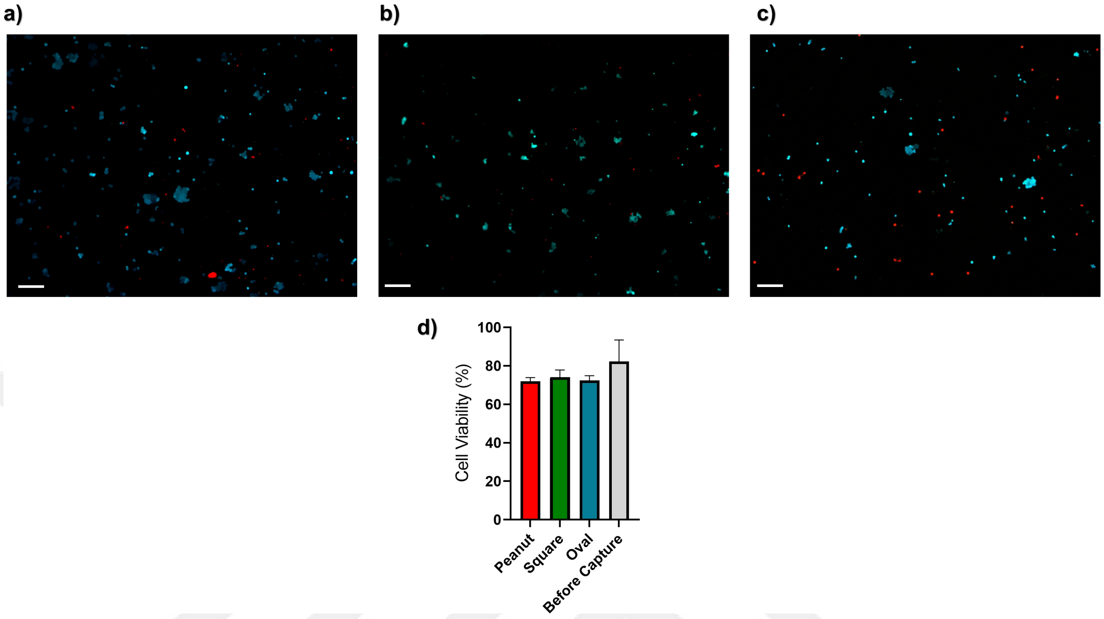

Figure 8.7: Live/Dead assay shows the viability for the extracted MCF-7 cells after the release process from **a)** peanut, **b)** square, and **c)** oval-shaped particles modified chips. **d)** Overall cell viability comparison of after release (different shapes of particles) and before capture. Green cells represent live, whereas red cells indicate dead. The data is analyzed by performing a non-parametric one-way ANOVA statistical analysis, and the statistical difference is found as non-significant. Error bars represent standard deviations (n = 3). Scale bar = 100 μm.

Additionally, these cells were investigated by the flow cytometry method before the capture and after the release processes (**Figure 8.8**). Before capturing MCF-7 cells, the dead (live/dead) rate was found as 13.6%, whereas after releasing them, the dead (live/dead) rate of the isolated cells was around 21.4%, confirming our fluorescence data and pointing out that the released MCF-7 cells experienced minimal damage, and they were highly viable.

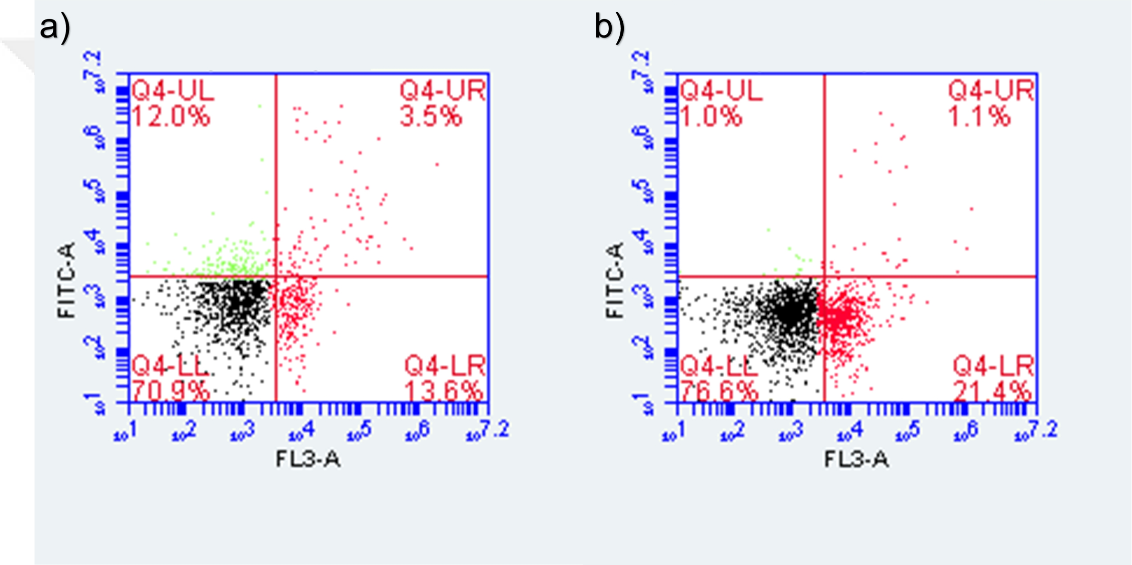

Figure 8.8: Flow cytometry analysis (live/dead) is shown for MCF-7 cells **a)** before the capture and **b)** after the release processes.

8.4 CONCLUSION and FUTURE PROSPECTS

CTCs/CTM are unique elements to comprehend insights of cancer metastasis, biology, progression, and treatment possibilities along with conventional and emergent cancer biomarkers. Practically, “biopsy” is the most broadly used technique for the diagnosis of cancer, and it guides and benchmarks the associated therapies. On the other hand, the heterogeneity characteristics of the tumor environment and the rarity of cancer cells lead to the disintegration of the cancer cells subpopulation, and subsequently, this biological limitation intereferes in developing biomedical methods to find out cancer cells. Regarding this aspect, new-fangled methods are essential to implement more sophisticated platforms in the aspects of daily clinical evaluations. By gaining benefits of uncovered biomarkers including EpCAM for specific CTCs isolation, firstly, CellSearch® was launched as a validated CTCs isolation technique. During the progression of cancer investigation, the requirement for CTCs investigations was not only limited to capturing or releasing rare tumor cells, and also, isolating them along with smart material-assisted methodologies by using external stimuli is a crucial aspect; thereby, we have elaborated different aspects of CTCs isolation in terms of smart material-utilized platforms.

In this thesis, we aimed to fabricate an efficient, easy-to-use, accurate, and label-free microfluidic chips that address unmet needs in the capture and release of CTCs for isolation of them. There are some researches performed and ongoing focusing on microfluidic platforms to capture and release cancer cells [1]. However, their surface area hinders the capture and release efficiency. To hurdle this limitation, we here implement varying shapes of bio-inspired silica particles (peanut, oval, and square shapes) to change, enhance, and control the surface area in the microfluidic chips. For this purpose, at the first glance, hematite (α-Fe2O3) hard templates with peanut, square, and oval morphologies were fabricated. Afterwards, different-shaped hard templates were homogeneously coated with silica-gel without any agglomerations. The produced $Fe_2O_3@SiO_2$ core-shell structures were treated by using HCl acidic mixture in order to remove the core structure for forming different shapes of hollow silica-gel structures. By using the surface-initiated ATRP method, harmonizing shape-dependent silica particles with thermo-sensitive p(NIPAAm) compounds enabled to produce 3-D structures, where surface area and so that the interactions between cancer cells with the microfluidic platform can be controlled precisely. Later, surface modifications with succinimide and maleimide functional groups were employed to the outer shells of p(NIPAAm)@SiO_2 colloids for further surface chemistry approaches.

Before implementing these particles to the microfluidic chips, we performed numerical simulations with the aim of stabilizing flow velocity and shear stress profile in the microchannels. We have optimized the laminar flow characteristics to immobilize biomolecules into the channels with 10 µL min^{-1} of flow rate. Moreover, typical shear stress profiles of microfluidic devices along with 50 µm of channel height was found suitable for biomolecule immobilization due to the low shear stress profiles. Furthermore, the fabricated microfluidics was tested by applying biotin protein to the glass surface with surface chemistry.

After that, we immobilized the bio-inspired silica particles to the microfluidic chips. In this regard, we also characterized after the immobilization process, and the outcomes from five distinct characterization methods contact angle, AFM, XPS, SEM, and Upright fluorescence microscopy complementary assessments exhibited that the short (3-MPS) modification was able to create highly active surfaces than the medium (Silane-PEG-SH 1k) and long (Silane-PEG-SH 5k)-distance modifications. Thus, we decided to continue with the short (3-MPS) modification for further experiments.

As proof-of-concept or preliminary work, we have shown adsorption & desorption of model proteins through temperature-sensitive different-shaped p(NIPAAm)@SiO_2 particles modified microfluidic platforms. Not only adsorbing proteins but also desorbing them with high yield, especially at body temperature (37 °C) demonstrated the phase alterations from hydrophobic to hydrophilic. This bioinspired strategy also has enabled the controlled adsorption & desorption rate via changing the shape of particles. With that, we revealed the temperature-induced phase transformation that could also lead to the isolation and release of cancer cells; thereby, we continued with this experimental design, setup, and parameters for further the capture and release experiments.

After that, the EpCAM-positive MCF-7 cells were cultured in an incubator. Furthermore, we have tested the cytotoxicity activities of SiO2 and P(NIPAAm)@SiO_2 particles against human breast cancer cells (MCF-7) in versatile conditions for observing the biocompatibility of our platform by long-term culturing , MTT assay analysis, and Live/Dead viability/cytotoxicity analyses. As a result, we did not observe any toxic effects and influences on the cell viability of MCF-7 caused by SiO_2 and p(NIPAAm)@SiO_2 particles.

Finally, we decorated anti-EpCAM antibodies on different shapes of particles, which were tethered with a short linkers (3-MPS) to the chip surface. After understanding the successful binding of anti-EpCAM antibodies, we applied MCF-7 cells into the microfluidic chips. As a result, MCF-7 cells were captured with high efficiencies (40% to 70%) with different concentrations (60.000 cells/mL, 75.000 cells/mL to 150.000 cells/mL). In particular, while employing the peanut shapes particles, the highest number of cells (15.265 ± 3.397) along with the maximum capture efficiency (72.69% ± 16.18%) were captured in the chips, and this might be due to the higher surface area. Again, in the chips modified with peanut shapes of particles, the number and ratio of released MCF-7 cells were was the highest. On the other hand, the lowest data was observed in the square shape. Finally, cell viabilities (live/dead) were investigated. Before capture and after the release process, the cell viabilities (live/dead) were not statistically different than those in control sample, pointing out that the cell capture and release procedures had negligible damages to cells.

On the other hand, even if this platform has enabled a high capture and release efficiency, aforementioned strategy have some limitations that can be further improved in the future. First of all, repeatability of the microfluidic platform is slightly limited due to the fact that the surfaces of microchannels did not provide a homogeneous distribution of p(NIPAAm)@SiO_2 particles, as can be seen from **Figure 5.12, 8.1**. Despite the fact that the short (3-MPS) modification has been distinguished in terms of biomolecules loading capacity, we tried only one concentration value by inspiring our previous work [74], yet surface chemistry would be more active if the concentration value of 3-MPS increases in order to create uniform surfaces. By creating more homogeneous substrates, the standart deviation values of CTCs capture and release yields also can be decreased. Additionally, despite the high capture ratio, the release yield can be enhanced by increasing the flow rate and release time of the MCF-7 cells; yet there is a potential to damage cell viability and cellular intactness during this process. Therefore, the future works can integrate different heating strategies such as laser that will also enable for local release of cells or harmonize different polymers such as polypyrrole that can provide a high heat capacitance. With these strategies, a higher release ratio can be achieved [184, 185, 186]. Moreover, for the investigation of specificity, different cell lines such as low- or non-EpCAM expressing cells can be tested on this platform. We therefore proved the accuracy and validation of the system in terms of non-dependency of cell concentrations, this aforementioned design can be also used for spiked samples or blood samples consisting of trace numbers of CTCs. In other words, there is always room for raising the quality and capability of our platform with much superior performance. Nevertheless, the way to reach a simplified and expedited fabrication process will enable a better understanding for CTCs as a liquid biopsy that will also enhance the reproducibility of these platforms.

Bibliography

[1] F. Inci and K. Sagdic, "Smart material-integrated systems for isolation and profiling of rare cancer cells and emboli," *Advanced Engineering Materials*, vol. 24, no. 3, 2021.

[2] J. Fares, M. Y. Fares, H. H. Khachfe, H. A. Salhab, and Y. Fares, "Molecular principles of metastasis: a hallmark of cancer revisited," *Signal transduction and targeted therapy*, vol. 5, no. 1, pp. 1–17, 2020.

[3] L. Freire-de Lima, "Sweet and sour: the impact of differential glycosylation in cancer cells undergoing epithelial–mesenchymal transition," *Frontiers in oncology*, vol. 4, p. 59, 2014.

[4] H. Ruan, X. Wu, C. Yang, Z. Li, Y. Xia, T. Xue, Z. Shen, and A. Wu, "A supersensitive ctc analysis system based on triangular silver nanoprisms and spion with function of capture, enrichment, detection, and release," *ACS Biomaterials Science & Engineering*, vol. 4, no. 3, pp. 1073–1082, 2018.

[5] S.-B. Cheng, M. Xie, Y. Chen, J. Xiong, Y. Liu, Z. Chen, S. Guo, Y. Shu, M. Wang, B.-F. Yuan, *et al.*, "Three-dimensional scaffold chip with thermosensitive coating for capture and reversible release of individual and cluster of circulating tumor cells," *Analytical chemistry*, vol. 89, no. 15, pp. 7924–7932, 2017.

[6] J. Zhang, B. Lin, L. Wu, M. Huang, X. Li, H. Zhang, J. Song, W. Wang, G. Zhao, Y. Song, *et al.*, "Dna nanolithography enables a highly ordered recognition interface in a microfluidic chip for the efficient capture and

release of circulating tumor cells," *Angewandte Chemie*, vol. 132, no. 33, pp. 14219–14223, 2020.

[7] N.-N. Lu, M. Xie, J. Wang, S.-W. Lv, J.-S. Yi, W.-G. Dong, and W.-H. Huang, "Biotin-triggered decomposable immunomagnetic beads for capture and release of circulating tumor cells," *ACS applied materials & interfaces*, vol. 7, no. 16, pp. 8817–8826, 2015.

[8] D. Wu, Y. Yu, D. Jin, M.-M. Xiao, Z.-Y. Zhang, and G.-J. Zhang, "Dual-aptamer modified graphene field-effect transistor nanosensor for label-free and specific detection of hepatocellular carcinoma-derived microvesicles," *Analytical chemistry*, vol. 92, no. 5, pp. 4006–4015, 2020.

[9] H. Liu, Y. Li, K. Sun, J. Fan, P. Zhang, J. Meng, S. Wang, and L. Jiang, "Dual-responsive surfaces modified with phenylboronic acid-containing polymer brush to reversibly capture and release cancer cells," *Journal of the American Chemical Society*, vol. 135, no. 20, pp. 7603–7609, 2013.

[10] S.-W. Lv, J. Wang, M. Xie, N.-N. Lu, Z. Li, X.-W. Yan, S.-L. Cai, P.-A. Zhang, W.-G. Dong, and W.-H. Huang, "Photoresponsive immunomagnetic nanocarrier for capture and release of rare circulating tumor cells," *Chemical science*, vol. 6, no. 11, pp. 6432–6438, 2015.

[11] Q. Huang, B. Cai, B. Chen, L. Rao, Z. He, R. He, F. Guo, L. Zhao, K. K. Kondamareddy, W. Liu, *et al.*, "Circulating tumor cell isolation: Efficient purification and release of circulating tumor cells by synergistic effect of biomarker and sio2@ gel-microbead-based size difference amplification (adv. healthcare mater. 13/2016)," *Advanced Healthcare Materials*, vol. 5, no. 13, pp. 1525–1525, 2016.

[12] B. N. Ames, "Mutagenesis and carcinogenesis: endogenous and exogenous factors," *Environmental and molecular mutagenesis*, vol. 14, no. S16, pp. 66–77, 1989.

[13] A. M. Gonzalez-Angulo, B. T. Hennessy, and G. B. Mills, "Future of personalized medicine in oncology: a systems biology approach," *Journal of clinical oncology*, vol. 28, no. 16, p. 2777, 2010.

[14] A. Haase-Fielitz, R. Bellomo, P. Devarajan, D. Story, G. Matalanis, D. Dragun, and M. Haase, “Novel and conventional serum biomarkers predicting acute kidney injury in adult cardiac surgery—a prospective cohort study,” *Critical care medicine*, vol. 37, no. 2, pp. 553–560, 2009.

[15] C. L. Sawyers, “The cancer biomarker problem,” *Nature*, vol. 452, no. 7187, pp. 548–552, 2008.

[16] N. Aceto, A. Bardia, D. T. Miyamoto, M. C. Donaldson, B. S. Wittner, J. A. Spencer, M. Yu, A. Pely, A. Engstrom, H. Zhu, *et al.*, “Circulating tumor cell clusters are oligoclonal precursors of breast cancer metastasis,” *Cell*, vol. 158, no. 5, pp. 1110–1122, 2014.

[17] E. A. Punnoose, S. K. Atwal, J. M. Spoerke, H. Savage, A. Pandita, R.-F. Yeh, A. Pirzkall, B. M. Fine, L. C. Amler, D. S. Chen, *et al.*, “Molecular biomarker analyses using circulating tumor cells,” *PloS one*, vol. 5, no. 9, p. e12517, 2010.

[18] I. Baccelli, A. Schneeweiss, S. Riethdorf, A. Stenzinger, A. Schillert, V. Vogel, C. Klein, M. Saini, T. Bäuerle, M. Wallwiener, *et al.*, “Identification of a population of blood circulating tumor cells from breast cancer patients that initiates metastasis in a xenograft assay,” *Nature biotechnology*, vol. 31, no. 6, pp. 539–544, 2013.

[19] M. Umer, R. Vaidyanathan, N.-T. Nguyen, and M. J. Shiddiky, “Circulating tumor microemboli: Progress in molecular understanding and enrichment technologies,” *Biotechnology advances*, vol. 36, no. 4, pp. 1367–1389, 2018.

[20] J. Kapeleris, A. Kulasinghe, M. E. Warkiani, I. Vela, L. Kenny, K. O’Byrne, and C. Punyadeera, “The prognostic role of circulating tumor cells (ctcs) in lung cancer,” *Frontiers in oncology*, vol. 8, p. 311, 2018.

[21] L. A. Devriese, E. E. Voest, J. H. Beijnen, and J. H. Schellens, “Circulating tumor cells as pharmacodynamic biomarker in early clinical oncological trials,” *Cancer treatment reviews*, vol. 37, no. 8, pp. 579–589, 2011.

[22] L. Khoja, P. Lorigan, C. Zhou, M. Lancashire, J. Booth, J. Cummings, R. Califano, G. Clack, A. Hughes, and C. Dive, “Biomarker utility of circulating tumor cells in metastatic cutaneous melanoma,” *Journal of Investigative Dermatology*, vol. 133, no. 6, pp. 1582–1590, 2013.

[23] L. Zhang, L. Ridgway, M. Wetzel, J. Ngo, W. Yin, D. Kumar, J. Goodman, M. Groves, and D. Marchetti, “The identification and isolation of breast cancer ctcs with brain metastatic competence,” *Sci Transl Med*, vol. 5, no. 180, pp. 84–93, 2013.

[24] M. Cristofanilli, J.-Y. Pierga, J. Reuben, A. Rademaker, A. A. Davis, D. J. Peeters, T. Fehm, F. Nolé, R. Gisbert-Criado, D. Mavroudis, *et al.*, “The clinical use of circulating tumor cells (ctcs) enumeration for staging of metastatic breast cancer (mbc): International expert consensus paper,” *Critical reviews in oncology/hematology*, vol. 134, pp. 39–45, 2019.

[25] E. HC, “Cancer cells in the circulating blood; a clinical study on the occurrence of cancer cells in the peripheral blood and in venous blood draining the tumour area at operation,” *Ugeskrift for laeger*, vol. 117, no. 25, pp. 822–823, 1955.

[26] D. R. Coman, R. P. deLong, and M. McCutcheon, “Studies on the mechanisms of metastasis. the distribution of tumors in various organs in relation to the distribution of arterial emboli,” *Cancer Research*, vol. 11, no. 8, pp. 648–651, 1951.

[27] I. Zeidman, “Metastasis: a review of recent advances,” *Cancer research*, vol. 17, no. 3, pp. 157–162, 1957.

[28] I. Fidler, “Selection of successive tumour lines for metastasis,” *Nature New Biology*, vol. 242, no. 118, pp. 148–149, 1973.

[29] S. Seal, “Silicone flotation: A simple quantitative method for the isolation of free-floating cancer cells from the blood,” *Cancer*, vol. 12, no. 3, pp. 590–595, 1959.

[30] D. T. Miyamoto, Y. Zheng, B. S. Wittner, R. J. Lee, H. Zhu, K. T. Broderick, R. Desai, D. B. Fox, B. W. Brannigan, J. Trautwein, *et al.*, "Rna-seq of single prostate ctcs implicates noncanonical wnt signaling in antiandrogen resistance," *Science*, vol. 349, no. 6254, pp. 1351–1356, 2015.

[31] W. J. Allard, J. Matera, M. C. Miller, M. Repollet, M. C. Connelly, C. Rao, A. G. Tibbe, J. W. Uhr, and L. W. Terstappen, "Tumor cells circulate in the peripheral blood of all major carcinomas but not in healthy subjects or patients with nonmalignant diseases," *Clinical cancer research*, vol. 10, no. 20, pp. 6897–6904, 2004.

[32] H. G. Burkitt, B. Young, P. R. Wheater, and J. W. Heath, *Wheater's functional histology: a text and colour atlas*. Churchill Livingstone, 1993.

[33] L. A. Liotta, J. Kleinerman, and G. M. Saldel, "The significance of hematogenous tumor cell clumps in the metastatic process," *Cancer research*, vol. 36, no. 3, pp. 889–894, 1976.

[34] F. Tang, C. Barbacioru, Y. Wang, E. Nordman, C. Lee, N. Xu, X. Wang, J. Bodeau, B. B. Tuch, A. Siddiqui, *et al.*, "mrna-seq whole-transcriptome analysis of a single cell," *Nature methods*, vol. 6, no. 5, pp. 377–382, 2009.

[35] Y. M. B. A. Wittner and S. Stott, "Smas me ting dt isakoff sj ciciliano jc wells mn shah am concannon kf donaldson mc sequist lv brachtel e. sgroi d. baselga j. ramaswamy s. toner m. haber da maheswaran s," *Science*, vol. 339, pp. 580–584, 2013.

[36] M. G. Krebs, R. L. Metcalf, L. Carter, G. Brady, F. H. Blackhall, and C. Dive, "Molecular analysis of circulating tumour cells—biology and biomarkers," *Nature reviews Clinical oncology*, vol. 11, no. 3, pp. 129–144, 2014.

[37] Q. Zhao, M. Barclay, J. Hilkens, X. Guo, H. Barrow, J. M. Rhodes, and L.-G. Yu, "Interaction between circulating galectin-3 and cancer-associated muc1 enhances tumour cell homotypic aggregation and prevents anoikis," *Molecular cancer*, vol. 9, no. 1, pp. 1–12, 2010.

[38] D. G. Duda, A. M. Duyverman, M. Kohno, M. Snuderl, E. J. Steller, D. Fukumura, and R. K. Jain, “Malignant cells facilitate lung metastasis by bringing their own soil,” *Proceedings of the National Academy of Sciences*, vol. 107, no. 50, pp. 21677–21682, 2010.

[39] Y. Hong, F. Fang, and Q. Zhang, “Circulating tumor cell clusters: What we know and what we expect,” *International journal of oncology*, vol. 49, no. 6, pp. 2206–2216, 2016.

[40] C. Alix-Panabières and K. Pantel, “Circulating tumor cells: liquid biopsy of cancer,” *Clinical chemistry*, vol. 59, no. 1, pp. 110–118, 2013.

[41] L. E. Lowes and A. L. Allan, “Recent advances in the molecular characterization of circulating tumor cells,” *Cancers*, vol. 6, no. 1, pp. 595–624, 2014.

[42] S.-I. Han and K.-H. Han, “Electrical detection method for circulating tumor cells using graphene nanoplates,” *Analytical chemistry*, vol. 87, no. 20, pp. 10585–10592, 2015.

[43] R. Li, Z. Gong, Y. Liu, X. Zhao, and S. Guo, “Detection of circulating tumor cells and single cell extraction technology: principle, effect and application prospect,” *Nano Futures*, vol. 5, no. 3, p. 032002, 2021.

[44] J. Ouyang, M. Chen, W.-J. Bao, Q.-W. Zhang, K. Wang, and X.-H. Xia, “Morphology controlled poly (aminophenylboronic acid) nanostructures as smart substrates for enhanced capture and release of circulating tumor cells,” *Advanced Functional Materials*, vol. 25, no. 38, pp. 6122–6130, 2015.

[45] L.-G. Liang, Y.-F. Sheng, S. Zhou, F. Inci, L. Li, U. Demirci, and S. Wang, “An integrated double-filtration microfluidic device for detection of extracellular vesicles from urine for bladder cancer diagnosis,” in *Extracellular Vesicles*, pp. 355–364, Springer, 2017.

[46] A. F. Sarioglu, N. Aceto, N. Kojic, M. C. Donaldson, M. Zeinali, B. Hamza, A. Engstrom, H. Zhu, T. K. Sundaresan, D. T. Miyamoto, *et al.*, “A microfluidic device for label-free, physical capture of circulating tumor cell clusters,” *Nature methods*, vol. 12, no. 7, pp. 685–691, 2015.

[47] F. I. Thege, T. B. Lannin, T. N. Saha, S. Tsai, M. L. Kochman, M. A. Hollingsworth, A. D. Rhim, and B. J. Kirby, “Microfluidic immunocapture of circulating pancreatic cells using parallel epcam and muc1 capture: characterization, optimization and downstream analysis,” *Lab on a Chip*, vol. 14, no. 10, pp. 1775–1784, 2014.

[48] Z. Zhang, J. Xu, B. Hong, and X. Chen, “The effects of 3d channel geometry on ctc passing pressure–towards deformability-based cancer cell separation,” *Lab on a Chip*, vol. 14, no. 14, pp. 2576–2584, 2014.

[49] H. Esmaeilsabzali, T. V. Beischlag, M. E. Cox, A. M. Parameswaran, and E. J. Park, “Detection and isolation of circulating tumor cells: principles and methods,” *Biotechnology advances*, vol. 31, no. 7, pp. 1063–1084, 2013.

[50] J. M. Jackson, M. A. Witek, J. W. Kamande, and S. A. Soper, “Materials and microfluidics: enabling the efficient isolation and analysis of circulating tumour cells,” *Chemical Society Reviews*, vol. 46, no. 14, pp. 4245–4280, 2017.

[51] C. Jin, S. M. McFaul, S. P. Duffy, X. Deng, P. Tavassoli, P. C. Black, and H. Ma, “Technologies for label-free separation of circulating tumor cells: from historical foundations to recent developments,” *Lab on a Chip*, vol. 14, no. 1, pp. 32–44, 2014.

[52] J. H. Kang, S. Krause, H. Tobin, A. Mammoto, M. Kanapathipillai, and D. E. Ingber, “A combined micromagnetic-microfluidic device for rapid capture and culture of rare circulating tumor cells,” *Lab on a Chip*, vol. 12, no. 12, pp. 2175–2181, 2012.

[53] T. M. Gorges, I. Tinhofer, M. Drosch, L. Röse, T. M. Zollner, T. Krahn, and O. von Ahsen, “Circulating tumour cells escape from epcam-based detection due to epithelial-to-mesenchymal transition,” *BMC cancer*, vol. 12, no. 1, pp. 1–13, 2012.

[54] L. Flores, D. Kindelberger, A. Ligon, M. Capelletti, M. Fiorentino, M. Loda, E. Cibas, P. Jänne, and I. Krop, “Improving the yield of circulating tumour cells facilitates molecular characterisation and recognition

of discordant her2 amplification in breast cancer," *British journal of cancer*, vol. 102, no. 10, pp. 1495–1502, 2010.

[55] F. A. Coumans, G. van Dalum, M. Beck, and L. W. Terstappen, "Filter characteristics influencing circulating tumor cell enrichment from whole blood," *PloS one*, vol. 8, no. 4, p. e61770, 2013.

[56] G. Vona, A. Sabile, and M. Louha, "sitruk v, romana s, schutze k, capron f, franco d, pazzagli m, vekemans m, lacour b, brechot c, paterlini-brechot p. isolation by size of epithelial tumor cells: a new method for the immunomorphological and molecular characterization of circulating tumor cells," *Am J Pathol*, vol. 156, pp. 57–63, 2000.

[57] J. A. Awe, M. C. Xu, J. Wechsler, N. Benali-Furet, Y. E. Cayre, J. Saranchuk, D. Drachenberg, and S. Mai, "Three-dimensional telomeric analysis of isolated circulating tumor cells (ctcs) defines ctc subpopulations," *Translational oncology*, vol. 6, no. 1, pp. 51–IN4, 2013.

[58] O. Lara, X. Tong, M. Zborowski, and J. J. Chalmers, "Enrichment of rare cancer cells through depletion of normal cells using density and flow-through, immunomagnetic cell separation," *Experimental hematology*, vol. 32, no. 10, pp. 891–904, 2004.

[59] D. L. Adams, S. Stefansson, C. Haudenschild, S. S. Martin, M. Charpentier, S. Chumsri, M. Cristofanilli, C.-M. Tang, and R. K. Alpaugh, "Cytometric characterization of circulating tumor cells captured by microfiltration and their correlation to the cellsearch® ctc test," *Cytometry Part A*, vol. 87, no. 2, pp. 137–144, 2015.

[60] Y. Song, T. Tian, Y. Shi, W. Liu, Y. Zou, T. Khajvand, S. Wang, Z. Zhu, and C. Yang, "Enrichment and single-cell analysis of circulating tumor cells," *Chemical science*, vol. 8, no. 3, pp. 1736–1751, 2017.

[61] G. Gallerani, C. Cocchi, M. Bocchini, F. Piccinini, and F. Fabbri, "Characterization of tumor cells using a medical wire for capturing circulating tumor cells: a 3d approach based on immunofluorescence and dna fish," *JoVE (Journal of Visualized Experiments)*, no. 130, p. e56936, 2017.

[62] F. Ge, H. Zhang, D. D. Wang, L. Li, and P. P. Lin, "Enhanced detection and comprehensive in situ phenotypic characterization of circulating and disseminated heteroploid epithelial and glioma tumor cells," *Oncotarget*, vol. 6, no. 29, p. 27049, 2015.

[63] S. L. Werner, R. P. Graf, M. Landers, D. T. Valenta, M. Schroeder, S. B. Greene, N. Bales, R. Dittamore, and D. Marrinucci, "Analytical validation and capabilities of the epic ctc platform: enrichment-free circulating tumour cell detection and characterization," *Journal of Circulating Biomarkers*, vol. 4, p. 3, 2015.

[64] B. Brandt, R. Junker, C. Griwatz, S. Heidl, O. Brinkmann, A. Semjonow, G. Assmann, and K. S. Zänker, "Isolation of prostate-derived single cells and cell clusters from human peripheral blood," *Cancer research*, vol. 56, no. 20, pp. 4556–4561, 1996.

[65] A. Sabile, M. Louha, E. Bonte, K. Poussin, G. Vona, A. Mejean, Y. Chretien, L. Bougas, B. Lacour, F. Capron, *et al.*, "Efficiency of ber-ep4 antibody for isolating circulating epithelial tumor cells before rt-pcr detection," *American journal of clinical pathology*, vol. 112, no. 2, pp. 171–178, 1999.

[66] A. A. Powell, A. H. Talasaz, H. Zhang, M. A. Coram, A. Reddy, G. Deng, M. L. Telli, R. H. Advani, R. W. Carlson, J. A. Mollick, *et al.*, "Single cell profiling of circulating tumor cells: transcriptional heterogeneity and diversity from breast cancer cell lines," *PloS one*, vol. 7, no. 5, p. e33788, 2012.

[67] J. Autebert, B. Coudert, J. Champ, L. Saias, E. T. Guneri, R. Lebofsky, F.-C. Bidard, J.-Y. Pierga, F. Farace, S. Descroix, *et al.*, "High purity microfluidic sorting and analysis of circulating tumor cells: towards routine mutation detection," *Lab on a Chip*, vol. 15, no. 9, pp. 2090–2101, 2015.

[68] C. M. Castro, A. A. Ghazani, J. Chung, H. Shao, D. Issadore, T.-J. Yoon, R. Weissleder, and H. Lee, "Miniaturized nuclear magnetic resonance platform for detection and profiling of circulating tumor cells," *Lab on a Chip*, vol. 14, no. 1, pp. 14–23, 2014.

[69] C. M. Earhart, C. E. Hughes, R. S. Gaster, C. C. Ooi, R. J. Wilson, L. Y. Zhou, E. W. Humke, L. Xu, D. J. Wong, S. B. Willingham, *et al.*, "Isolation and mutational analysis of circulating tumor cells from lung cancer patients with magnetic sifters and biochips," *Lab on a Chip*, vol. 14, no. 1, pp. 78–88, 2014.

[70] S.-m. Park, D. J. Wong, C. C. Ooi, D. M. Kurtz, O. Vermesh, A. Aalipour, S. Suh, K. L. Pian, J. J. Chabon, S. H. Lee, *et al.*, "Molecular profiling of single circulating tumor cells from lung cancer patients," *Proceedings of the National Academy of Sciences*, vol. 113, no. 52, pp. E8379–E8386, 2016.

[71] A. A. Ashkarran and M. Mahmoudi, "Magnetic levitation systems for disease diagnostics," *Trends in Biotechnology*, vol. 39, no. 3, pp. 311–321, 2021.

[72] N. G. Durmus, H. C. Tekin, S. Guven, K. Sridhar, A. Arslan Yildiz, G. Calibasi, I. Ghiran, R. W. Davis, L. M. Steinmetz, and U. Demirci, "Magnetic levitation of single cells," *Proceedings of the National Academy of Sciences*, vol. 112, no. 28, pp. E3661–E3668, 2015.

[73] F. Inci, M. O. Ozen, Y. Saylan, M. Miansari, D. Cimen, R. Dhara, T. Chinnasamy, M. Yuksekkaya, C. Filippini, D. K. Kumar, *et al.*, "A novel on-chip method for differential extraction of sperm in forensic cases," *Advanced Science*, vol. 5, no. 9, p. 1800121, 2018.

[74] S. Wang, F. Inci, T. L. Chaunzwa, A. Ramanujam, A. Vasudevan, S. Subramanian, A. C. F. Ip, B. Sridharan, U. A. Gurkan, and U. Demirci, "Portable microfluidic chip for detection of escherichia coli in produce and blood," *International journal of nanomedicine*, vol. 7, p. 2591, 2012.

[75] X. Zhang, M. A. Hashem, X. Chen, and H. Tan, "On passing a non-newtonian circulating tumor cell (ctc) through a deformation-based microfluidic chip," *Theoretical and Computational Fluid Dynamics*, vol. 32, no. 6, pp. 753–764, 2018.

[76] M. G. Ahmed, M. F. Abate, Y. Song, Z. Zhu, F. Yan, Y. Xu, X. Wang, Q. Li, and C. Yang, "Isolation, detection, and antigen-based profiling of

circulating tumor cells using a size-dictated immunocapture chip," *Angewandte Chemie International Edition*, vol. 56, no. 36, pp. 10681–10685, 2017.

[77] W. S. Low and N. A. Kadri, "Computational analysis of enhanced circulating tumour cell (ctc) separation in a microfluidic system with an integrated dielectrophoretic-magnetophorectic (dep-map) technique," *Chemosensors*, vol. 4, no. 3, p. 14, 2016.

[78] Y. Zhou, Z. Ma, and Y. Ai, "Hybrid microfluidic sorting of rare cells based on high throughput inertial focusing and high accuracy acoustic manipulation," *RSC advances*, vol. 9, no. 53, pp. 31186–31195, 2019.

[79] X. Zhang, X. Chen, and H. Tan, "On the thin-film-dominated passing pressure of cancer cell squeezing through a microfluidic ctc chip," *Microfluidics and Nanofluidics*, vol. 21, no. 9, pp. 1–13, 2017.

[80] M.-C. Chang, Y.-T. Chang, J.-Y. Chen, Y.-M. Jeng, C.-Y. Yang, Y.-W. Tien, S.-H. Yang, H.-L. Chen, T.-Y. Liang, C.-F. Wang, *et al.*, "Clinical significance of circulating tumor microemboli as a prognostic marker in patients with pancreatic ductal adenocarcinoma," *Clinical chemistry*, vol. 62, no. 3, pp. 505–513, 2016.

[81] S. Wang, A. Thomas, E. Lee, S. Yang, X. Cheng, and Y. Liu, "Highly efficient and selective isolation of rare tumor cells using a microfluidic chip with wavy-herringbone micro-patterned surfaces," *Analyst*, vol. 141, no. 7, pp. 2228–2237, 2016.

[82] S. Nath, M. Pigula, A. P. Khan, W. Hanna, M. K. Ruhi, F. M. Dehkordy, K. Pushpavanam, K. Rege, K. Moore, Y. Tsujita, *et al.*, "Flow-induced shear stress confers resistance to carboplatin in an adherent three-dimensional model for ovarian cancer: A role for egfr-targeted photoimmunotherapy informed by physical stress," *Journal of clinical medicine*, vol. 9, no. 4, p. 924, 2020.

[83] G. Hvichia, Z. Parveen, C. Wagner, M. Janning, J. Quidde, A. Stein, V. Müller, S. Loges, R. Neves, N. Stoecklein, *et al.*, "A novel microfluidic

platform for size and deformability based separation and the subsequent molecular characterization of viable circulating tumor cells," *International journal of cancer*, vol. 138, no. 12, pp. 2894–2904, 2016.

[84] N. M. Karabacak, P. S. Spuhler, F. Fachin, E. J. Lim, V. Pai, E. Ozkumur, J. M. Martel, N. Kojic, K. Smith, P.-i. Chen, *et al.*, "Microfluidic, marker-free isolation of circulating tumor cells from blood samples," *Nature protocols*, vol. 9, no. 3, pp. 694–710, 2014.

[85] S. Bahl, H. Nagar, I. Singh, and S. Sehgal, "Smart materials types, properties and applications: A review," *Materials Today: Proceedings*, vol. 28, pp. 1302–1306, 2020.

[86] Y. Saylan, Ö. Erdem, F. Inci, and A. Denizli, "Advances in biomimetic systems for molecular recognition and biosensing," *Biomimetics*, vol. 5, no. 2, p. 20, 2020.

[87] A. S. Hoffman, "Stimuli-responsive polymers: Biomedical applications and challenges for clinical translation," *Advanced drug delivery reviews*, vol. 65, no. 1, pp. 10–16, 2013.

[88] R. Ning, Q. Zhuang, and J.-M. Lin, "Biomaterial-based microfluidics for cell culture and analysis," in *Cell Analysis on Microfluidics*, pp. 181–224, Springer, 2018.

[89] H. Safarpour, S. Dehghani, R. Nosrati, N. Zebardast, M. Alibolandi, A. Mokhtarzadeh, and M. Ramezani, "Optical and electrochemical-based nano-aptasensing approaches for the detection of circulating tumor cells (ctcs)," *Biosensors and Bioelectronics*, vol. 148, p. 111833, 2020.

[90] L. Wu, L. Zhu, M. Huang, J. Song, H. Zhang, Y. Song, W. Wang, and C. Yang, "Aptamer-based microfluidics for isolation, release and analysis of circulating tumor cells," *TrAC Trends in Analytical Chemistry*, vol. 117, pp. 69–77, 2019.

[91] M. Labib, B. Green, R. M. Mohamadi, A. Mepham, S. U. Ahmed, L. Mahmoudian, I.-H. Chang, E. H. Sargent, and S. O. Kelley, "Aptamer and

antisense-mediated two-dimensional isolation of specific cancer cell subpopulations," *Journal of the American Chemical Society*, vol. 138, no. 8, pp. 2476–2479, 2016.

[92] B. J. Green, L. Kermanshah, M. Labib, S. U. Ahmed, P. N. Silva, L. Mahmoudian, I.-H. Chang, R. M. Mohamadi, J. V. Rocheleau, and S. O. Kelley, "Isolation of phenotypically distinct cancer cells using nanoparticle-mediated sorting," *ACS applied materials & interfaces*, vol. 9, no. 24, pp. 20435–20443, 2017.

[93] C. C. A. Ng, A. Magenau, S. H. Ngalim, S. Ciampi, M. Chockalingham, J. B. Harper, K. Gaus, and J. J. Gooding, "Using an electrical potential to reversibly switch surfaces between two states for dynamically controlling cell adhesion," *Angewandte Chemie International Edition*, vol. 51, no. 31, pp. 7706–7710, 2012.

[94] Q. Shao, P. Wu, P. Gu, X. Xu, H. Zhang, and C. Cai, "Electrochemical and spectroscopic studies on the conformational structure of hemoglobin assembled on gold nanoparticles," *The Journal of Physical Chemistry B*, vol. 115, no. 26, pp. 8627–8637, 2011.

[95] Ö. Erdem, E. Derin, K. Sagdic, E. G. Yilmaz, and F. Inci, "Smart materials-integrated sensor technologies for covid-19 diagnosis," *Emergent Materials*, vol. 4, no. 1, pp. 169–185, 2021.

[96] M. Freitas, H. Nouws, E. Keating, V. C. Fernandes, and C. Delerue-Matos, "Immunomagnetic bead-based bioassay for the voltammetric analysis of the breast cancer biomarker her2-ecd and tumour cells using quantum dots as detection labels," *Microchimica Acta*, vol. 187, no. 3, pp. 1–10, 2020.

[97] W. Y. Hong, S. H. Jeon, E. S. Lee, and Y. Cho, "An integrated multifunctional platform based on biotin-doped conducting polymer nanowires for cell capture, release, and electrochemical sensing," *Biomaterials*, vol. 35, no. 36, pp. 9573–9580, 2014.

[98] Y. Peng, Y. Peng, S. Tang, H. Shen, S. Sheng, Y. Wang, T. Wang, J. Cai, G. Xie, and W. Feng, "Pdirbp mesoporous nanospheres combined with

superconductive carbon black for the electrochemical determination and collection of circulating tumor cells," *Microchimica Acta*, vol. 187, no. 4, pp. 1–11, 2020.

[99] W. Zhang, Z. Dai, X. Liu, and J. Yang, "High-performance electrochemical sensing of circulating tumor dna in peripheral blood based on poly-xanthurenic acid functionalized mos2 nanosheets," *Biosensors and Bioelectronics*, vol. 105, pp. 116–120, 2018.

[100] L. Wu, X. Xu, B. Sharma, W. Wang, X. Qu, L. Zhu, H. Zhang, Y. Song, and C. Yang, "Beyond capture: Circulating tumor cell release and single-cell analysis," *Small Methods*, vol. 3, no. 5, p. 1800544, 2019.

[101] S. Guo, J. Xu, M. Xie, W. Huang, E. Yuan, Y. Liu, L. Fan, S. Cheng, S. Liu, F. Wang, *et al.*, "Degradable zinc-phosphate-based hierarchical nanosubstrates for capture and release of circulating tumor cells," *ACS Applied Materials & Interfaces*, vol. 8, no. 25, pp. 15917–15925, 2016.

[102] M. Xie, N.-N. Lu, S.-B. Cheng, X.-Y. Wang, M. Wang, S. Guo, C.-Y. Wen, J. Hu, D.-W. Pang, and W.-H. Huang, "Engineered decomposable multifunctional nanobioprobes for capture and release of rare cancer cells," *Analytical chemistry*, vol. 86, no. 9, pp. 4618–4626, 2014.

[103] M.-H. Park, E. Reátegui, W. Li, S. N. Tessier, K. H. Wong, A. E. Jensen, V. Thapar, D. Ting, M. Toner, S. L. Stott, *et al.*, "Enhanced isolation and release of circulating tumor cells using nanoparticle binding and ligand exchange in a microfluidic chip," *Journal of the American Chemical Society*, vol. 139, no. 7, pp. 2741–2749, 2017.

[104] S.-W. Lv, Y. Liu, M. Xie, J. Wang, X.-W. Yan, Z. Li, W.-G. Dong, and W.-H. Huang, "Near-infrared light-responsive hydrogel for specific recognition and photothermal site-release of circulating tumor cells," *ACS nano*, vol. 10, no. 6, pp. 6201–6210, 2016.

[105] D. Larson and D. Lawrence, "Acs chem. biol. 2009, 4, 409.(d) mayer, g.; heckel, a," *Angew. Chem., Int. Ed*, vol. 45, p. 4900, 2006.

[106] X. Wei, K. Chen, B. Cai, L. Rao, Z. Wang, Y. Sun, M. Yu, W. Liu, S. Guo, and X.-Z. Zhao, “An acoustic droplet-induced enzyme responsive platform for the capture and on-demand release of single circulating tumor cells,” *ACS applied materials & interfaces*, vol. 11, no. 44, pp. 41118–41126, 2019.

[107] W. Asghar, H. Shafiee, V. Velasco, V. R. Sah, S. Guo, R. El Assal, F. Inci, A. Rajagopalan, M. Jahangir, R. M. Anchan, *et al.*, “Toxicology study of single-walled carbon nanotubes and reduced graphene oxide in human sperm,” *Scientific reports*, vol. 6, no. 1, pp. 1–11, 2016.

[108] Z. Ke, M. Lin, J.-F. Chen, J.-s. Choi, Y. Zhang, A. Fong, A.-J. Liang, S.-F. Chen, Q. Li, W. Fang, *et al.*, “Programming thermoresponsiveness of nanovelcro substrates enables effective purification of circulating tumor cells in lung cancer patients,” *ACS nano*, vol. 9, no. 1, pp. 62–70, 2015.

[109] H. J. Yoon, A. Shanker, Y. Wang, M. Kozminsky, Q. Jin, N. Palanisamy, M. L. Burness, E. Azizi, D. M. Simeone, M. S. Wicha, *et al.*, “Tunable thermal-sensitive polymer–graphene oxide composite for efficient capture and release of viable circulating tumor cells,” *Advanced materials*, vol. 28, no. 24, pp. 4891–4897, 2016.

[110] M. L. Tan, P. F. Choong, and C. R. Dass, “Recent developments in liposomes, microparticles and nanoparticles for protein and peptide drug delivery,” *Peptides*, vol. 31, no. 1, pp. 184–193, 2010.

[111] J. Zhang, W. Ma, X.-P. He, and H. Tian, “Taking orders from light: photo-switchable working/inactive smart surfaces for protein and cell adhesion,” *ACS Applied Materials & Interfaces*, vol. 9, no. 10, pp. 8498–8507, 2017.

[112] V. Brunella, S. A. Jadhav, I. Miletto, G. Berlier, E. Ugazio, S. Sapino, and D. Scalarone, “Hybrid drug carriers with temperature-controlled on–off release: A simple and reliable synthesis of pnipam-functionalized mesoporous silica nanoparticles,” *Reactive and Functional Polymers*, vol. 98, pp. 31–37, 2016.

[113] H.-J. Liu and P. Xu, “Smart mesoporous silica nanoparticles for protein delivery,” *Nanomaterials*, vol. 9, no. 4, p. 511, 2019.

[114] X. Lv, L. Zhang, F. Xing, and H. Lin, "Controlled synthesis of monodispersed mesoporous silica nanoparticles: Particle size tuning and formation mechanism investigation," *Microporous and Mesoporous Materials*, vol. 225, pp. 238–244, 2016.

[115] Y. Bao, C. Shi, T. Wang, X. Li, and J. Ma, "Recent progress in hollow silica: Template synthesis, morphologies and applications," *Microporous and Mesoporous Materials*, vol. 227, pp. 121–136, 2016.

[116] S. Porrang, N. Rahemi, S. Davaran, M. Mahdavi, and B. Hassanzadeh, "Synthesis of temperature/ph dual-responsive mesoporous silica nanoparticles by surface modification and radical polymerization for anti-cancer drug delivery," *Colloids and Surfaces A: Physicochemical and Engineering Aspects*, vol. 623, p. 126719, 2021.

[117] L. Racca, M. Canta, B. Dumontel, A. Ancona, T. Limongi, N. Garino, M. Laurenti, G. Canavese, and V. Cauda, "Smart nanoparticles for biomedicine," 2018.

[118] Y. Gao, S. Gu, Y. Zhang, X. Xie, T. Yu, Y. Lu, Y. Zhu, W. Chen, H. Zhang, H. Dong, *et al.*, "The architecture and function of monoclonal antibody-functionalized mesoporous silica nanoparticles loaded with mifepristone: repurposing abortifacient for cancer metastatic chemoprevention," *Small*, vol. 12, no. 19, pp. 2595–2608, 2016.

[119] J. Wen, K. Yang, F. Liu, H. Li, Y. Xu, and S. Sun, "Diverse gatekeepers for mesoporous silica nanoparticle based drug delivery systems," *Chemical society reviews*, vol. 46, no. 19, pp. 6024–6045, 2017.

[120] C. Boztepe, A. Künkül, and M. Yüceer, "Application of artificial intelligence in modeling of the doxorubicin release behavior of ph and temperature responsive poly (nipaam-co-aac)-peg ipn hydrogel," *Journal of Drug Delivery Science and Technology*, vol. 57, p. 101603, 2020.

[121] C. Boztepe, M. Yüceer, A. Künkül, M. Şölener, and O. S. Kabasakal, "Prediction of the deswelling behaviors of ph-and temperature-responsive poly

(nipaam-co-aac) ipn hydrogel by artificial intelligence techniques," *Research on Chemical Intermediates*, vol. 46, no. 1, pp. 409–428, 2020.

[122] L. Wang, H. Liu, F. Zhang, G. Li, and S. Wang, "Smart thin hydrogel coatings harnessing hydrophobicity and topography to capture and release cancer cells," *Small*, vol. 12, no. 34, pp. 4697–4701, 2016.

[123] Q. Yu, Y. Zhang, H. Chen, Z. Wu, H. Huang, and C. Cheng, "Protein adsorption on poly (n-isopropylacrylamide)-modified silicon surfaces: effects of grafted layer thickness and protein size," *Colloids and Surfaces B: Biointerfaces*, vol. 76, no. 2, pp. 468–474, 2010.

[124] T. A. Saleh, G. Fadillah, and E. Ciptawati, "Smart advanced responsive materials, synthesis methods and classifications: from lab to applications," *Journal of Polymer Research*, vol. 28, no. 6, pp. 1–15, 2021.

[125] E. Yu, A. Lo, L. Jiang, B. Petkus, N. I. Ercan, and P. Stroeve, "Improved controlled release of protein from expanded-pore mesoporous silica nanoparticles modified with co-functionalized poly (n-isopropylacrylamide) and poly (ethylene glycol)(pnipam-peg)," *Colloids and Surfaces B: Biointerfaces*, vol. 149, pp. 297–300, 2017.

[126] A. P. Martinez, B. Qamar, T. R. Fuerst, S. Muro, and A. K. Andrianov, "Biodegradable "smart" polyphosphazenes with intrinsic multifunctionality as intracellular protein delivery vehicles," *Biomacromolecules*, vol. 18, no. 6, pp. 2000–2011, 2017.

[127] V. R. Cherkasov, E. N. Mochalova, A. V. Babenyshev, A. V. Vasilyeva, P. I. Nikitin, and M. P. Nikitin, "Nanoparticle beacons: supersensitive smart materials with on/off-switchable affinity to biomedical targets," *Acs Nano*, vol. 14, no. 2, pp. 1792–1803, 2020.

[128] F. Inci, M. G. Karaaslan, A. Mataji-Kojouri, P. A. Shah, Y. Saylan, Y. Zeng, A. Avadhani, R. Sinclair, D. T.-Y. Lau, and U. Demirci, "Enhancing the nanoplasmonic signal by a nanoparticle sandwiching strategy to detect viruses," *Applied Materials Today*, vol. 20, p. 100709, 2020.

[129] H. Tao, T. Wu, M. Aldeghi, T. C. Wu, A. Aspuru-Guzik, and E. Kumacheva, "Nanoparticle synthesis assisted by machine learning," *Nature Reviews Materials*, vol. 6, no. 8, pp. 701–716, 2021.

[130] X. Guo, Y. Deng, D. Gu, R. Che, and D. Zhao, "Synthesis and microwave absorption of uniform hematite nanoparticles and their core-shell mesoporous silica nanocomposites," *Journal of Materials Chemistry*, vol. 19, no. 37, pp. 6706–6712, 2009.

[131] R. Narayan, U. Y. Nayak, A. M. Raichur, and S. Garg, "Mesoporous silica nanoparticles: A comprehensive review on synthesis and recent advances," *Pharmaceutics*, vol. 10, no. 3, p. 118, 2018.

[132] T. Sugimoto, M. Khan, A. Muramatsu, and H. Itoh, "Colloids surfaces," *A: Physicochem. Eng. Aspects*, vol. 79, p. 233, 1993.

[133] T. Sugimoto, M. M. Khan, A. Muramatsu, and H. Itoh, "Formation mechanism of monodisperse peanut-type α-fe2o3 particles from condensed ferric hydroxide gel," *Colloids and Surfaces A: Physicochemical and Engineering Aspects*, vol. 79, no. 2-3, pp. 233–247, 1993.

[134] W. Stöber, A. Fink, and E. Bohn, "Controlled growth of monodisperse silica spheres in the micron size range," *Journal of colloid and interface science*, vol. 26, no. 1, pp. 62–69, 1968.

[135] Y. Wang, X. Su, P. Ding, S. Lu, and H. Yu, "Shape-controlled synthesis of hollow silica colloids," *Langmuir*, vol. 29, no. 37, pp. 11575–11581, 2013.

[136] K. Manivannan, Y.-S. Huang, B.-R. Huang, C.-F. Huang, and J.-K. Chen, "Real-time packing behavior of core-shell silica@ poly (n-isopropylacrylamide) microspheres as photonic crystals for visualizing in thermal sensing," *Polymers*, vol. 8, no. 12, p. 428, 2016.

[137] P. Pan, M. Fujita, W.-Y. Ooi, K. Sudesh, T. Takarada, A. Goto, and M. Maeda, "Dna-functionalized thermoresponsive bioconjugates synthesized via atrp and click chemistry," *Polymer*, vol. 52, no. 4, pp. 895–900, 2011.

[138] M. Zainuri, "Hematite from natural iron stones as microwave absorbing material on x-band frequency ranges," in *IOP conference series: materials science and engineering*, vol. 196, p. 012008, IOP Publishing, 2017.

[139] R. K. Biswas, P. Khan, S. Mukherjee, A. K. Mukhopadhyay, J. Ghosh, and K. Muraleedharan, "Study of short range structure of amorphous silica from pdf using ag radiation in laboratory xrd system, raman and nexafs," *Journal of Non-Crystalline Solids*, vol. 488, pp. 1–9, 2018.

[140] R. G. Sousa, W. F. Magalhães, and R. F. Freitas, "Glass transition and thermal stability of poly (n-isopropylacrylamide) gels and some of their copolymers with acrylamide," *Polymer degradation and stability*, vol. 61, no. 2, pp. 275–281, 1998.

[141] X. Lu, L. Zhang, L. Meng, and Y. Liu, "Synthesis of poly (n-isopropylacrylamide) by atrp using a fluorescein-based initiator," *Polymer Bulletin*, vol. 59, no. 2, pp. 195–206, 2007.

[142] S. Li and X. Liu, "Synthesis, characterization, and evaluation of enzymatically degradable poly (n-isopropylacrylamide-co-acrylic acid) hydrogels for colon-specific drug delivery," *Polymers for Advanced Technologies*, vol. 19, no. 11, pp. 1536–1542, 2008.

[143] L. A. Fulton, P. Zhang, W. R. Seitz, J. G. Tsavalas, and R. P. Planalp, "Dynamic aggregation of poly-n-isopropylacrylamide characterized using second-order scattering," *Applied Spectroscopy*, vol. 72, no. 9, pp. 1341–1348, 2018.

[144] Y.-J. Shih, Y. Chang, A. Deratani, and D. Quemener, ""schizophrenic" hemocompatible copolymers via switchable thermoresponsive transition of nonionic/zwitterionic block self-assembly in human blood," *Biomacromolecules*, vol. 13, no. 9, pp. 2849–2858, 2012.

[145] S. Gupta, A. Singh, and N. Matsumi, "Controlled phase behavior of thermally sensitive poly (n-isopropylacrylamide/ionic liquid) with embedded au nanoparticles," *ACS omega*, vol. 4, no. 25, pp. 20923–20930, 2019.

[146] A. Liga, A. Vliegenthart, W. Oosthuyzen, J. Dear, and M. Kersaudy-Kerhoas, “Exosome isolation: a microfluidic road-map,” *Lab on a Chip*, vol. 15, no. 11, pp. 2388–2394, 2015.

[147] T. Noeiaghaei, J.-O. Kim, and S.-R. Chae, “Recent advances in nano-hybrid membranes for advanced water treatment,” *Current Organic Chemistry*, vol. 18, no. 18, pp. 2381–2404, 2014.

[148] J. Shao, L. Wu, J. Wu, Y. Zheng, H. Zhao, Q. Jin, and J. Zhao, “Integrated microfluidic chip for endothelial cells culture and analysis exposed to a pulsatile and oscillatory shear stress,” *Lab on a Chip*, vol. 9, no. 21, pp. 3118–3125, 2009.

[149] T. H. Kim, J. M. Lee, C. D. Ahrberg, and B. G. Chung, “Development of the microfluidic device to regulate shear stress gradients,” *BioChip Journal*, vol. 12, no. 4, pp. 294–303, 2018.

[150] N. J. Kent, S. O’Brien, L. Basabe-Desmonts, G. R. Meade, B. D. MacCraith, B. G. Corcoran, D. Kenny, and A. J. Ricco, “Shear-mediated platelet adhesion analysis in less than 100 μ l of blood: Toward a poc platelet diagnostic,” *IEEE transactions on biomedical engineering*, vol. 58, no. 3, pp. 826–830, 2010.

[151] R. Khnouf, D. Karasneh, and B. A. Albiss, “Protein immobilization on the surface of polydimethylsiloxane and polymethyl methacrylate microfluidic devices,” *Electrophoresis*, vol. 37, no. 3, pp. 529–535, 2016.

[152] K. H. Neoh, S. K. S. Cheng, H. Wu, A. Chen, Y. Sun, B. Li, A. Cao, and R. P. Han, “ph-responsive carbon nanotube film-based microfluidic chip for efficient capture and release of cancer cells,” *ACS Applied Nano Materials*, 2022.

[153] S. Wang, M. Esfahani, U. A. Gurkan, F. Inci, D. R. Kuritzkes, and U. Demirci, “Efficient on-chip isolation of hiv subtypes,” *Lab on a Chip*, vol. 12, no. 8, pp. 1508–1515, 2012.

[154] S. Wang, D. Sarenac, M. H. Chen, S.-H. Huang, F. F. Giguel, D. R. Kuritzkes, and U. Demirci, “Simple filter microchip for rapid separation of plasma and viruses from whole blood,” *International journal of nanomedicine*, vol. 7, p. 5019, 2012.

[155] F. Inci, “Benchmarking a microfluidic-based filtration for isolating biological particles,” *Langmuir*, vol. 38, no. 5, pp. 1897–1909, 2022.

[156] J. M. Tarbell and Z.-D. Shi, “Effect of the glycocalyx layer on transmission of interstitial flow shear stress to embedded cells,” *Biomechanics and modeling in mechanobiology*, vol. 12, no. 1, pp. 111–121, 2013.

[157] V. Balan, I. A. Petrache, M. I. Popa, M. Butnaru, E. Barbu, J. Tsibouklis, and L. Verestiuc, “Biotinylated chitosan-based spions with potential in blood-contacting applications,” *Journal of Nanoparticle Research*, vol. 14, no. 2, pp. 1–14, 2012.

[158] R. Sanjeev and V. Jagannadham, “Comparison of substituent effects in benzenes (xc5h5c), pyridines (xc5h4n) and phosphorines (xc5h4p) and their protonated species,” *World*, vol. 8, no. 4, pp. 155–162, 2020.

[159] T. Jordan, M. A. O’Brien, C.-P. Spatarelu, and G. P. Luke, “Antibody-conjugated barium titanate nanoparticles for cell-specific targeting,” *ACS Applied Nano Materials*, vol. 3, no. 3, pp. 2636–2646, 2020.

[160] A. P. Dubey, “Carbon nanofiber and polymer conjugate,” *Carbon Nanofibers: Fundamentals and Applications*, pp. 75–98, 2021.

[161] S. Maslanka Figueroa, D. Fleischmann, S. Beck, and A. Goepferich, “Thermodynamic, spatial and methodological considerations for the manufacturing of therapeutic polymer nanoparticles,” *Pharmaceutical research*, vol. 37, no. 3, pp. 1–11, 2020.

[162] H. Shafiee, E. A. Lidstone, M. Jahangir, F. Inci, E. Hanhauser, T. J. Henrich, D. R. Kuritzkes, B. T. Cunningham, and U. Demirci, “Nanostructured optical photonic crystal biosensor for hiv viral load measurement,” *Scientific reports*, vol. 4, no. 1, pp. 1–7, 2014.

[163] D. P. Nair, M. Podgorski, S. Chatani, T. Gong, W. Xi, C. R. Fenoli, and C. N. Bowman, "The thiol-michael addition click reaction: a powerful and widely used tool in materials chemistry," *Chemistry of Materials*, vol. 26, no. 1, pp. 724–744, 2014.

[164] Y. Liu, F. Seidi, and J. Song, "Atrp-tethering anti-fouling/anti-fogging hydrophilic thin hydrogel layers on the surface of glass slides," *Polymer Science, Series A*, vol. 63, no. 6, pp. 705–711, 2021.

[165] S. S. Shah, *Electrochemically switchable surfaces for cell cultivation and release*. University of California, Davis, 2011.

[166] P. Ihalainen, H. Majumdar, T. Viitala, B. Törngren, T. Närjeoja, A. Määttänen, J. Sarfraz, H. Härmä, M. Yliperttula, R. Österbacka, *et al.*, "Application of paper-supported printed gold electrodes for impedimetric immunosensor development," *Biosensors*, vol. 3, no. 1, pp. 1–17, 2012.

[167] B.-S. Yoo and F. E. Regnier, "Proteomic analysis of carbonylated proteins in two-dimensional gel electrophoresis using avidin-fluorescein affinity staining," *Electrophoresis*, vol. 25, no. 9, pp. 1334–1341, 2004.

[168] Y. Liu and C. M. Li, "Advanced immobilization and amplification for high performance protein chips," *Analytical letters*, vol. 45, no. 2-3, pp. 130–155, 2012.

[169] N. Li, J. Xiao, X. Hai, K. Wang, and F. Dang, "Key role of ionic hydrogen bonding in nonspecific protein adsorption on a hydrophobic surface," *The Journal of Physical Chemistry C*, vol. 120, no. 34, pp. 19135–19141, 2016.

[170] T. Trantidou, T. Prodromakis, and C. Toumazou, "Oxygen plasma induced hydrophilicity of parylene-c thin films," *Applied surface science*, vol. 261, pp. 43–51, 2012.

[171] R. Cheng, F. Meng, S. Ma, H. Xu, H. Liu, X. Jing, and Z. Zhong, "Reduction and temperature dual-responsive crosslinked polymersomes for targeted intracellular protein delivery," *Journal of materials chemistry*, vol. 21, no. 47, pp. 19013–19020, 2011.

[172] R. Bastien, T. B. Lewis, J. E. Hawkes, J. F. Quackenbush, T. C. Robbins, J. Palazzo, C. M. Perou, and P. S. Bernard, “High-throughput amplicon scanning of the tp53 gene in breast cancer using high-resolution fluorescent melting curve analyses and automatic mutation calling,” *Human Mutation*, vol. 29, no. 5, pp. 757–764, 2008.

[173] S. Li, C. Cao, J. Gao, K. Li, J. Kang, D. Wu, and Y. Kong, “Dual stimuli-responsive nanoplatform based on core-shell structured graphene oxide/mesoporous silica@ alginate,” *International Journal of Biological Macromolecules*, vol. 175, pp. 209–216, 2021.

[174] A. V. Lee, S. Oesterreich, and N. E. Davidson, “Mcf-7 cells—changing the course of breast cancer research and care for 45 years,” *JNCI: Journal of the National Cancer Institute*, vol. 107, no. 7, 2015.

[175] S. Gao, Y. Sun, X. Liu, D. Zhang, and X. Yang, “Epcam and cox-2 expression are positively correlated in human breast cancer,” *Molecular Medicine Reports*, vol. 15, no. 6, pp. 3755–3760, 2017.

[176] Z.-m. Chang, Z. Wang, D. Shao, J. Yue, H. Xing, L. Li, M. Ge, M. Li, H. Yan, H. Hu, *et al.*, “Shape engineering boosts magnetic mesoporous silica nanoparticle-based isolation and detection of circulating tumor cells,” *ACS applied materials & interfaces*, vol. 10, no. 13, pp. 10656–10663, 2018.

[177] E. M. Ngigi, B. P. George, H. Abrahamse, P. N. Nomngongo, and J. C. Ngila, “Cytotoxic effects of novel solvothermal synthesised ag-doped pegylated wo3 sheet-like nanocomposites on mcf-7 human breast cancer cells,” *Journal of Nanoparticle Research*, vol. 22, no. 7, pp. 1–13, 2020.

[178] H. Liu, X. Liu, J. Meng, P. Zhang, G. Yang, B. Su, K. Sun, L. Chen, D. Han, S. Wang, *et al.*, “Hydrophobic interaction-mediated capture and release of cancer cells on thermoresponsive nanostructured surfaces,” *Advanced Materials*, vol. 25, no. 6, pp. 922–927, 2013.

[179] J. Hong, C. Park, and Y. Kim, “Photothermal properties of wool fabrics colored with sio2@ aunps,” *Colloids and Surfaces A: Physicochemical and Engineering Aspects*, vol. 574, pp. 115–121, 2019.

[180] D. Ş. Karaman, A. Pamukçu, M. B. Karakaplan, O. Kocaoglu, and J. M. Rosenholm, "Recent advances in the use of mesoporous silica nanoparticles for the diagnosis of bacterial infections," *International Journal of Nanomedicine*, vol. 16, p. 6575, 2021.

[181] Q. Zheng, S. M. Iqbal, and Y. Wan, "Cell detachment: Post-isolation challenges," *Biotechnology advances*, vol. 31, no. 8, pp. 1664–1675, 2013.

[182] X. Wu, Z. Wang, D. Zhu, S. Zong, L. Yang, Y. Zhong, and Y. Cui, "ph and thermo dual-stimuli-responsive drug carrier based on mesoporous silica nanoparticles encapsulated in a copolymer–lipid bilayer," *ACS applied materials & interfaces*, vol. 5, no. 21, pp. 10895–10903, 2013.

[183] R. P. McNamara, Y. Zhou, A. B. Eason, J. T. Landis, M. G. Chambers, S. Willcox, T. A. Peterson, B. Schouest, N. J. Maness, A. G. MacLean, *et al.*, "Imaging of surface microdomains on individual extracellular vesicles in 3-d," *Journal of extracellular vesicles*, vol. 11, no. 3, p. e12191, 2022.

[184] K. Sagdic, I. Eş, M. Sitti, and F. Inci, "Smart materials: rational design in biosystems via artificial intelligence," *Trends in Biotechnology*, 2022.

[185] Ö. Erdem, E. Derin, S. Zeibi Shirejini, K. Sagdic, E. G. Yilmaz, S. Yildiz, G. A. Akceoglu, and F. Inci, "Carbon-based nanomaterials and sensing tools for wearable health monitoring devices," *Advanced Materials Technologies*, vol. 7, no. 3, p. 2100572, 2022.

[186] K. Sagdic, Ö. Erdem, E. Derin, S. Z. Shirejini, Y. Aslan, S. Celik, U. Celik, and F. Inci, "Micromechanical biosensors for virus detection," *Biosensors for Virus Detection*, pp. 8–1, 2021.

Appendix A

APPENDIX

A.1 Declaration of Copyright Cleareance Aggrements

Reference Number	License Supplier	License Number
[1]	John Wiley and Sons	5332510580640
[2]	Springer Nature	Permission not required
[3]	Frontiers in Oncology	Permission not required
[4]	American Chemical Society	Permission not required
[5]	American Chemical Society	Permission not required
[6]	John Wiley and Sons	5365411415763
[7]	American Chemical Society	Permission not required
[8]	American Chemical Society	Permission not required
[9]	American Chemical Society	Permission not required
[10]	Royal Society of Chemistry	Permission not required
[11]	John Wiley and Sons	5365421095629